Universidad Nacional Autónoma de México
Programa de maestría y doctorado en ingeniería
Ingeniería mecánica - Termofluidos

Numerical simulation of non-steady flows around solid bodies with arbitrary motion using a weakly-compressible Smoothed Particle Hydrodynamics method.

Tesis
Que para optar por el grado de:
Maestro en Ingeniería

Presenta:
ALEJANDRO GARCÍA PÉREZ

Tutor principal
Rubén, Ávila, Rodríguez, CIA, Departamento de Termofluidos

Ciudad Universitaria, CD. MX. Enero 2018

Jurado asignado:

Presidente: DR. CERVANTES DE GORTARI JAIME G.
Secretario: DR. SOLORIO ORDAZ FRANCISCO JAVIER
Vocal: DR. ÁVILA RODRÍGUEZ RUBÉN
1er. Suplente: DR. VICENTE Y RODRÍGUEZ WILLIAM
2do. Suplente: DR. RAMOS MORA EDUARDO

Lugar donde se realizó la tesis: Facultad de Ingeniería, UNAM

Tutor de tesis:

RUBÉN ÁVILA RODRÍGUEZ

Firma

Acknowledgements

...to God, the most kind, elegant and unpredictable force of equilibrium.

This work is dedicated to the most wonderful persons I have ever met, my mother María del Carmen, my father Victor, and my two brothers Victor Hugo and Enrique.

Special thanks to Jessy and her unconditional and incredible love, help and support during my studies and my daily life lessons.

Thank you García and Narvaez families.

Grazie mille alla meravigliosa famiglia Landi per avermi considerato un membro della loro famiglia durante la mia permanenza nella bellissima città di Parma, Italia.

I would like to thank also my friends and professors from IPN, UNAM, IIM, CELE and the University of Parma for all those great moments, and constructive discussions.

To my supervisors of the academy staff here in México and Italy who always have encouraged me to contribute to the scientific community. Their knowledge and experience is the present for a success future.

Abstract

This study presents the implementation of the novel Smoothed Particle Hydrodynamics (SPH) meshless method regarding fluid solid interaction. To assess the numerical approach five study cases have been carried out, namely the classical benchmark problems; fluid flow around a fixed circular cylinder, and flow around a square cylinder when it travels through a fluid at rest. The next case concern the numerical simulation of the buoyancy effect on a circular cylinder whose density value is lower than the media in which it is immersed. The two last cases exposes the numerical analysis of a train when it travels along a tunnel at a high velocity and the last case treats the numerical simulation of the ascending motion of a submarine hull located at a certain depth from the free surface. A comparison between numerical results and experimental previous solutions is exposed, showing that the SPH methodology provides promising advantages in contrast with the conventional mesh-grid based methods. Concluding results in the train study case highlights a similar tendency for pressures measurements in comparison with early works related to the same phenomenon. Nevertheless it is concluded that special attention to the equation of state is required due to the increase in the density field variations during the train passing. Finally in the study case of the submarine hull, the rolling stability issue is effectively reproduced with no additional treatment like in previous works usually do while using conventional mesh-grid approaches. It is concluded that a substantial reduction in the height of the sail should be carried out in order to reduce the effect that promotes instability flaws design during the submarine ascending performance.

Resumen

En este estudio se presenta la implementación del novedoso método no dependiente de mallado Smoothed Particle Hydrodynamics concerniente al problema de la interacción fluido sólido. Para evaluar la metodología numérica, cinco casos de estudio se han llevado a cabo, a saber, los ya clasicos problemas tipo benchmark; flujo alrededor de un cilindro circular fijo y el flujo alrededor de un cilindro cuadrado moviendose en un fluido en reposo. El siguiente caso consiste en la simulación numérica del efecto boyante sobre un cilindro circular cuyo valor de densidad es menor al del fluido en el cual se encuentra inmerso. Los últimos dos casos exponen el estudio numérico de un tren viajando a gran velocidad a lo largo de un tunel y el caso final aborda la simulación numérica del movimiento ascendente de un submarino posicionado a cierta profundidad de la superficie libre. Así mismo, se expone una comparación entre resultados obtenidos numéricamente y resultados experimentales previos, dando a resaltar que la metodología del SPH provee ventajas prometedoras en contraste con los métodos convencionales dependientes de un mallado. Resultados concluyentes en el caso de estudio del tren, resaltan una tendencia similar en las medidas de presión en comparación con trabajos previos relacionados con el mismo fenómeno. Sin embargo, se requiere especial atención a la ecuación de estado utilizada para el cálculo de presión debido al incremento de variaciones en el campo de densidad, durante el paso del tren. Finalmente en el estudio del submarino, el problema de la estabilidad en el Rolling es reproducido de forma efectiva, sin tener que implementar un tratamiento adicional como sucede en los métodos convencionales basados de mallado. Se concluye finalmente, que se debe realizar una reducción sustancial de la altura del sail, para reducir los efectos que promueven problemas de inestabilidad durante el movimiento ascendente del submarino.

Contents

List of Figures

List of Tables

1

Introduction

Arbitrary motion of solid bodies in a particular fluid flow appears in a diverse range of applications, either in industrial or research fields. The great importance of acquiring a consistent understanding, and a continuous enhancement of such issue demands not only an increasing endeavour to understand and clarify the solid body dynamics, but also the prediction of the body behaviour that results from the interaction with the fluid in which the body performs a specific purpose.

Calculation of the resultant forces onto a body generated by the fluid flow hydrodynamics is widely considered to be a vital factor of importance in the design stage of engineering systems, since it allows researches and engineers to model a suitable body shape to maintain a stable state condition, prevent potential failures or even avoid fatal accidents. Forces that appear during any solid-fluid interaction are obtained via experiment, implementing a numerical simulation, and in some simplified cases an analytical solution can be obtained; field variables like velocity, pressure, position, and density constitute the most essential aspects that must be considered to calculate these forces. This study is mainly focused on the numerical simulation of the solid-fluid interaction and the resultant effect on the solid body dynamics. Implementing an experimental campaign, and a successful technique that captures the aforementioned field variables represent a more real support, since each measurement is taken from the real flow interaction. Nevertheless while carrying out an experiment demands most of the time highly building costs, waste of time concerning issues of collocation, not to mention that the apparatus are usually restricted to just one kind of measurement. Some examples of modern experimental techniques used in the analysis of fluid flows are the particle-laden techniques. An excel-

lent review of most modern particle-laden techniques is discussed in (Tu et al., 2017). These visualizing techniques are used essentially for single-phase flows, and present the limitation of providing only average measurements of some field variables, and analysis in 2D.

Examples of experimental studies concerning solid-fluid interaction are: (Havelock, 1936), who used an image method for the calculation of forces on a circular cylinder. (Greenhow et al., 1982), that examined the problem of the survival of Salter's duck wave-energy device in extreme waves, both experimentally and theoretically. (Moyo and Greenhow, 2000) solved solid-fluid interaction implementing the Vinje and Brevig method, for the submerging and sinking of a cylinder. More recently (Ricco et al., 2007) who performed an experimental analysis of the pressure generated of a train running through a tunnel at a high speed.

Employing a numerical simulation, on the other hand, provides a more practical option. This is because some engineering and physical phenomena could be adequately simulated. For instance it is just a matter of few lines of computational code to acquire relevant information of field variables in space, and time in the domain of the numerical simulation. The numerical techniques offer the advantage of simulating at a real scale, the phenomenon under study. Furthermore, the simulations allow to control directly situations which are difficult to reach or maintain in real life.

Depending on the methodology adopted, the computational time in a numerical approach can increase from some hours to many days. Until now most of the numerical techniques are mesh dependent, which means that the principal condition for a phenomenon to be accurately simulated is the construction of a suitable mesh capable of representing the true physics or at least an approximation. This mesh dependency causes many issues related to the selection, construction, and time evolution of the mesh during a numerical simulation. In this study a different numerical scheme is adopted in order to overcome common shortcomings that appear in traditional mesh dependent numerical methods.

In recent years meshless numerical techniques have become an alternative tool that present many advantages in contrast with mesh methods. The novel Lagrangian approach Smoothed Particle Hydrodynamics (henceforth referred SPH) has emerged as a new numerical tool for solving difficult problems that otherwise require an additional effort, and the application and coupling of distinct techniques. Based on the meshless concept the SPH method is ideal, (as it will be explained in the next chapters) for this sort of solid-fluid interaction problems.

Recently the High Performance Computing (HPC), allows the massively parallel architecture of GPUs and Clusters significantly accelerate simulations regarding transient solid-fluid interaction phenomena. By combining attributes from both numerical methodologies and HPC it is possible to provide a powerful numerical tool that open new branches of treating complex problems that allow scientist understand a physical phenomenon. Figure 1.1 shows the global process of a numerical simulation based upon the author experience.
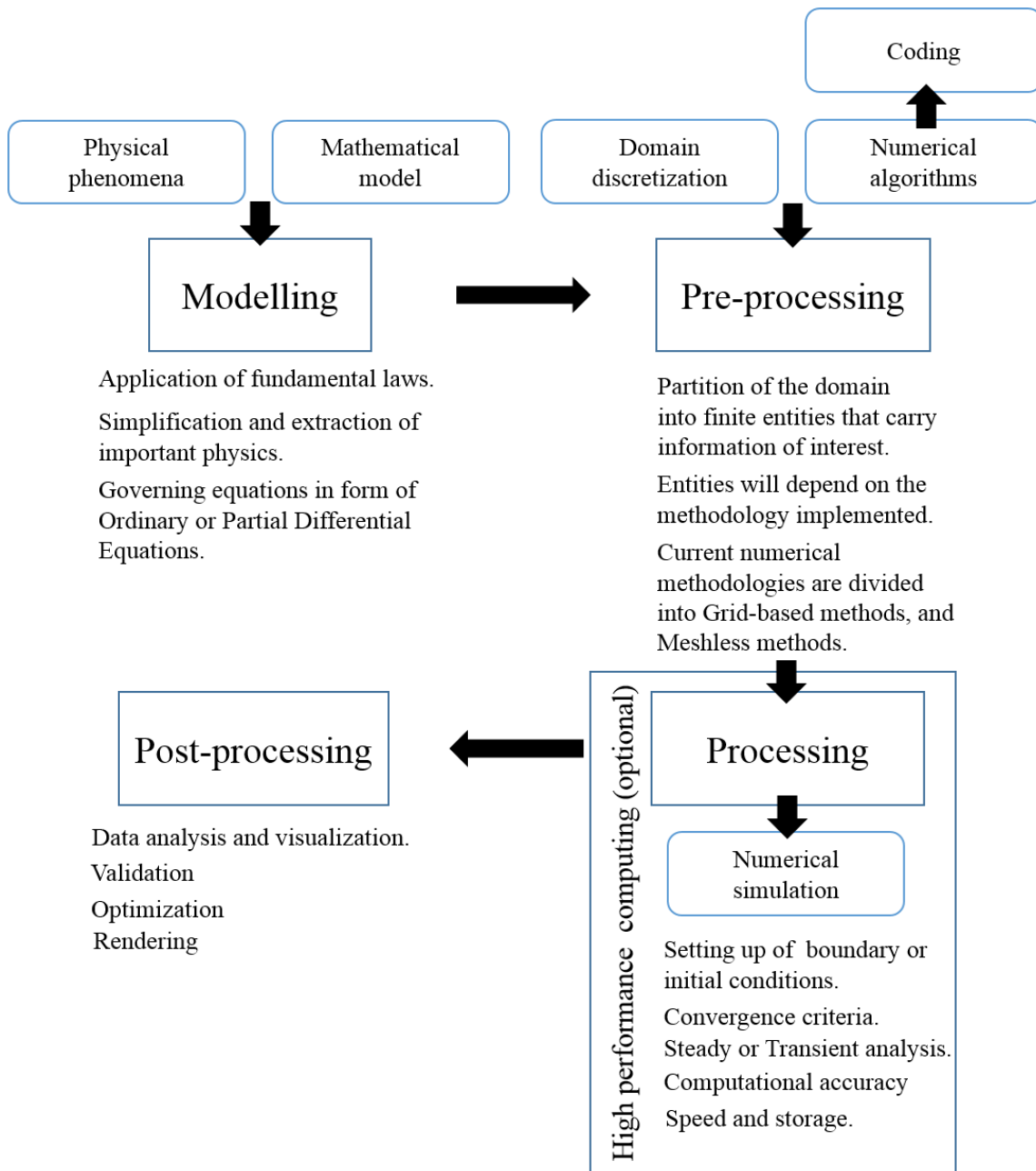
Figure 1.1: General procedure of conducting a numerical simulation.

The resultant effect of the forces exerted on the body as a consequence of the solid-fluid interaction, carries a change of momentum in the body, causing an instability on its degrees of freedom. Engineers and researchers are mainly interested in the study of the influence that the fluid flow exerts to the degrees of freedom of the body. There exist several applications in which the essential ground of interest is the solid-fluid interaction, but only some of them are listed below:

1. Overtopping

2. Slamming bodies

3. Offshore

4. Buoyancy driven bodies

5. Tsunamis

6. Turbines

7. Windmills

8. Moving rigid bodies

In this study five cases are simulated numerically. Three of them will assess the reliability and accuracy of the numerical method implemented. The other two cases concern a major attention due to their difficulty to be analysed. The first study case concerns the numerical simulation of the ascending motion of a submarine hull (a buoyancy driven body) immersed in a viscous fluid, the second case is related to the numerical simulation of a high velocity train (a moving rigid body), when it passes trough a tunnel. The software DualSPHysics based on the novel numerical method Smoothed Particle Hydrodynamics is used to calculate Pitching, Yawing, and Rolling on the submarine hull produced by the interaction with the fluid. For the second case, pressure and velocity fields are calculated during the train travelling inside a tunnel.

1.1   Background

The numerical simulations concerning the interaction between a solid body and a fluid flow are been carried out mainly using two different approaches, namely mesh-grid methods, and meshfree methods. Mesh-grid methods have the availability of adopting either an Eulerian or a Lagrangian scheme. On the other hand meshfree methods provide a numerical tool without the aid of a mesh. Based upon the Lagrangian scheme meshfree methods are expected to overcome shortcomings appearing in traditional mesh-grid numerical approaches. During the last decades there have been efforts to implement an hybrid of both methods(Lagrangian-Eulerian methods), enhancing the performance of conventional mesh-grid techniques see (Liu and Liu, 2003).

1.2   Mesh-grid based methods

The principal idea of mesh-grid methods relies on the spacial domain division into abstract entities (that carry field variables information), distributed along a mesh. Following (Liu and Liu, 2003), a *mesh* is defined as any of the open spaces between the strands of a net that is formed by connecting nodes in a predefined manner. Entities in essence, are represented as cells, nodes or elements depending of the numerical methodology. The main process of calculation during a numerical simulation is performed on each of these abstract computational entities by means of considering contributions of neighbours preserving a certain topological relation. A global idea of the concepts above described is exposed in Figure 1.2.
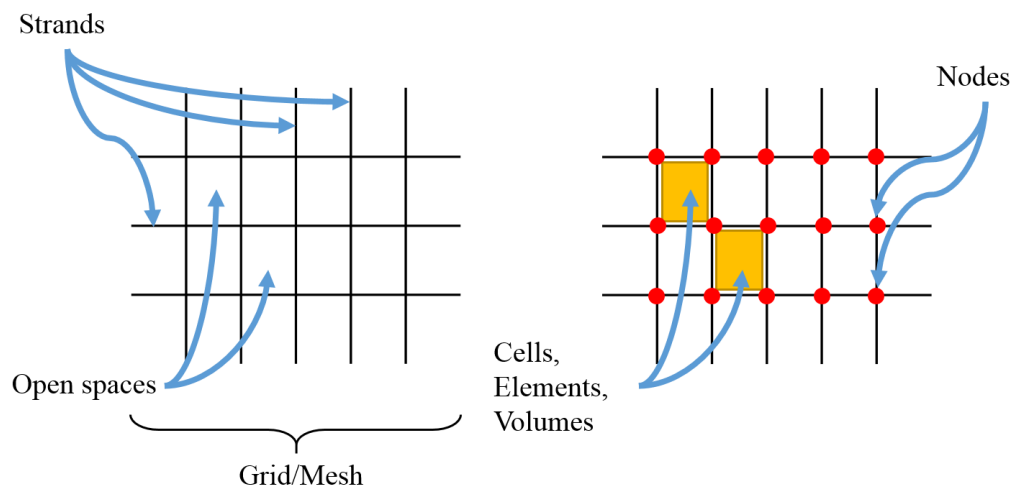
Figure 1.2: Concept of a Mesh-Grid and abstract entities.

Conventional and more common methodologies based upon mesh-grid methods are: Finite Element Method (FEM), (Liu and Quek, 2013; Zienkiewicz and Taylor, 2000), Finite Differences Method (FDM), (Kleiber, 1998), and Finite Volume Method (FVM), (LeVeque, 2002). The meshing process will be in fact the fundamental aspect of these kind of conventional numerical methods.

Regarding mesh-grid based methods, remarkable works that treat the the solid-fluid flow interaction are for example: (Greenhow et al., 1981), considered as the first consistent simulation method for two dimensional problem concerning floating bodies. (S Peskin, 1977) who originally proposed the Immersed Boundary Method (IBM). (Fekken, 2004) that implemented a coupled FVM, and a different version of the (IBM). (Liu, 2004) published the study of numerical simulation of two trains passing each other using an overset grid scheme for the domain of the simulation and the overlap grid method for the calculation of properties at some specific zones. (Hadžić et al., 2005) in which the RANS and body dynamics equations are solved simultaneously by means of the SIMPLE-algorithm. In that work the FVM is used, and moving-grids for the solver are employed. Similar to this study (Zhang et al., 2013), carried out the numerical simulation of the steady turning of a submarine using a commercial software that implements a FVM. More recently (Chu et al., 2014), who presented a a numerical study of two high trains when they cross by inside a tunnel using a turbulence model based in the k-ϵ technique. (Bettle et al., 2014a) used a commercial software CFX connected with Fortran subroutines for evaluating an auxiliary coefficient-based model to solve simultaneously the integration of the 6 DOF rigid body equations and the URANS equations in time during the numerical simulation of a submarine hull ascending motion.

1.3 Meshfree methods

In meshfree methods the domain of interest is subdivided into scattered or arbitrarily distributed nodes called particles, nevertheless no predefined mesh/grid is required. Each of the particles stores field variables locally as a result of the contribution of neighbours(Liu and Liu, 2003) like in mesh-grid methods, but no complex relation between particles exist. In this study a meshfree method is adopted to perform the calculations of the solid-fluid interaction. Therefore on the next paragraphs the focus will be maintained on these kind of numerical approaches.

Some excellent reviews about meshfree methods can be found in (Belytschko et al., 1996; Li and Liu, 2002). In the monograph on meshfree methods (Li and Liu, 2002) the author has addressed the history, development, theory and applications of the major existing meshfree methods.

Implementing a meshfree numerical scheme for solid-fluid interactions, it is worth mentioning the previous work of (Koshizuka et al., 1998) where a particle semi-implicit (MPS) method was used for solid-fluid interactions. In (B. Kajtar and J. Monaghan, 2009) the authors presented a numerical simulation of a 2-D fish-like movement in a fluid, aided with Lagrange multipliers in the restrictions of the equations of motion, resulting in good agreement with other related works. Other authors like (Monaghan et al., 2003) present a comparison between Moving Particle semi-implicit Method and Smoothed Particle Hydrodynamics while simulating numerically the fluid motion generated by impact. (Rogers et al., 2010) present the solid-fluid interaction based in the idea of repulsive boundary force technique , additionally providing an effectively sort of frictional force when two bodies collision. In (Ulrich and Rung, 2012) a numerical simulation of a water entry of a cube is presented, resulting in good agreement with experimental data. Later in (Omidvar et al., 2013) an hybrid model using SPH and the ALE method is developed for the study of floating bodies. The ground objective of this work was to include a variable particle mass distribution in order to increase resolution where is needed, and to improve computational costs. The comparison between SPH and the experiment shows excellent agreement for the force and free surface for motion.(Bouscasse et al., 2013) carried out numerical simulations using a combination of SPH and ghost particle technique to reproduce the movement of floating bodies interaction with non-linear water waves in free surface flows. (Liu et al., 2014) treated the fluid-solid interface with a coupled dynamic algorithm (CD-FSIT) and the SPH method, in this work solid particles move with the rigid objects. (Canelas et al., 2015) performed numerical simulations of buoyancy-driven motion with solid bodies using the SPH method. The results were compared with experimental data obtaining good agreement.

Meshfree methods seem to be generating a considerable interest in the field of Computational Fluid Dynamics. As seen before, these methods do not require special treatments or at least no too many as mesh-grid based methods usually do. The studies presented above using these mesh independent numerical schemes expose some of the advantages over the conventional mesh-grid based methods for applications of solid-fluid interactions, driven motion of solid bodies in free surfaces flows etc. Furthermore, the necessity of employing a numerical scheme that is adequate for High Performance Parallel architectures in the last years encourage the use of these numerical approaches.

There are largely two categories of numerical methods for solving the governing equations (PDEs) that rule a physical phenomenon: *direct approach and indirect approach*[1]. Table 1.1 and 1.2 present a general framework regarding mesh-grid and meshfree methods considering the aforementioned categories.

Mesh-Grid methods	
Strong formulation	PDE's that rule the problem physics are discretized and solved directly.
Weak formulation	PDE's are not solved directly, but an alternative equation with the highest order of the initial derivative reduced in one order. Solution of an integral equation (averaged).

Table 1.1: Categories concerning Mesh-Grid methods

Meshfree methods	
Strong formulation	PDE's that rule the problem physics are discretized and solved directly.
Weak formulation	It does not represent a truly meshless approach due to the requirement of a mesh, as it is mandatory for the integration of the weak forms.
Particle formulation	Solution of an integral equation (averaged). Additionally the differential operator passes directly on the weighted average operator.

Table 1.2: Categories concerning Meshfree methods

Special attention is given to the meshfree particle[2] methods, since the SPH approach adopted in this thesis pertains to this sort of methodologies.

Meshfree particle methods

Particle-based methods (or particle methods for abbreviation) in general refers to a special class of meshfree methods that employ a set of finite number of discrete particles to represent the computational domain of a system under study. The initial state of the discretized domain and its evolution in time is developed through the movement of the particles. A thoroughly discussion in

---

[1] A more in-depth explanation can be found in (Liu and Han, 2003)

[2] In (Li and Liu, 2007) a complete mathematical description of such techniques can be found.

relation to the advantages of meshfree particle methods over conventional grid-based numerical methods is highlighted in (Liu and Liu, 2003). Nonetheless the principal differences between the mesh-grid and meshfree particle methods are mentioned next:

▶ The problem domain is discretized by means of a set of arbitrary distributed particles (*Particle representation*).

▶ Functions, derivatives and integrals in the governing equations are approximated using the particles rather than over a mesh (*Particle approximation*).

Particle representation

In meshfree particle methods, there is no need of considering the connectivity between such entities titled particles. Only an initial arbitrary distribution (known as domain representation/discretization) of particles that represents the discretized domain is required. Different ways of generating and populate particles complex domains can be employed.

Figure 1.3 is an example of a particle representation of a complex CAD model. Figures 1.3(a) and 1.3(c) show the isometric and frontal views of the initial geometry. Figures 1.3(b), and 1.3(d) exhibit their final particle representation respectively; the transformation from the solid to the particle representation was carried out using the GenCase subrutine inside the DualSPHyics software (Crespo et al., 2015).

(a)

(b)

(c)

(d)
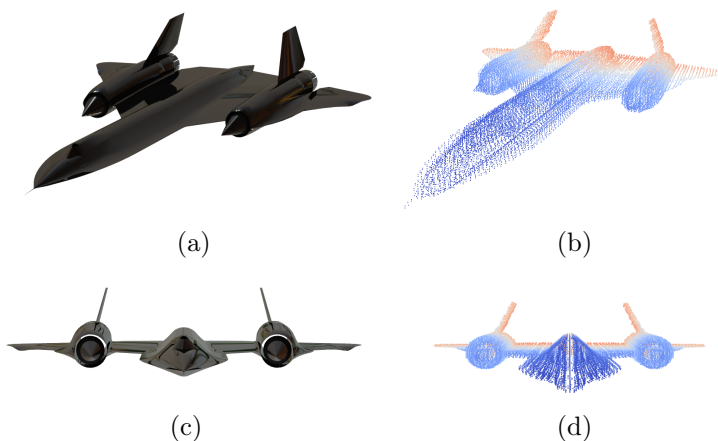
Figure 1.3: Generation of a 3-D complex geometry formed by particles using **GenCase** in DualSPHysics.

Particle approximation

Numerical discretization in meshfree particle methods involves approximating the values of functions, derivatives and integrals at a point (hereafter referred as particle) through neighbouring particles averaged contributions (also known as displacement interpolation). These contributions refer to a summation process by using the information from all the neighbours that have a significant influence on the particle considered. The area of influence of a particle is determined by the so-called support domain which may remain at a constant value or vary during the simulation evolve. Neighbouring particles within this zone provide all the necessary and sufficient information to predict eventual field variable values at the particle of interest.

For example, considering a field variable f evaluated at any particle $p(x_1, x_2)$, this function can be approximated or interpolated using values of neighbours $f(p^*)$'s within the support domain of p, i.e.

$$f^h(p) = \sum_{i \in S_n} \phi_i f_i(p^*) \tag{1.1}$$

where ϕ_i is a function (often called shape function). The evaluation of this special function depends on the information extracted from all particles evaluated within the support domain of p. S_n is the set of particles (p^*)'s included in a *"small local domain"* of p. Such local domain is commonly titled *"support domain"* in most of SPH literature. Neighbouring particles populating this zone are designated as *"support particles"*. Figure 1.4 exposes these concepts for a field variable calculation in 2D.
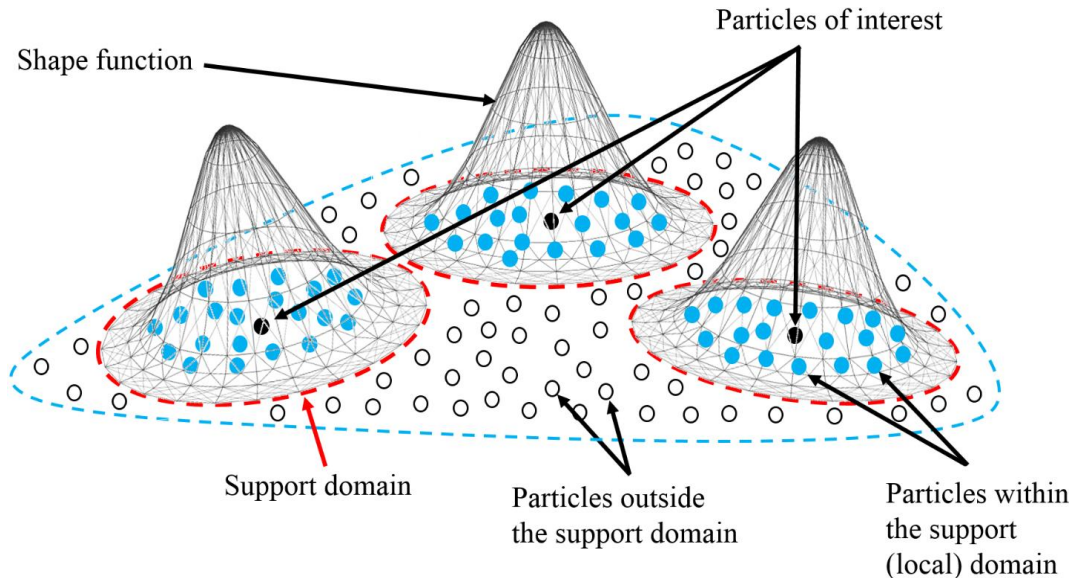
Figure 1.4: Domain representation of a 2D discretized domain and particles in a local weighted support domain.

1.4 Applications of the SPH method

From early applications of the SPH method, the most extensively addressed are exposed below. For a more detailed description of each subject consult (Liu and Liu, 2010a; Monaghan, 2012).

▶ **Astrophysics** (Firstly the main goal)
↪ Binary stars and stellar collisions (Benz, 1988; Monaghan, 1992; Rasio and Lombardi, 1999)
↪ Supernova (Hultman and Pharasyn, 1999; Thacker and Couchman, 2001)
↪ Collapse and formation of galaxies (Berczik, 2000; Monaghan and Lattanzio, 1991)
↪ Coalescence of black holes with neutron stars (Lee, 2000; Lee and Kluzniak, 1999)
↪ Single and multiple detonation of white dwarfs (García-Senz et al., 1999)
↪ Evolution of the universe (Monaghan, 1990)

▶ **Fluid dynamics**
↪ Multiphase flows (Colagrossi and Landrini, 2003; Hu and Adams, 2007; Mokos et al., 2014)
↪ Surface tension (Colagrossi, 2005; Hunter, 1992; Mokos et al., 2014; Monaghan, 1994)
↪ Liquid drops (Nugent and Posch, 2000)
↪ Generation of tsunamis (Monaghan and Kajtar, 2009)
↪ Rivers draining (Wells and Wettlaufer, 2005)
↪ Water wave impact (Crespo et al., 2007a; Dalrymple and Rogers, 2006; Gómez-Gesteira and Dalrymple, 2004)
↪ Dambreak (Crespo et al., 2008)
↪ Sloshing and overtopping (Iglesias et al., 2004; Shao et al., 2006; Souto-Iglesias et al., 2006)
↪ Heat and/or mass conduction (Chen et al., 1999; Cleary, 1998; Jeong et al., 2003; Jiang and Sousa, 2006; Rook et al., 2007)
↪ High explosive detonation and explosion (Liu and Liu, 2003; Liu et al., 2003c; Swegle and Attaway, 1995)
↪ Underwater explosions and water mitigation (Liu et al., 2002, 2003a)
↪ Fish-like swimming (Kajtar and Monaghan, 2010, 2008)
↪ Micro channels (Liu and Liu, 2005; Liu et al., 2003b)

▶ **Geophysical flow**
↪ Flood and river dynamics (Ghazali and Kamsin, 2008; Kipfer and Westermann, 2006)
↪ Landslides (Gallati et al., 2005; Pastor et al., 2009)
↪ Flow in fractures and porous media (Herrera et al., 2009; Tartakovsky and Meakin, 2006)

↪ Soil mechanics and mudflow (Bui et al., 2006, 2008; Laigle et al., 2007)

▶ **Solid mechanics**

↪ Elastic plastic flow (Gray et al., 2001; Libersky and Petschek, 1991; Libersky et al., 1993; Zhou et al., 2007)

↪ Fracture and impact (Benz and Asphaug, 1994, 1995; Das and Cleary, 2010; Gray and Monaghan, 2004; Jutzi et al., 2008)

↪ Metal forming and high pressure die casting (Bonet and Kulasegaram, 2000; Cleary et al., 2006; Cleary and Ha, 2000; Ha and Cleary, 2000, 2005)

↪ Soft tissues (Hieber and Koumoutsakos, 2008)

↪ Cross rheological model (Hosseini et al., 2007; Shao and Lo, 2003)

▶ **Non Newtonian flow**

↪ Blood behaviour (Müller et al., 2004; Tanaka and Takano, 2005; TSUB-OTA et al., 2006)

↪ Human organs (Hieber et al., 2004)

1.5 Objective and scope

The paramount objective of this thesis is to present the state of the art, the fundamentals and the implementation of the meshfree numerical technique called Smoothed Particle Hydrodynamics. This technique in its Weakly Incompressible version has been successfully applied in the solution of fluid solid interactions. The scope of the present work concerns problems related to the arbitrary motion of buoyant bodies and bodies with an imposed motion law. Therefore to achieve the main objective a remarkable initial point is to provide an introduction to the fundamentals of the SPH numerical methodology. Then the next essential point is to introduce a numerical code that implements the SPH method providing significant and reliable solutions. The numerical simulations are then carried out using DualSPHysics (Crespo et al., 2015) routines. This numerical code has been developed based upon the SPH methodology to simulate physical phenomena without the necessity of a meshing process. The code of DualSPHysics has been designed to extend its capabilities to the actual tendency of High Performance Computing (HPC), providing the simulations to be massively parallelized.

Thesis outline

From this section, throughout the subsequent chapters this work attends the following structure:

Chapter 2 describes schematically the physical models of the study cases. Three of them pertaining to the numerical validations, namely the square travelling linearly through a fluid, the fluid flow around a square cylinder, and the ascending motion of a cylinder submerged at an initial depth in a viscous fluid. Dimensions and parameters of each of their configurations are depicted. In addition, a general overview involving the principal study cases are exposed. The train passing through a tunnel at a high velocity and the submarine going up to the surface. For both study cases dimensions and initial parameters are assigned as well.

Chapter 3 describes the fundamental principles that govern the fluid dynamics upon the assumption of a Lagrangian scheme fluid model. Conservation equations, namely continuity and momentum are presented in their material approach considering low density variations.

Chapter 4 reviews the formality of the SPH method. The essential formulation and principal ideas are exposed, including more common derivative rules during the process of treating any function with SPH methodology. Furthermore the concept of smoothing function is extended and at the end of the chapter, the criteria to carry out the selection of smoothing functions is highlighted.

Chapter 5 depicts the process of discretizing the mathematical model that governs the physics of the problems of interest, namely the continuity and momentum equations. Then this chapter presents additional treatments commonly used in the SPH technique implementation in order to overcome shortcomings inherent to the numerical approach. To conclude the key ideas of the fluid solid interaction are describe in detail.

Chapter 6 addresses the validations of the SPH numerical technique with solutions published by other authors. Furthermore the results of the two main interesting study cases obtained using DualSPHysics, and important parameters regarding the numerical methodology are thoroughly discussed.

Chapter 7 finally presents the conclusion of this work, describing advantages, issues and pitfalls of implementing numerical approaches using SPH, in particular DualSPHysics for fluid solid interaction.

<div align="right">

2

</div>

Physical models

2.1 Flow around a moving square cylinder

This first study case regards the SPH numerical validation based upon the benchmark test case No.6 from the SPH European Research Interest Community (SPHERIC) web page http://spheric-sph.org/tests/test-6 see (Colagrossi, 2011). It is worth emphasizing that due to the existence of boundaries at a short distance from the geometry numerical errors may decrease the accuracy in numerical results. As a consequence the numerical domain was extended as shown in Figure 2.1 pretending to mimic a similar effect of a non-reflecting boundary as published by (Bouscasse et al., 2013). The square length L is equal to 1m, and its change in position is prescribed according to an imposed motion law showed in Figure 2.2. The gravity is considered negligible.
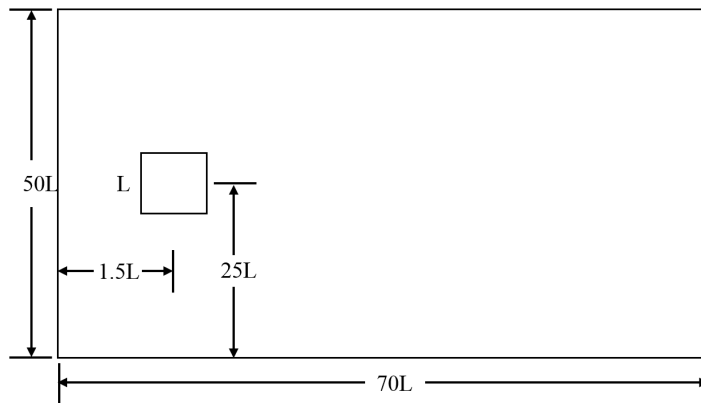
Figure 2.1: Initial set up of the moving square test case.
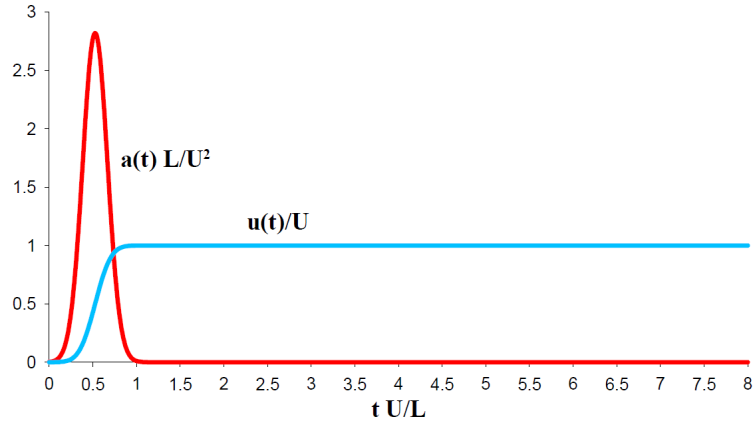
Figure 2.2: Motion law from benchmark test case.

The square cylinder is surrounded by a fluid at rest. The center of the geometry is located as previously indicated in Figure 2.1. Density is initialized with a value of $\rho = 1 \, \text{kg} \, \text{m}^{-3}$ and $\nu_o = 0.006666 \, \text{m}^2 \, \text{s}^{-1}$. The square cylinder starts an accelerated motion in the positive x-component direction, until a velocity of $U = 1 \, \text{m} \, \text{s}^{-1}$ is reached. Once this velocity value is is reached, it is maintained constant during the translational motion and plays the role of the characteristic velocity. The initial acceleration stage let the square move smoothly maintaining a considerable non disturbed media. The total trajectory described by the square cylinder lasts eight seconds from its starting point.

2.2 Flow around a fixed circular cylinder

For the second test case, the configuration of a circular cylinder fixed in space that perturbs the flow of a viscous fluid is executed. Similarly to the anterior case, the processing calculations have been accomplished by means of Dual-SPHysics. Figure 2.3 shows the general set up of the numerical domain and the location of the circular cylinder. The influence of the gravity is considered negligible like in the anterior case.
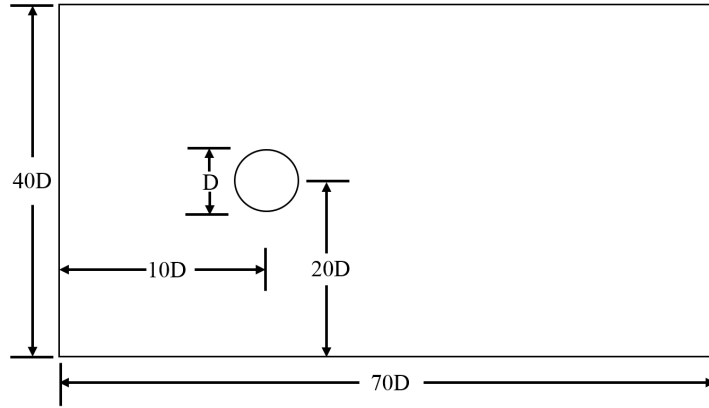
Figure 2.3: Initial set up of the fluid passing over a cylinder test case.

The free stream velocity is set to $U = 1 \, \mathrm{m \, s^{-1}}$. Boundaries are extended 20 times the cylinder diameter top and bottom so as to avoid the numerical calculations to be affected. Complementary, an extension of the space from the cylinder to the end of the container is required in order to permit the fluid patterns to be fully developed. It is worth mentioning that the left and right sides of the boundary numerical domain, are considered to behave as opened boundaries to guarantee a constant flow rate. Moreover the next consideration are assumed; the diameter of the cylinder is $D = 1 \, \mathrm{m}$, the fluid density is considered equal to $\rho = 1 \, \mathrm{kg \, m^{-3}}$, and finally $\nu_o = 0.01 \, \mathrm{m^2 \, s^{-1}}$.

2.3 Ascending motion of a cylinder in a viscous flow

The third case presents the results of the ascending motion of a circular cylinder departing from a specific depth from the free surface. The ascending motion of the cylinder is achieved due to the difference of densities of the cylinder and the media in which it is immersed. Since the cylinder is deemed as a floating body, a buoyant force governs the movement of the cylinder once the simulation starts. Figure 2.4 describes the model to be computed. Furthermore the numerical domain is also presented, where a distribution of particles is initialized to populate the fluid zone and the boundary regions as well.
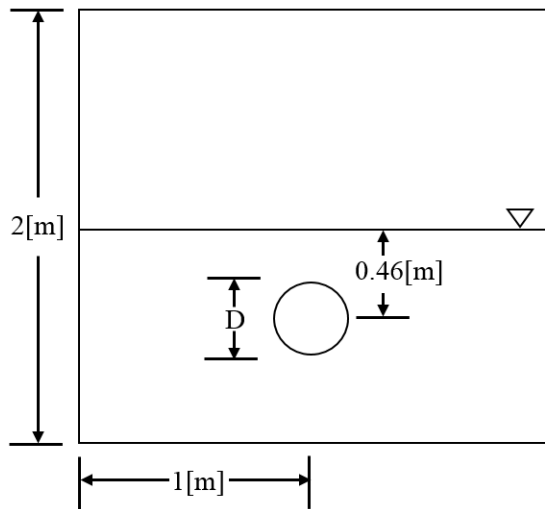
Figure 2.4: Dimensions and initial layout of a cylinder submerged in a viscous fluid.

At the beginning of the simulation the fluid is at rest, then at time $t = 0\,\text{s}$ due to the lower density value of the circular cylinder compared to that of the fluid, a sudden acceleration produce a change in position guided to the undisturbed free surface. Additional treatments for the free surface are not required, this will magnify the features of the SPH methodology as exposed later.

Important physical parameters involved in the experimental campaign are initialised as follows, a density value of $\rho_w = 998.2\,\text{kg}\,\text{m}^{-3}$ is assumed for the particles representing the fluid region. The diameter of the circular cylinder adopts a a value of $D = 0.30\,\text{m}$ and the position of its center is specified to be located $d = 0.46\,\text{m}$ under the fluid free surface. The density of the cylinder is considered $\rho_c = 0.62\rho_w\,\text{kg}\,\text{m}^{-3}$.

2.4   A single carriage train travelling through a tunnel

Figure 2.5 shows the model domain of the tunnel. Dimensions of the tunnel and train are taken from the experiment set up of (Ricco et al., 2007). Numerical extensions are collocated at the entry and exit of the tunnel so as to diminish the effects caused by high velocity at the entry of the train. The tunnel diameter is $D = 0.099$ m with a thickness of $t = 0.005$ m.
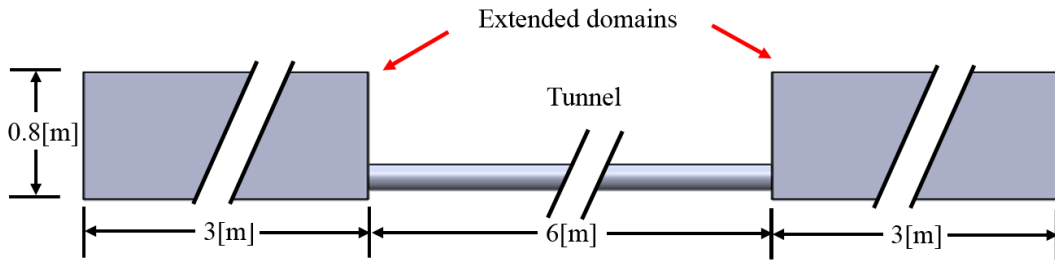
Figure 2.5: Side view of the tunnel configuration.
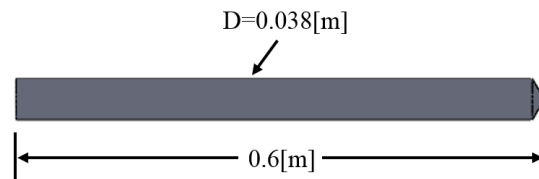
Figure 2.6: Train dimensions.

Train dimensions are presented in Figure 2.6 where the former part of the geometry has a conic angle of $\theta = 30$ deg measured between the axis and the directrix. The train initial location is $d = 1$ m from the tunnel entrance as shown in Figure 2.7. The diameter of the train and the tunnel are assumed to be concentric.
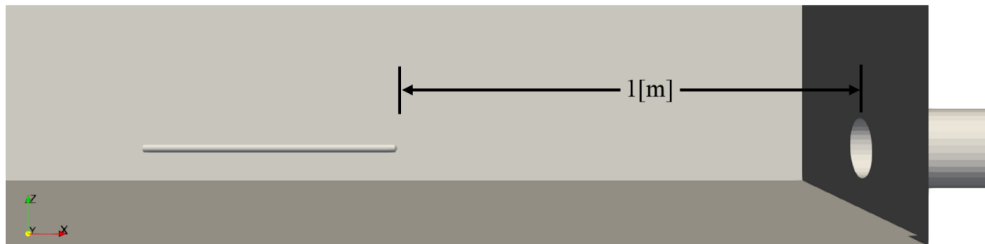
Figure 2.7: Train initial position.

19

The main objective of this study is to measure the pressure changes while the train is travelling through the tunnel at velocity equal to $v_x = 30.6 \text{ m s}^{-1}$. The goal pressure behaviour is that experimentally reported by (Ricco et al., 2007). To perform such a task, a numerical tool of planting particles at a certain distance from the tunnel entrance is assessed. The early work of (Ricco et al., 2007), set pressure sensors in order to capture the pressure variations during the stages of the phenomenon, namely, the entering to the tunnel, the train travelling, and the leaving of the train. These sensor are represented numerically by means of a set of material particles in the same locations as the real sensors are. Nevertheless just one measure particle numerical instrument is analysed. Figure 2.8 highlights the location of the numerical particle sensor of interest. During the simulation the next physical parameters are assumed; the fluid density is set as $\rho = 1.22 \text{ kg m}^{-3}$, and $\nu_o = 1.516 \times 10^{-5} \text{ m}^2 \text{ s}^{-1}$.
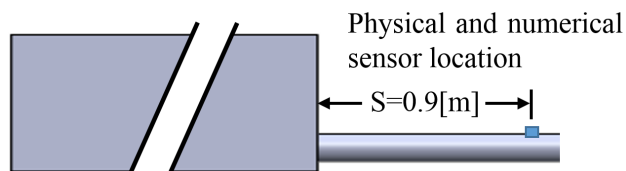
Figure 2.8: Sensor location for numerical particle measure tool.

The process of the train is as next; at the initial time $t = 0 \text{ s}$ the train initiate a vertical imposed motion in the x-component direction, with a velocity of $v_x = 30.6 \text{ m s}^{-1}$. Then the train travels inside the tunnel causing a pressure rising effect from its enter until it leaves the tunnel. Pressure variations are registered in order to compare and discuss the reliability of the meshless SPH method. In general regarding numerical simulations of high speed trains when they travel in a tunnel there exist two classical configurations, namely, just one single carriage train travelling along the tunnel at a high speed or two trains passing each other. This study is focused on the first configuration, assuming the single carriage train entering in a tunnel at a high velocity. Velocities achieved by nowadays high speed trains do not overcome the unity of the Mach number. In fact the fastest train belongs to the new categorize of MagLev (Magnetic Levitation) trains. Notwithstanding the high velocity these MagLev trains could reached, their velocity remains below the Mach number unity. It is worth mentioning that both categories, railways and MagLevs are numerically studied without considering the technique implemented to travel, instead dimensionless numbers like the length ratio, blockage ratio and the Mach number are considered. Such numbers are defined as follows:

$$L_r = L_{tunnel}/L_{train}, \quad \text{Length ratio}$$
$$B_r = A_{train}/A_{tunnel}, \quad \text{Blockage ratio}$$
$$M = V_{ref}/C_{sound}, \quad \text{Mach number}$$

For the present study case these numbers become,

$$L_r = 6\,\mathrm{m}/0.6\,\mathrm{m} = 10,$$
$$B_r = 0.0011\,\mathrm{m}/0.0076\,\mathrm{m} = 0.14,$$
$$M = 30.6\,\mathrm{m\,s^{-1}}/345\,\mathrm{m\,s^{-1}} = 0.088,$$

2.5 Ascending motion of a submarine hull

Regarding the numerical campaign for this study case, dimension are taken from Mackay (2003). In that technical report a standard scheme of a submarine hull is specified. Furthermore this report was the result of several experimental tests carried out in different facilities, oriented to Defence Research and Development in Canada. Experiments were prior accomplished either in wind tunnels or towing tanks and later numerically represented. Notwithstanding the good agreement between numerical simulations and experiments, all measurements are still acquired assuming static hydrodynamic loads. Such assumption does not represent the true behaviour which the submarine hull structures challenge under real emergency situations.

The main objective of this study concerns one of those challenging circumstances, namely a rolling stability issue when a submarine describes an emergency ascending motion, apparently caused by the tower like structure at the top of the submarine hull known as the sail. There exist some early works that attempt to capture the instability rolling movement like the early work of (Bettle et al., 2009) and more recently (Bettle et al., 2014b). Notwithstanding the good accuracy of the results, the used conventional numerical approaches seems to demand an additional computational time and effort when treating a meshing pre-process. Moreover a couple between equations of rigid body motion and fluid dynamics equations is demanded adding one more difficulty to conventional mesh-grid methods. In order to capture the real fluid solid interaction a buoyant body is considered to represent the submarine hull. To avoid additional treatments between the solid and the fluid, the calculations are performed according to fluid solid interaction presented in 5.3. Figure 2.9 illustrates the submarine general dimensions adopted in this study. Figure 2.10 shows complementary nose and tail parameters of the geometry. Important physical parameters are considered to be; $D = 0.2$ m, the fluid density is set $\rho_f = 1000\,\mathrm{kg\,m^{-3}}$, the submarine hull density $\rho_s = 0.9\rho_w\,\mathrm{kg\,m^{-3}}$, the kinematic viscosity $\nu_o = 1\mathrm{e} - 6$ $\mathrm{m^2\,s^{-1}}$. The initial layout is illustrated in Figures 2.11 and 2.12.

Figure 2.9: DRDC standard submarine geometry. Reproduced from Mackay (2003).

Nose:
- Length, $1.75D$
- Axisymmetric profile defined by:

$$\frac{r}{D} = 0.8685\sqrt{\frac{x_F}{D}} - 0.3978\frac{x_F}{D} + 0.006511\left(\frac{x_F}{D}\right)^2 + 0.005086\left(\frac{x_F}{D}\right)^3$$

where x_F is distance measured aft from the FP

Midbody:
- Length, $4D$
- Axisymmetric, with constant diameter D

Tail:
- Length, $3D$
- Axisymmetric parabolic profile:

$$\frac{r}{D} = \frac{1}{3}\left(\frac{x_A}{D}\right) - \frac{1}{18}\left(\frac{x_A}{D}\right)^2$$

where x_A is distance measured forward from the AP

Figure 2.10: Complemetary dimensions. DRDC standard submarine geometry. Reproduced from Mackay (2003).

Figure 2.11: Initial layout.
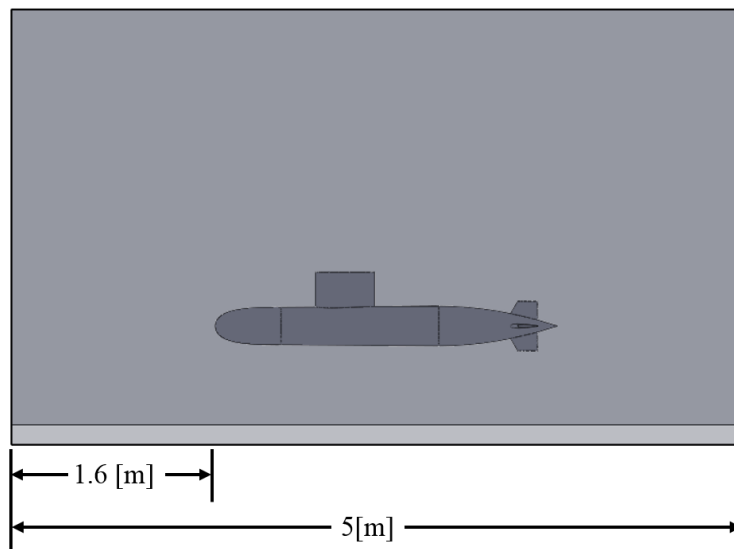
Figure 2.12: Initial layout.

The calculations pretended to be performed, are very related to the moments developed by the submarine hull. The nature of the media in which the submarine plays its role, supply the geometry with degrees of freedom that if they are not controlled, can exert undesirable rotations(instabilities). To speak in the same language Figure 2.13 illustrates the possible moments to be analysed, being for the present study that related to the rolling instability.
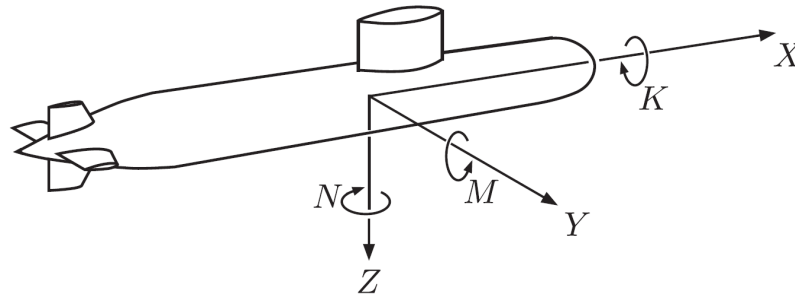
Figure 2.13: Moments for a 6 degree of freedom geometry, taken from Mackay (2003).

where N stands for the Yawing moment, M for the Pitching moment and finally K represents the Rolling moment.

3

Mathematical model

3.1 Governing equations

The mathematical apparatus in fluid mechanics for describing the behaviour of a fluid assumed incompressible are based upon a series of fundamental physical principles namely,

- ▶ Mass conservation.
- ▶ Momentum conservation.

and two representative schemes, early mentioned in chapter 1,

- ▶ Eulerian scheme.
- ▶ Lagrangian scheme.

depending on the adopted scheme, different mathematical representations (integral or differential forms) of fundamental physical principles are deduced. As the continuum assumption is considered, then any function variable is supported by all the theorems pertaining to the calculus.

The implementation of each of fundamental principles relies on the problem layout and the field variables information demanded. Considering a Lagrangian representation of the governing equations seems to be more suitable for this study, since the numerical methodology adopted was developed for such scheme. Henceforth the continuity equation deduced from the mass conservation principle is expressed as next (Anderson, 1995),

$$\frac{D\rho}{Dt} + \rho \nabla \cdot \boldsymbol{v} = 0, \tag{3.1}$$

and the momentum equation (Newton second law for fluid dynamics), considering a low density variations,

$$\frac{D\boldsymbol{v}}{Dt} = -\frac{1}{\rho}\nabla P + \frac{1}{\rho}\left(\nabla \cdot \rho\nu_o\nabla\right)\boldsymbol{v} + \boldsymbol{g} \tag{3.2}$$

Both equation appear in their material description i.e. the governing equations of fluid dynamics in the Lagrangian scheme. Additionally they appear in their Cartesian version. Observing the anterior equations they do not represent indeed a true model of a fully incompressible fluid. This is due to the Weakly Incompressible SPH approximation explained in later sections. The resulting system of governing equations are referred as the Navier Stokes equations.

4

The Smoothed Particle Hydrodynamics method

The Smoothed Particle Hydrodynamics method often referred as SPH, is a meshfree particle adaptive method that performs numerical approaches based on the Lagrangian scheme. A crucial characteristic of the metodology is that the entire computational domain turns into a set of distributed particles which posses material properties. Partial differential equations that govern the physical system are converted into their integral representation by means of a convolution. Then, the convolution of the function is manipulated according to the SPH methodology and discretized, leading to its particle representation. Individual particle behaviour becomes a function of the designated interpolation function, which performs a weighted average of all the values of the nearest particles surrounding the particle of interest. Such average is carried out by a summation process of the information held on each neighbour particle. Physical variables of interest are computed implementing such interpolation as well.

In this chapter a brief introduction to the formality of SPH will be briefed. Basic concepts, and mathematical formulation to obtain the SPH approximation for PDEs are explained. Furthermore, issues related to the formulation are highly discussed, and finally the construction process of interpolation function are carried out.

The SPH method was first introduced and formulated by (Gingold and Monaghan, 1977; Lucy, 1977) to solve astrophysical problems. Since then SPH has been extensively studied and extended to distinct fields. In this study the SPH method will be implemented concerning the field of Computational Fluid Dynamics. Figure 4.1 summarizes a general classification of the SPH method.
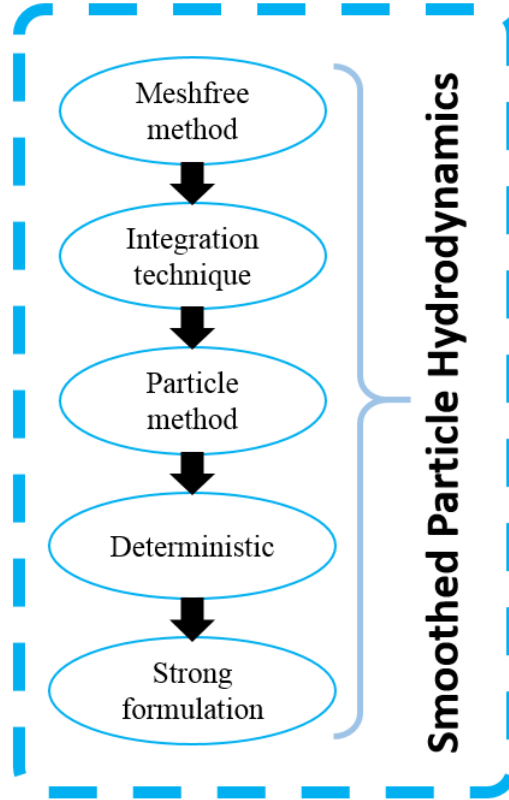
Figure 4.1: General classification of the SPH method.

The calculation process during the numerical simulations presented in later chapters were obtained using the DualSPHysics software(Crespo et al., 2015). Based on a weakly incompressible meshfree particle approach, this software has been extended to a vast variety of applications, particularly in hydrodynamics problems.

4.1 Formality of SPH

Pertaining to those methods based on the Integration technique, the SPH methodology solves governing equations by means of a integral representation. Such a straightforward process consists on passing the differential operator acting on a given field function to an interpolating function (best known as kernel function).

This action reduces the requirement on the order of consistency of the approximated field functions, turning SPH into a *weak-like formulation* (Liu, 2009).

The integral representation is performed through a convolution of field functions like density, velocity, pressure, etc. For a better understanding of the theoretical foundation[1] of the SPH method it is often necessary a high mathematical background, since a variety of abstract concepts are required to stablish a basis from which the methodology is able to justify its performance, accuracy, convergence, limitations, and novel applications. As an attempt to exhibit a general overview of the mathematical background (that is regularly a requirement to get introduced in numerical methods), Figure 4.2 highlights the path to be followed for those interested on this sorts of topics.
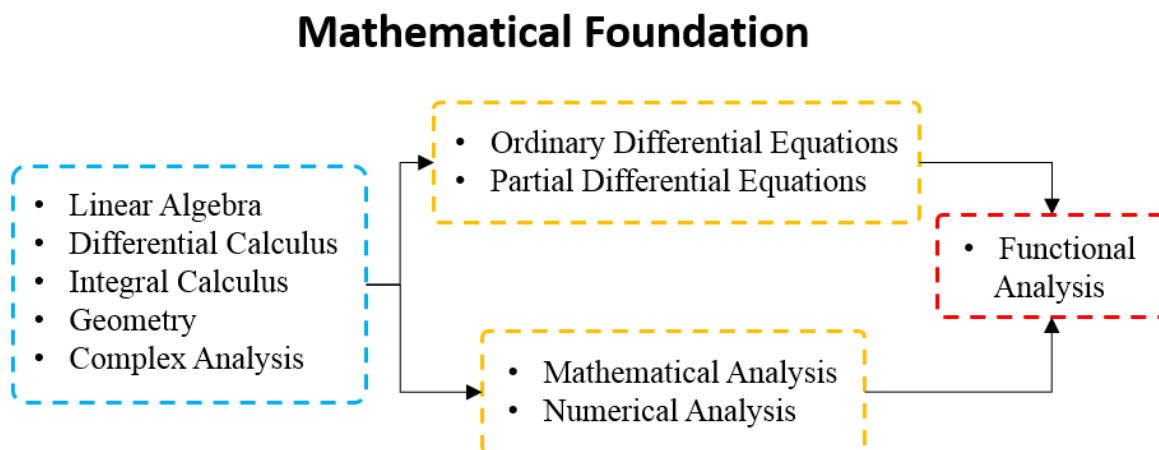
Figure 4.2: Topic basis for understanding numerical methods.

Supposing an acceptable level of math, the next sections present the essential SPH formulation.

4.2 Essential formulation

The essential formulation of SPH relies mainly in two very important steps, *"The integral representation"*, and *"The particle approximation"*.

The integral representation (subsequently titled kernel approximation) of the field functions, consists of applying the convolution of a given arbitrary function or derivative, with a weight(smoothing) function. The smoothing

---

[1] Introductory concepts and a detailed explanation of the mathematical formality of meshfree methods is addressed in (Liu, 2009; Liu and Zhang, 2013)

function is designated as the *kernel* or *kernel function*. Given any arbitrary function (material quantity) f evaluated on a particle i (whose position vector is r_i), i.e. $f(r_i)$, the interpolation via a convolution in SPH is such that,

$$\langle f(r_i) \rangle = \int_{\partial\Omega} f(r_j)\delta(r_i - r_j)dr_j, \tag{4.1}$$

where $\langle \cdot \rangle$ stands for the averaging operator, $\delta(r_i - r_j)$ is the Dirac delta function, and $\partial\Omega$ denotes the domain that contains r_i. Equation (4.1) is a point support representation of function f due to the nature of the Dirac delta function, therefore such equation cannot be implemented for establishing numerical models (Liu and Liu, 2010b; Monaghan, 1992). In order for the latter equation to be more suitable in a numerical approach, the Delta function is replaced by a smoothing function $W(r_i - r_j, h)$ with a finite spatial dimension defined by h, which is called smoothing length and represents the *support domain*(coming up in the next sections) of *W*.

The equation (4.1), then becomes,

$$\langle f(r_i) \rangle = \int_{\partial\Omega} f(r_j)W(r_i - r_j, h)dr_j, \tag{4.2}$$

from (4.2), $W(r_i - r_j, h)$ is demanded to satisfy the next conditions: for a constant smoothing length $h> 0$.

1. *Positivity,* $\quad \int_{\partial\Omega} W(r_i - r_j, h) > 0 \quad \forall j \in \partial\Omega,$

2. *Compact support,* $\quad W(r_i - r_j, h) = 0 \quad \forall j \in \partial\Omega^c,$

3. *Unity,* $\quad \int_{\partial\Omega} W(r_i - r_j, h)dr_j = 1, \quad \forall j \in \partial\Omega,$

4. *Delta function property,* $\quad \lim_{h \to 0} W(r_i - r_j, h) = \delta(r_i - r_j),$

5. *Decay,* $\quad (r_i - r_j) \leq (r_i - r_k) \Rightarrow W(r_i - r_j, h) \geq W(r_i - r_k, h) \quad \forall j, k \in \partial\Omega,$

6. *Symmetric,* $\quad W(r_i - r_j, h) = W(-(r_i - r_j), h),$

7. *Smoothness,* $W(r_i - r_j, h)$ *should be sufficiently smooth.*

Other manner to express condition 2 is,

$$W(r_i - r_j, h) = 0 \quad when \quad |r_i - r_j| > kh,$$

where k is a constant related to the smoothing function for a point at r_i, and defines the effective area of such function. This effective area is called the support domain, and will be clarified in this section.

As it is always quoted in numerical methods, a classification in the order of accuracy based on the order of the derivative (truncation error), exposes either the *diffusive* or *dispersive* nature of any method. Carrying out an expansion in Taylor series of eq.(4.2), makes evident that the truncation error is of second order of accuracy, leading the methodology to a diffusive scheme see (Liu and Liu, 2003). One of the primary objectives of this section is to explain the process of the SPH formulation applied to functions like derivative operators. This task often corresponds to the first contact with the method, however there is a need of experience, skills, and tricks, that are not taught in literature, but emphasized to acquire. The methodology starts similarly to eq.(4.2), but the function $\left\langle f(r_i) \right\rangle$ is replaced by $\left\langle \dfrac{\partial f(r_i)}{\partial x_i} \right\rangle$, then,

$$\underbrace{\left\langle \frac{\partial f(r_i)}{\partial x_i} \right\rangle}_{\text{Any function evaluated in } i} = \underbrace{\int_{\partial\Omega} \frac{\partial f(r_j)}{\partial x_j} W(r_i - r_j, h) dr_j,}_{\text{The integral of the same function evaluated in } j, \text{ multiplied by } W}$$

(4.3)

Keeping the anterior process in mind, and generalizing,

$$\left\langle \nabla \cdot \boldsymbol{f}(r_i) \right\rangle = \int_{\partial\Omega} \left(\nabla \cdot \boldsymbol{f}(r_j) \right) W(r_i - r_j, h) dr_j, \tag{4.4}$$

where the derivative of the integral is operated with respect to the j-th coordinate. Now considering the next identity, and substituting in the previous equation,

$$\begin{aligned}
\left[\nabla \cdot \boldsymbol{f}(r_j) \right] W(r_i - r_j, h) =& \nabla \cdot \left[\boldsymbol{f}(r_j) W(r_i - r_j, h) \right] \\
& - \boldsymbol{f}(r_j) \cdot \nabla \left[W(r_i - r_j, h) \right],
\end{aligned} \tag{4.5}$$

substituting in eq.(4.4),

$$\begin{aligned}
\left\langle \nabla \cdot \boldsymbol{f}(r_i) \right\rangle =& \int_{\partial\Omega} \nabla \cdot \left[\boldsymbol{f}(r_j) W(r_i - r_j, h) \right] dr_j \\
& - \int_{\partial\Omega} \boldsymbol{f}(r_j) \cdot \nabla \left[W(r_i - r_j, h) \right] dr_j,
\end{aligned} \tag{4.6}$$

using the divergence theorem in the first integral on the right hand side of (4.6), in order to integrate over the surface of the domain of integration,

$$\begin{aligned}
\left\langle \nabla \cdot \boldsymbol{f}(r_i) \right\rangle =& \int_{S} \boldsymbol{f}(r_j) W(r_i - r_j, h) \cdot \boldsymbol{n} dS \\
& - \int_{\partial\Omega} \boldsymbol{f}(r_j) \cdot \nabla \left[W(r_i - r_j, h) \right] dr_j,
\end{aligned} \tag{4.7}$$

As the smoothing function is defined to have a compact support, the first integral on the right hand side becomes zero while considering particles inside

the entire domain, otherwise a truncation of the smoothing function should be applied for particles near/in the boundaries, consequently the order of the kernel approximation via a Taylor expansion becomes larger and the first integral is no longer zero. Considering the first case eq.(4.7) becomes,

$$\langle \nabla \cdot \boldsymbol{f}(r_i) \rangle = - \int_{\partial \Omega} \boldsymbol{f}(r_j) \cdot \nabla \left[W(r_i - r_j, h) \right] dr_j, \qquad (4.8)$$

Equations (4.2) and (4.8), are examples of how the SPH method is applied on arbitrary functions, in this case a function and its derivative, respectively. From this section forward any function representation obtained through the anterior process will be referred as *kernel approximation.*

The particle approximation is the next step to be exerted after the kernel approximation. To achieve this, the entire (continuous)domain is subdivided in material particles that carries individual mass and occupy individual space. This process is called *discretization*, and it is performed once the equations (4.2) and (4.8) have been obtained, then integral equations previously presented are converted into its discretized forms of summation over all the particles in the support domain h of the kernel W. The corresponding discretized process of summation over the particles is commonly known as particle approximation. The particle approximation is implemented as follows. Beginning with equation (4.2),

$$\langle f(r_i) \rangle = \int_{\partial \Omega} f(r_j) W(r_i - r_j, h) dr_j, \qquad (4.9)$$

if the infinitesimal volume dr_j, in the above integration at the location of particle j is replaced by the finite volume of a particle $\triangle V(r_j)$ that is related to the particle $m(r_j)$ by the equality,

$$m(r_j) = \triangle V(r_j) \rho(r_j), \quad \forall j \in \partial \Omega \qquad (4.10)$$

where $\rho(r_j)$ is the density of particle j. Now from eq.(4.9),

$$\begin{aligned}
\langle f(r_i) \rangle &= \int_{\partial \Omega} f(r_j) \left[W(r_i - r_j, h) \right] dr_j, \\
&\approx \sum_j^N f(r_j) W(r_i - r_j, h) \triangle V(r_j), \\
&\approx \sum_j^N f(r_j) W(r_i - r_j, h) \frac{\rho(r_j)}{\rho(r_j)} \triangle V(r_j), \\
&\approx \sum_j^N f(r_j) W(r_i - r_j, h) \frac{(\rho(r_j) \triangle V(r_j))}{\rho(r_j)}, \\
&\approx \sum_j^N f(r_j) W(r_i - r_j, h) \frac{m(r_j)}{\rho(r_j)},
\end{aligned}$$

finally,

$$f(r_i) = \sum_j^N \frac{f(r_j)}{\rho(r_j)} W(r_i - r_j, h) m(r_j), \quad \forall j \in \partial\Omega \qquad (4.11)$$

Following the same argument, the particle approximation can be achieved for the spatial derivative operator. Remembering eq.(4.8),

$$
\begin{aligned}
\langle \nabla \cdot \boldsymbol{f}(r_i) \rangle &= -\int_{\partial\Omega} \boldsymbol{f}(r_j) \cdot \nabla \left[W(r_i - r_j, h) \right] dr_j, \\
&\approx -\sum_j^N \boldsymbol{f}(r_j) \cdot \nabla W(r_i - r_j, h) \triangle V(r_j), \\
&\approx -\sum_j^N \boldsymbol{f}(r_j) \cdot \nabla W(r_i - r_j, h) \frac{\rho(r_j)}{\rho(r_j)} \triangle V(r_j), \\
&\approx -\sum_j^N \boldsymbol{f}(r_j) \cdot \nabla W(r_i - r_j, h) \frac{(\rho(r_j) \triangle V(r_j))}{\rho(r_j)}, \\
&\approx -\sum_j^N \boldsymbol{f}(r_j) \cdot \nabla W(r_i - r_j, h) \frac{m(r_j)}{\rho(r_j)},
\end{aligned}
$$

resulting,

$$\nabla \cdot \boldsymbol{f}(r_i) = -\sum_j^N \frac{\boldsymbol{f}(r_j)}{\rho(r_j)} \cdot \nabla W(r_i - r_j, h) m(r_j), \qquad (4.12)$$

or more specific with the spatial derivative of the RHS with respect to r_i,

$$\nabla_i \cdot \boldsymbol{f}(r_i) = -\sum_j^N \frac{\boldsymbol{f}(r_j)}{\rho(r_j)} \cdot \nabla_j W(r_i - r_j, h) m(r_j), \quad \forall j \in \partial\Omega \qquad (4.13)$$

4.2.1 Shape of a smoothing function

According to (Li and Liu, 2002), smoothing functions are preferred to be symmetric so that many important properties like conservation of linear momentum and energy can be verified. Then most of the smoothing functions present the next form:

$$W(\mathbf{r_{ij}}, h) = \frac{1}{h^d} f\left(\frac{||\mathbf{r_{ij}}||}{h}\right) \qquad (4.14)$$

where d is the spatial dimension, and $\mathbf{r_{ij}} = r_{ij}\boldsymbol{i}_i = (r_i - r_j)\boldsymbol{i}_i$.

Now using the euclidean norm defined as $||\mathbf{r_{ij}}|| := \sqrt{(r_i - r_j)\boldsymbol{i}_i \cdot (r_i - r_j)\boldsymbol{i}_i}$,

and differentiating eq.(4.14) with respect to r_i, by chain rule,

$$\nabla_i W(r_{ij}, h) = \frac{\partial W(||\mathbf{r_i} - \mathbf{r_j}||, h)}{\partial r_i} \boldsymbol{i}_i, \tag{4.15}$$

$$= \frac{\partial W(||\mathbf{r_i} - \mathbf{r_j}||, h)}{\partial ||\mathbf{r_i} - \mathbf{r_j}||} \frac{\partial ||\mathbf{r_i} - \mathbf{r_j}||}{\partial r_i} \boldsymbol{i}_i,$$

$$= \frac{\mathbf{r_{ij}}}{||\mathbf{r_{ij}}||} \frac{\partial W(||\mathbf{r_i} - \mathbf{r_j}||, h)}{\partial ||\mathbf{r_i} - \mathbf{r_j}||}, \tag{4.16}$$

from the above a very effective identity can be obtained,

$$\nabla_i W(r_{ij}, h) = \frac{\mathbf{r_{ij}}}{||\mathbf{r_{ij}}||} \frac{\partial W(||\mathbf{r_i} - \mathbf{r_j}||, h)}{\partial ||\mathbf{r_{ij}}||},$$

$$= -\frac{\mathbf{r_{ji}}}{||\mathbf{r_{ji}}||} \frac{\partial W(||\mathbf{r_i} - \mathbf{r_j}||, h)}{\partial ||\mathbf{r_i} - \mathbf{r_j}||},$$

$$= -\nabla_j W(r_{ij}, h), \tag{4.17}$$

finally, substituting eq.(4.17), into eq.(4.13),

$$\nabla_i \cdot \boldsymbol{f}(r_i) = -\sum_j^N \frac{\boldsymbol{f}(r_j)}{\rho(r_j)} \cdot \nabla_j W(r_i - r_j, h) m(r_j),$$

$$= \sum_j^N \frac{\boldsymbol{f}(r_j)}{\rho(r_j)} \cdot \left(-\nabla_j W(r_i - r_j, h) \right) m(r_j),$$

$$= \sum_j^N \frac{\boldsymbol{f}(r_j)}{\rho(r_j)} \cdot \nabla_i W(r_i - r_j, h) m(r_j).$$

thus,

$$\nabla_i \cdot \boldsymbol{f}(r_i) = \sum_j^N \frac{\boldsymbol{f}(r_j)}{\rho(r_j)} \cdot \nabla_i W(r_i - r_j, h) m(r_j). \tag{4.18}$$

showing that, the spatial derivative of any function in its particle approximation is highly dependent on the spatial derivative of the smoothing function. Furthermore the minus sign that appears in a SPH discretization can be eliminated using eq.(4.17). Finally, before the average operator can be applied to the equations of fluid dynamics, some of its properties (Liu and Liu, 2003), are highlighted below,

Given two arbitrary functions $f(r_i)$, $f(r_j)$, and a constant c the next operations exist,

$$\langle f(r_i) + f(r_j) \rangle = \langle f(r_i) \rangle + \langle f(r_j) \rangle \tag{4.19}$$

and,

$$\langle f(r_i) f(r_j) \rangle = \langle f(r_i) \rangle \langle f(r_j) \rangle \tag{4.20}$$

it can be shown straightforward that the next properties are satisfied,

$$\langle f(r_i) + f(r_j) \rangle = \langle f(r_j) + f(r_i) \rangle \tag{4.21}$$

$$\langle f(r_i)f(r_j) \rangle = \langle f(r_j)f(r_i) \rangle \tag{4.22}$$

$$\langle cf(r_i) \rangle = c\langle f(r_i) \rangle \tag{4.23}$$

4.3   SPH differentiation rules

There are some issues related when deriving the SPH version of any given function like in (4.18). Two different techniques are presented to overcome such issues, the *product-like*, and *quotient-like* SPH function conversions (Monaghan, 1992). The next results are derived using such techniques; first the conversion of the divergence operator into SPH methodology through each technique is exposed. Furthermore in appendix B, an alternative procedure to obtain the SPH version of the gradient operator is provided according to (E. Danis et al., 2013). Both methods yield the same results and can be applied analogously.

4.3.1   Product-like SPH function conversion

Considering the divergence of the next product,

$$\nabla \cdot (\rho(r_i)\boldsymbol{f}(r_i)) = \rho(r_i)(\nabla \cdot \boldsymbol{f}(r_i)) + \boldsymbol{f}(r_i) \cdot (\nabla \rho(r_i)) \tag{4.24}$$

and isolating the second term of the anterior equation,

$$\nabla \cdot \boldsymbol{f}(r_i) = \frac{1}{\rho(r_i)} \Big(\nabla \cdot (\rho(r_i)\boldsymbol{f}(r_i)) - \boldsymbol{f}(r_i) \cdot (\nabla \rho(r_i)) \Big) \tag{4.25}$$

applying now (4.18) to each derivative term of the right hand side of eq.(4.25),

$$
\begin{aligned}
\nabla_i \cdot \boldsymbol{f}(r_i) =& \frac{1}{\rho(r_i)} \Big[\sum_j^N \frac{(\rho(r_j)\boldsymbol{f}(r_j))}{\rho(r_j)} \cdot \nabla_i W(r_i - r_j, h)m(r_j) \\
& - \boldsymbol{f}(r_i) \cdot \Big(\sum_j^N \frac{\rho(r_j)}{\rho(r_j)} \nabla_i W(r_i - r_j, h)m(r_j) \Big) \Big], \\
=& \frac{1}{\rho(r_i)} \Big[\sum_j^N \boldsymbol{f}(r_j) \cdot \nabla_i W(r_i - r_j, h)m(r_j) \\
& - \boldsymbol{f}(r_i) \cdot \Big(\sum_j^N \nabla_i W(r_i - r_j, h)m(r_j) \Big) \Big], \\
=& \frac{1}{\rho(r_i)} \Big[\sum_j^N m(r_j)\big(\boldsymbol{f}(r_j) - \boldsymbol{f}(r_i)\big) \Big] \cdot \nabla_i W(r_i - r_j, h),
\end{aligned}
$$

results the *product-like SPH conversion* of the divergence operator,

$$\nabla_i \cdot \boldsymbol{f}(r_i) = \frac{1}{\rho(r_i)} \Big[\sum_j^N m(r_j) \big(\boldsymbol{f}(r_j) - \boldsymbol{f}(r_i) \big) \Big] \cdot \nabla_i W(r_i - r_j, h). \qquad (4.26)$$

4.3.2 Quotient-like SPH function conversion

Beginning with the next identity,

$$\nabla \cdot \left(\frac{\boldsymbol{f}(r_i)}{\rho(r_i)} \right) = \frac{\nabla \cdot \boldsymbol{f}(r_i)}{\rho(r_i)} - \frac{\boldsymbol{f}(r_i) \cdot \nabla \rho(r_i)}{\rho(r_i)^2}, \qquad (4.27)$$

and isolating the second term from the right hand side,

$$\nabla \cdot \boldsymbol{f}(r_i) = \rho(r_i) \left[\nabla \cdot \left(\frac{\boldsymbol{f}(r_i)}{\rho(r_i)} \right) + \frac{\boldsymbol{f}(r_i) \cdot \nabla \rho(r_i)}{\rho(r_i)^2} \right], \qquad (4.28)$$

once again, the next step consists of applying (4.18) to each derivative term from the right hand side of eq.(4.28),

$$\nabla_i \cdot \boldsymbol{f}(r_i) = \rho(r_i) \Bigg[\sum_j^N \frac{\left(\dfrac{\boldsymbol{f}(r_j)}{\rho(r_j)} \right)}{\rho(r_j)} \cdot \nabla_i W(r_i - r_j, h) m(r_j) \Bigg]$$

$$+ \frac{\boldsymbol{f}(r_i)}{\rho(r_i)^2} \cdot \Bigg[\sum_j^N \frac{\rho(r_j)}{\rho(r_j)} \nabla_i W(r_i - r_j, h) m(r_j) \Bigg],$$

$$= \rho(r_i) \Bigg[\sum_j^N \frac{\boldsymbol{f}(r_j)}{\rho(r_j)^2} \cdot \nabla_i W(r_i - r_j, h) m(r_j) \Bigg]$$

$$+ \frac{\boldsymbol{f}(r_i)}{\rho(r_i)^2} \cdot \Bigg[\sum_j^N \nabla_i W(r_i - r_j, h) m(r_j) \Bigg],$$

$$= \rho(r_i) \Bigg[\sum_j^N m(r_j) \left(\frac{\boldsymbol{f}(r_j)}{\rho(r_j)^2} + \frac{\boldsymbol{f}(r_i)}{\rho(r_i)^2} \right) \cdot \nabla_i W(r_i - r_j, h) \Bigg],$$

therefore eq.(4.28) becomes,

$$\nabla_i \cdot \boldsymbol{f}(r_i) = \rho(r_i) \Bigg[\sum_j^N m(r_j) \left(\frac{\boldsymbol{f}(r_j)}{\rho(r_j)^2} + \frac{\boldsymbol{f}(r_i)}{\rho(r_i)^2} \right) \cdot \nabla_i W(r_i - r_j, h) \Bigg]. \qquad (4.29)$$

Following (Li and Liu, 2002), the last equation better represents the principle of momentum conservation, and for this reason this representation of the divergence operator will be adopted.

4.3.3 Additional concepts

In previous sections the kernel function denoted by $W(r_i - r_j, h)$ has been extensively described and incorporated into the SPH formulation. Actually, referring to subsection 1.3, this kernel plays the role of the early mentioned *support domain*. In addition to this, the concept of *influence domain* is extended below and both concepts are linked to the their analogous meaning in the SPH terminology. Figures 4.3(a) and 4.3(b) illustrate the global idea of the aforementioned domains.

(a)

(b)
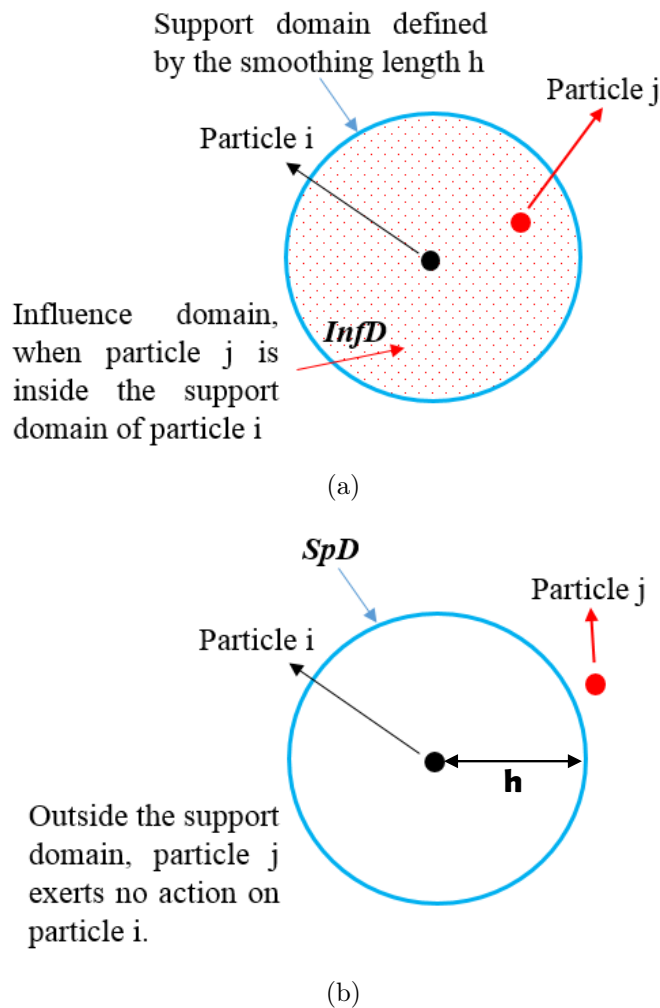
Figure 4.3: Support domain SpD(coloured with blue),and Influence domain $InfD$(showed with points in red colour).

The Support domain is defined as the region from which the information from all the particles $p(r_j)$ inside this zone contributes to obtain information and predict future behaviour of a particle with vector position r_i. Particles carry material properties and they move according to the information obtained from their neighbours via a the kernel $W(r_i - r_j, h)$. This concept becomes

relevant when treating a field variable evaluation.

The Influence domain is defined as the region from which a particle $p(r_j)$ exerts its influence onto the particle of interest $p(r_i)$. When the concept of influence domain is used, concerns only particles inside the kernel. In other words Support and Influence domain seem to be the same when particle j pertains to the support domain of particle i Figure 4.3(a). Otherwise no Influence domain exist at all as in the case of Figure 4.3(b).

4.4 Smoothing functions

Smoothing/Kernel functions are the main core of the SPH methodology; these functions perform the task of measuring the influence of any particle inside the support domain of the particle of interest, so as to assign an average value of the material property that the particle of interest carries with it. Depending on the distance from each of one of the particles to the main particle, the interaction will be stronger when the distance between them is short, and it will decrease monotonically as introduced in previous sections.

Every numerical method meets the challenging task of achieving a numerical representation of a physical phenomenon; this relates one of the most important issues of a numerical method to be satisfied, namely the consistency, since it guarantees how well the methodology has the ability to exactly represent governing equations. In order to achieve consistency in SPH, it is necessary for a kernel to reproduce a function, and its derivatives at a given order. Regarding SPH method the consistency appears during two of the SPH essential steps, namely the *kernel*, and *particle* approximations.[2]

4.4.1 Selection of smoothing functions

Construction of kernels is mostly related to how well the kernel is defined, so that it mimics the Dirac Delta function behaviour when the smoothing length tends to zero in the limit. Generally, functions that are chosen for this purpose might have the shape of polynomials or piecewise functions. In (Liu and Liu, 2003) is exposed a more in-depth explanation about the entire process of kernels construction; the entire process is constrained to satisfy conditions for consistency as previously mentioned. In this section some of the more implemented piecewise kernels are shown so their derivatives, and finally a justification of the kernel to be used during the calculations is presented.

---

[2] In (Liu, 2002), a detailed explanation about conditions for consistency in SPH can be found.

Quartic Kernel

Proposed by (Lucy, 1977), and defined as next:

$$W(r_i - r_j, h) = \alpha_d \begin{cases} (1 + 3q)(1 - q)^3 & q \leqslant 1 \\ 0 & q > 1 \end{cases} \tag{4.30}$$

where $q = \dfrac{|r_i - r_j|}{h}$,

The number α_d, is equal to $5/4h$, $5/\pi h^2$, and $105/16\pi h^3$ in one-, two-, and three- dimensional domain respectively. It is worth mentioning that α_d is known as the dimensional factor, and assures that the kernel functions satisfy the unity condition (Liu and Liu, 2003). Figure 4.4 shows the Quartic kernel function, and its first derivative.
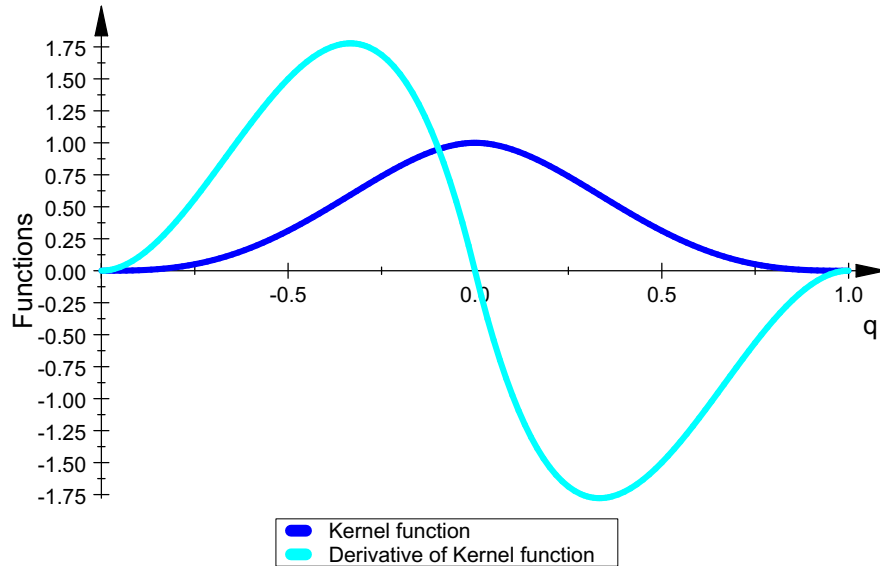
Figure 4.4: Quartic Kernel.

(a)

(b)

(c)

(d)
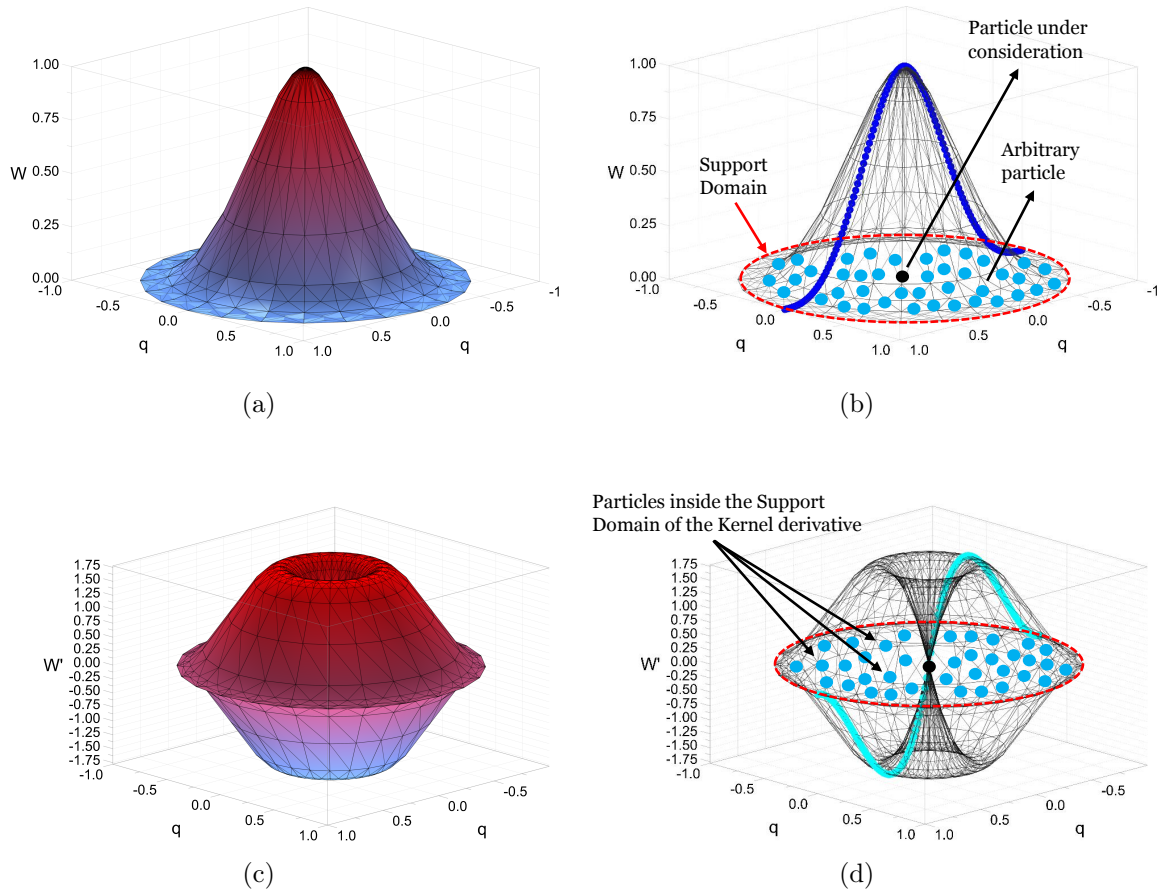
Figure 4.5: Quartic Kernel, and its first derivative as it might look like during a 2D calculation.

Figures 4.5(a) and 4.5(c), exhibit the surface representation of the Quartic kernel while Figures 4.5(b) and 4.5(d), present in a more comprehensible form, the main idea of a particle interaction inside the compact support domain of the kernel and its derivative respectively.

Gaussian Kernel

This kind of kernel was proposed by (Monaghan, 1992), this work also specifies that, in order to find a physical interpretation of a SPH equation representation, the implementation of this kernel is preferred. The Gaussian kernel is defined as next:

$$W(r_i - r_j, h) = \alpha_d e^{-q^2} \tag{4.31}$$

where α_d, is equal to $11/\pi^{1/2}h$, $1/\pi h^2$, and $1/\pi^{3/2}h^3$ in one-, two-, and three-dimensional domain respectively. In Figure 4.6 the Gaussian kernel and its derivative are plotted.
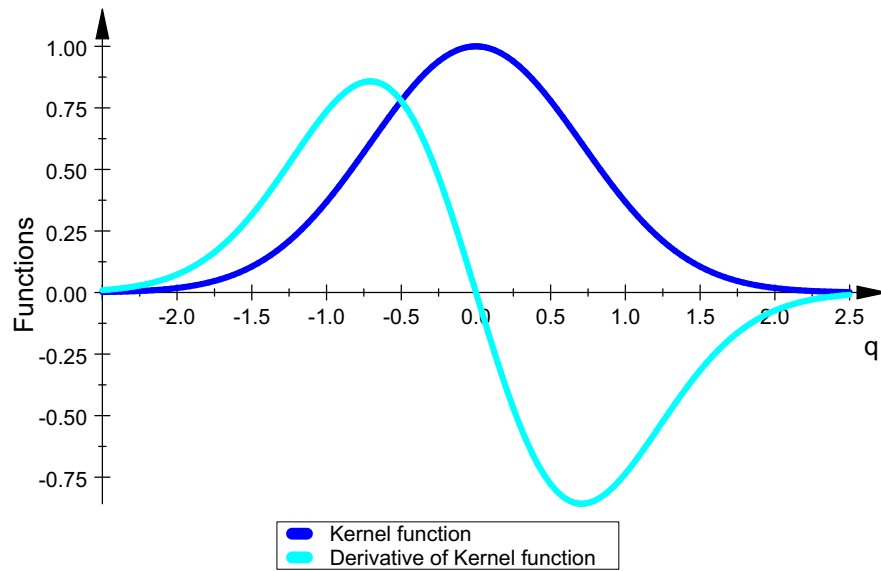
Figure 4.6: Gaussian Kernel.

(a)

(b)

(c)

(d)
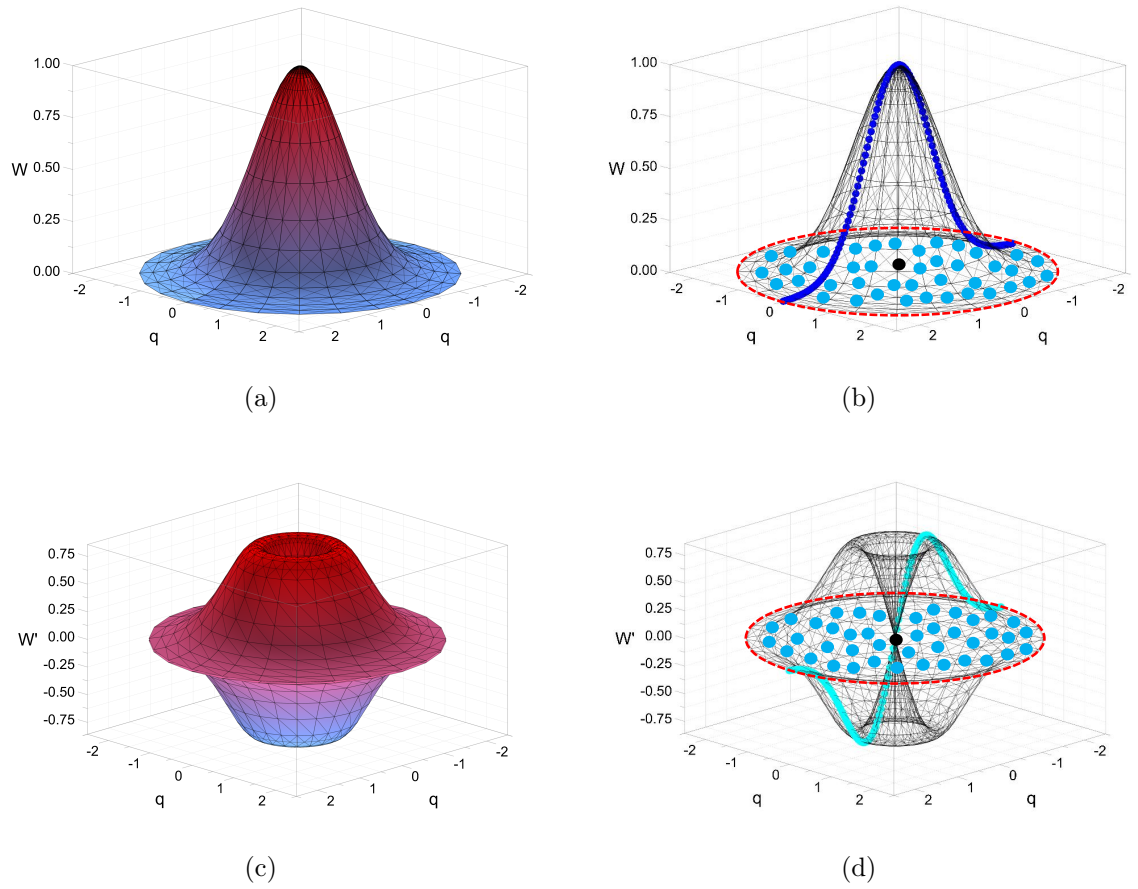
Figure 4.7: Gaussian Kernel, and its first derivative as it might look like during a 2D calculation.

Figures 4.7(a) and 4.7(c), shows the surface representation of the Gaussian kernel, on the other hand Figures 4.7(b) and 4.7(d), present the main idea of a particle interaction inside the compact support domain of the kernel and its derivative respectively.

Cubic Kernel

(Monaghan and Lattanzio, 1985) derived a Cubic kernel through spline functions implementation. This kernel is expressed as next:

$$W(r_i - r_j, h) = \alpha_d \begin{cases} (2/3) - q^2 + (1/2)q^3 & 0 \le q < 1 \\ (1/6)(2-q)^3 & 1 \le q < 2 \\ 0 & q > 2 \end{cases} \qquad (4.32)$$

where α_d, is equal to $1/h$, $15/7\pi h^2$, and $3/2\pi h^3$ in one-, two-, and three-dimensional respectively. In Figure 4.8 the Cubic kernel and its derivative are graphed.
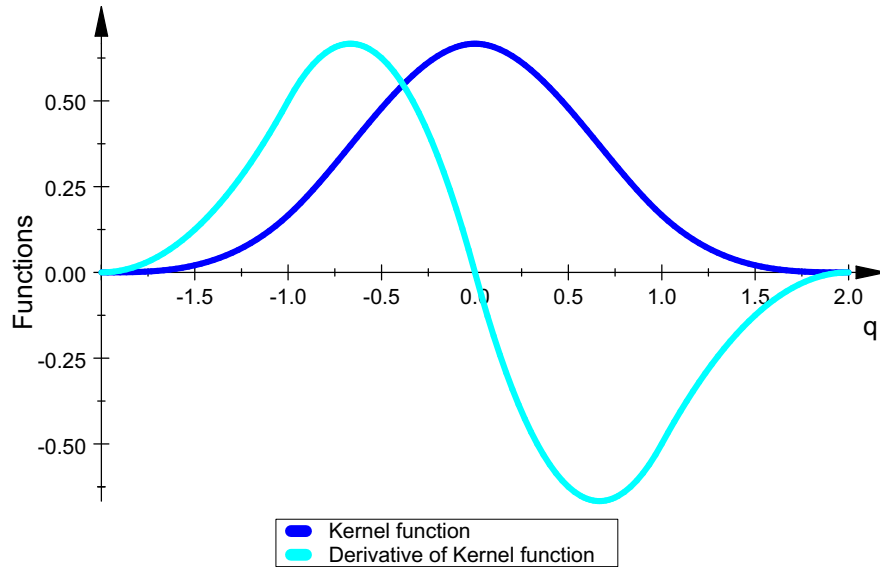
Figure 4.8: Cubic Kernel

(a)

(b)

(c)

(d)
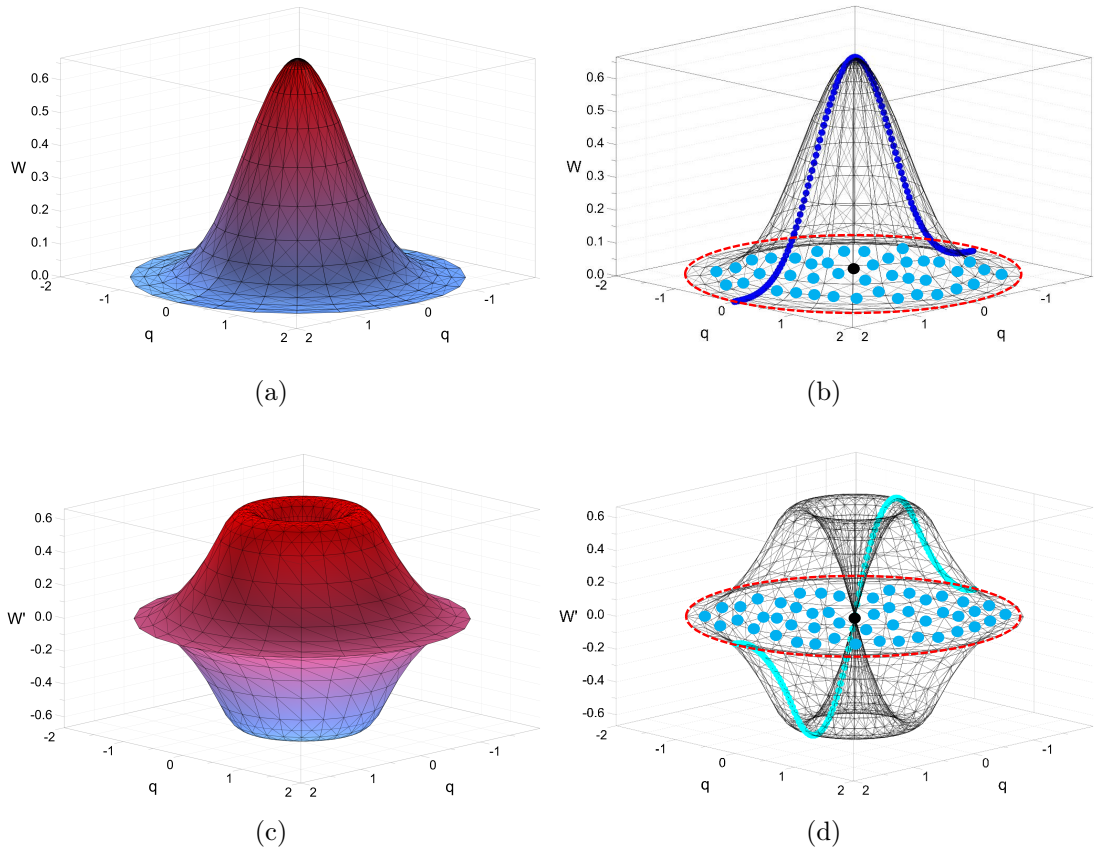
Figure 4.9: Cubic Kernel and its first derivative during a 2D calculation.

Figures 4.9(a) and 4.9(d), show the surface representation of the Cubic kernel, furthermore Figures 4.9(b) and 4.9(d), present in a more suitable form, the main idea of a particle interaction inside the compact support domain of the kernel and its derivative respectively.

Wendland Kernel

As presented in Wendland (1995), a new class of positive definite and compactly supported function was devised. The expression that defines this sort of kernel is the next:

$$W(r_i - r_j, h) = \alpha_d \Big(1 - \frac{q}{2}\Big)^4 (2q + 1) \quad 0 \leq q \leq 2 \tag{4.33}$$

where α_d, is equal to $7/4\pi h^2$, and $21/16\pi h^3$ in two-, and three- dimensional respectively. Figure 4.10 presents the graph of the Wendland kernel so its derivative.
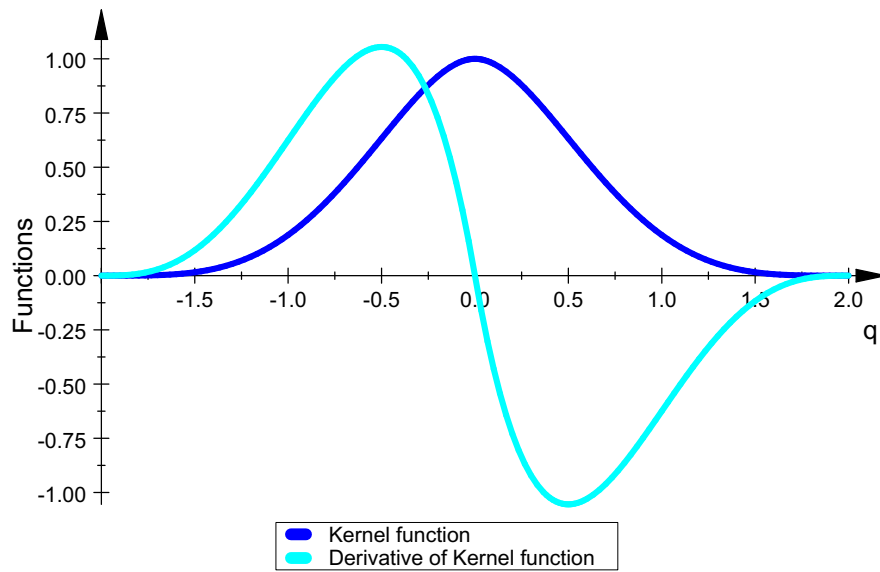
Figure 4.10: Wendland Kernel
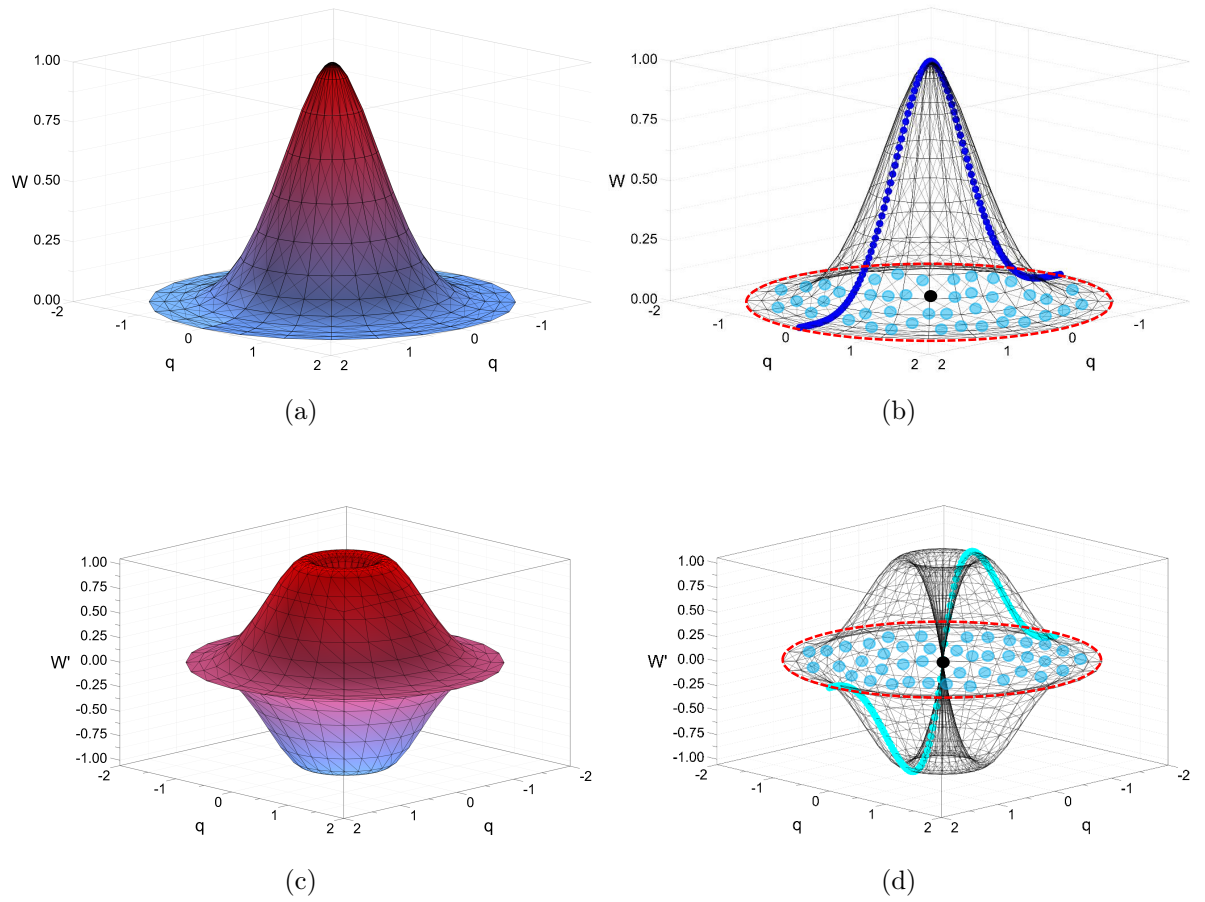
Figure 4.11: Wendland Kernel and its first derivative representation during a 2D calculation.

Figures 4.11(a) and 4.11(c), show the surface representation of the Wendland kernel, additionally Figures 4.11(b) and 4.11(d), present in a more suitable form, the main idea of a particle interaction inside the compact support domain of the kernel and its derivative respectively.

Before continuing with the selection of the smoothing function, there are some applications, and restrictions of the anterior kernels that seem to be appropriated to mention. Commencing with the Quartic kernel, it can be easily observed that the dimension of its compact support domain is smaller from the other functions, causing during the kernel approximation to not to consider enough number of neighbours, not to mention that its shape is far from the goal subject Gaussian-like shape that, is necessary to mimic according to (Monaghan, 1992). Continuing with the Gaussian kernel it is stated in (Liu and Liu, 2003) that, although it is deemed to have a sufficient smoothness for the differentiation process at higher derivative orders, it does not represent a real compact support domain, unless the smoothing length tends to zero in the infinite, nevertheless an advantage of this non real compact support is that, it is very stable and accurate when treating with disordered particles. Now, in the case of the Cubic smoothing function devised by (Monaghan and Lattanzio, 1985), not only a better smoothing dimension is defined, but also a more suitable Gaussian-like shape is obtained. Unfortunately as it is mentioned in (Monaghan, 1992), this function is piecewise defined, therefore the little difficulty of its implementation becomes an extra task to deal with, compared to the employment of one piece smoothing functions. Finally the Wendland kernel seems to mimic accurately the Gaussian shape, and at the same time to overcome the issues related to the piecewise cubic kernel function. Indeed such a smoothing function has gained in recent years an increasing interest in SPH applications. Figure 4.12, shows a comparison between smoothing functions.
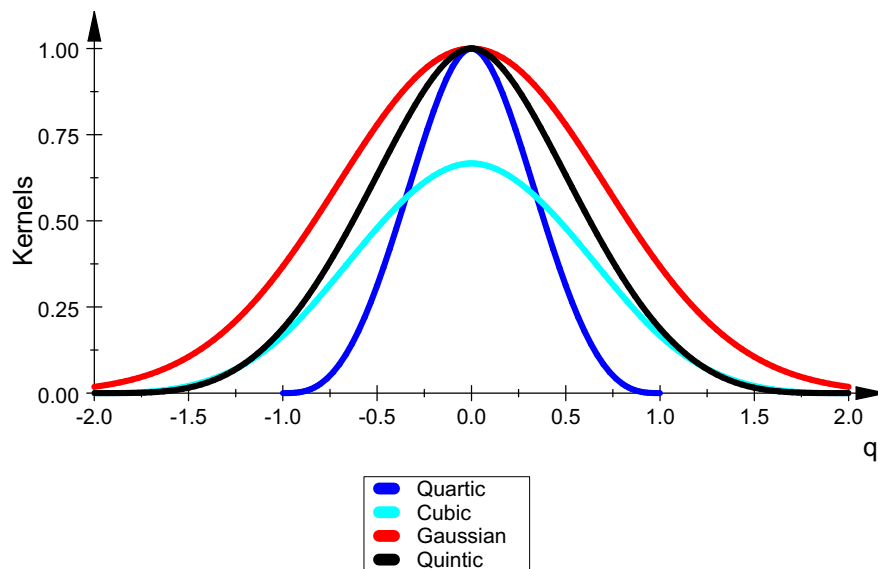
Figure 4.12: Kernels.

Observing the anterior in more detail, the kernel that mimics almost completely the Gaussian function shape is that devised from Wendland. Within the framework of this criterion the anterior comparisons suggest that a Wendland kernel is an excellent choice to be considered during the methodology execution. Figure 4.13 exhibits the kernel derivatives, demonstrating again that, the similarity between the Gaussian and Wendland functions is remarkable contrary to other kernels.
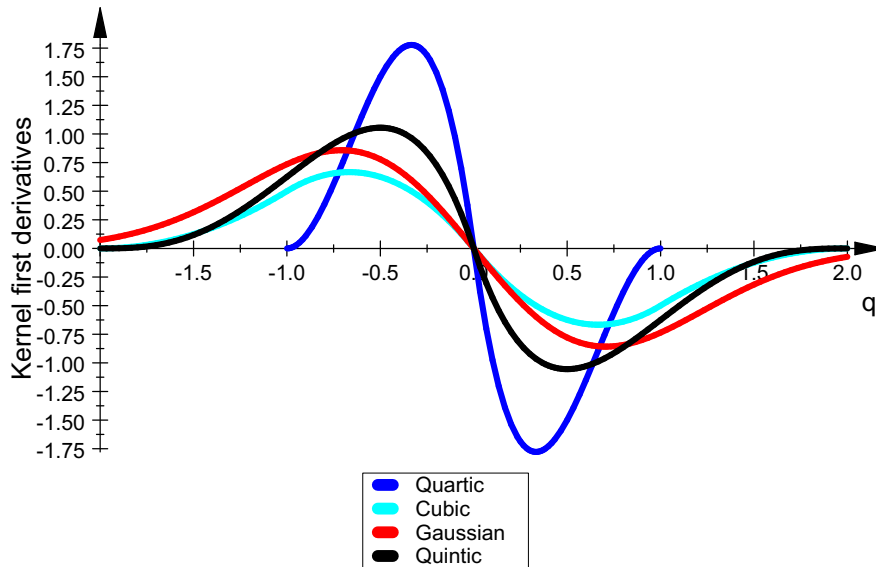
Figure 4.13: Kernel derivatives.

5
Numerical discretization

For the equations of mass and momentum conservation, a similar process like that shown in 4.2 at the beginning of chapter 4, is used.

Beginning with the continuity equation from chapter 3,

$$\frac{d\rho}{dt} = -\rho \nabla \cdot \boldsymbol{v}, \tag{5.1}$$

using eq.(4.24), and isolating the first term of the right hand side,

$$\begin{aligned}
\frac{d\rho(r_i)}{dt} =& -\rho(r_i)\nabla \cdot \boldsymbol{v}(r_i), \\
=& \boldsymbol{v}(r_i) \cdot (\nabla \rho(r_i)) - \nabla \cdot (\rho(r_i)\boldsymbol{v}(r_i)), \tag{5.2}
\end{aligned}$$

applying eq.(4.18) to the second term, and using the SPH gradient form obtained in Appendix B,

$$\begin{aligned}
\boldsymbol{v}(r_i) \cdot (\nabla \rho(r_i)) - \nabla \cdot (\rho(r_i)\boldsymbol{v}(r_i)) =& \boldsymbol{v}(r_i) \cdot \Big[\sum_j^N m(r_j)\nabla_i W(r_i - r_j, h)\Big] - \\
& \Big[\sum_j^N \frac{\rho(r_j)\boldsymbol{v}(r_j)}{\rho(r_j)} \cdot \nabla_i W(r_i - r_j, h)m(r_j)\Big], \\
=& \Big[\sum_j^N m(r_j)\big(\boldsymbol{v}(r_i) - \boldsymbol{v}(r_j)\big)\Big] \cdot \nabla_i W(r_i - r_j, h),
\end{aligned}$$

therefore, the particle approximation of the continuity equation results,

$$\frac{d\rho}{dt} = \Big[\sum_j^N m(r_j)\big(\boldsymbol{v}(r_i) - \boldsymbol{v}(r_j)\big)\Big] \cdot \nabla_i W(r_i - r_j, h). \tag{5.3}$$

which is the most common expression for the continuity equation in the SPH methodology. It is worth mentioning that this equation permits the density field to vary because the divergence does not equals to zero but only approaches; this means that eq.(5.3) admits density changes representing a compressible medium. Permitting non-zero compressibility the current discretization is titled Weakly Compressible Smooth Particle Hydrodynamics (hereafter referred as WCSPH).

For the momentum equation, from chapter 3,

$$\frac{d\boldsymbol{v}}{dt} = -\frac{1}{\rho}\nabla P + \frac{1}{\rho}\left(\nabla \cdot \rho\nu_o\nabla\right)\boldsymbol{v} + \boldsymbol{g} \tag{5.4}$$

Following a similar discretization process like in Appendix A for the Pressure term, it yields to,

$$\frac{\nabla P(r_i)}{\rho(r_i)} = \sum_j m_j \left(\frac{P(r_j)}{\rho(r_j)^2} + \frac{P(r_i)}{\rho(r_i)^2}\right) \cdot \nabla_i W(r_i - r_j, h). \tag{5.5}$$

this equality early used in (Liu and Liu, 2003; Monaghan, 1985, 1992), conserves both linear and angular momentum due to the existence of the action reaction principle between particles. As a consequence this SPH version of the Pressure term is considered a symmetrized and balanced approach. In the next section some of the treatments for the diffusive term in momentum equation is explained.

5.1 Viscosity treatment

Concerning the diffusive term in eq.(5.4) there exit at least three approaches. The first of these was presented by (Monaghan and Gingold, 1983) to allow shocks in tubes to be simulated. This numerical representation of the viscous term provides the advantage of diminish instabilities caused by the non uniform behaviour of the particles. The new viscous term is added commonly into the Pressure gradient in the momentum equation, resulting as it is shown below,

$$\frac{\nabla P(r_i)}{\rho(r_i)} = \sum_j m(r_j)\left(\frac{P(r_j)}{\rho(r_j)^2} + \frac{P(r_i)}{\rho(r_i)^2} + \Pi_{ij}\right) \cdot \nabla_i W(r_i - r_j, h). \tag{5.6}$$

where,

$$\Pi_{ij} = \begin{cases} \dfrac{\alpha\overline{c_{ij}}\mu_{ij}}{\overline{\rho_{ij}}} & \boldsymbol{v}_{ij} \cdot \boldsymbol{r}_{ij} < 0 \\ 0 & \boldsymbol{v}_{ij} \cdot \boldsymbol{r}_{ij} \geqslant 0 \end{cases} \tag{5.7}$$

with $\boldsymbol{v}_{ij} = \boldsymbol{v}_i - \boldsymbol{v}_j$, $\boldsymbol{r}_{ij} = \boldsymbol{r}_i - \boldsymbol{r}_j$, $\mu_{ij} = h\boldsymbol{v}_{ij} \cdot \boldsymbol{r}_{ij}/r_{ij} + \eta^2$, and $\overline{c_{ij}} = c(r_i) + c(r_j)/2$, that represents the mean speed of sound. The number $\eta^2 = 0.01h^2$ is factor inserted to prevent numerical divergences when two particles approach each

other, and α is a coefficient that depends on the particle distance, therefore it needs to be tuned depending on the study case so as to provide a proper dissipation (Crespo et al., 2015). In this manner (5.4) becomes,

$$\frac{d\boldsymbol{v}}{dt} = -\sum_j m(r_j) \left(\frac{P(r_j)}{\rho(r_j)^2} + \frac{P(r_i)}{\rho(r_i)^2} + \Pi_{ij} \right) \cdot \nabla_i W(r_i - r_j, h) + \boldsymbol{g} \qquad (5.8)$$

The second model proposed to approach the viscous term was presented by (Morris et al., 1997),

$$\Pi_i = \sum_j^N m(r_j) \frac{4\nu_o \boldsymbol{r}_{ij} \cdot \nabla_i W(r_i - r_j, h)}{(\rho(r_i) + \rho(r_j))(r_i - r_j)^2}. \qquad (5.9)$$

this model can be adapted in order to not to diverge when two particles approach each other (Lo and Shao, 2002), yielding to,

$$\Pi_i = \sum_j^N m(r_j) \frac{4\nu_o \boldsymbol{r}_{ij} \cdot \nabla_i W(r_i - r_j, h)}{(\rho(r_i) + \rho(r_j))(r_{ji})^2 + \eta^2}. \qquad (5.10)$$

thus, the version of the momentum equation using this approach yields,

$$\frac{d\boldsymbol{v}}{dt} = -\sum_j m(r_j) \left(\frac{P(r_j)}{\rho(r_j)^2} + \frac{P(r_i)}{\rho(r_i)^2} \right) \cdot \nabla_i W(r_i - r_j, h) +$$

$$\sum_j^N m(r_j) \frac{4\nu_o \boldsymbol{r}_{ij} \cdot \nabla_i W(r_i - r_j, h)}{(\rho(r_i) + \rho(r_j))(r_i - r_j)^2 + \eta^2} + \boldsymbol{g}, \qquad (5.11)$$

Both versions of the momentum equation are principally used when the case of study involves a laminar regime. The third approach was published by (Dalrymple and Rogers, 2006). Such approach allows modelling a turbulence flow based on the concept of Sub-Particle Scale first presented by (Gotoh et al., 2004). In this thesis the first two approximations will be implemented.

To complete the system of equations an considering small variations of the density field an equation of state is adopted. The most common equation of state implemented in WCSPH methodology is that proposed by Tait (Batchelor, 2000) which is used to mimic barotropic fluids. The equation is described as follows,

$$P_i = \frac{\rho_0 C_s}{\gamma} \left[\left(\frac{\rho_0}{\rho_i} \right)^\gamma - 1 \right] \qquad (5.12)$$

where ρ_0 is a reference density, C_s represents the sound velocity at the reference density, γ acquires the value of 7 for fluids like water.

5.2 Density treatment

The Lagrangian nature of the method carries a disordering in the particle domain, consequently high-frequency low amplitude oscillations populates the scalar field(Molteni and Colagrossi, 2009). These authors proposed to mitigate the consequences of the natural disorder of particles trough the addition of a diffusive term[1] into the continuity equation (5.3) as shown below,

$$
\frac{d\rho}{dt} = \Big[\sum_j^N m(r_j)\big(\boldsymbol{v}(r_i) - \boldsymbol{v}(r_j)\big)\Big] \cdot \nabla_i W(r_i - r_j, h) +
$$
$$
2\delta_\phi h c_0 \sum_j^N (\rho_j - \rho_i)\frac{(\boldsymbol{r}_i - \boldsymbol{r}_j)\cdot \nabla_i W(r_i - r_j, h)}{\boldsymbol{r}_{ij}^2}\frac{m_j}{\rho_j}. \tag{5.13}
$$

The anterior equality represents the formulation introduced by (Molteni and Colagrossi, 2009), commonly referred as δ-SPH formulation because of the free parameter δ_ϕ that is set to a suitable value. Formally it can be explained as the addition of the Laplacian of the density field to the continuity equation. Typically the value of the δ_ϕ parameter is 0.01.

5.3 Fluid solid interaction

Fluid solid interaction in SPH has been successfully modelled (Canelas, 2015), assuming that any given body with an arbitrary shape will behave like a rigid body. Therefore equations that govern the dynamics of the rigid body will predict the resultant motion of a body under the influence of a fluid flow. From a inertial reference frame, the equations that describe the rigid body dynamics are:

$$
M_I \frac{d\boldsymbol{V}_I}{dt} = \sum_i \boldsymbol{F}_i, \tag{5.14}
$$

$$
\boldsymbol{I}\frac{d\boldsymbol{\Omega}_I}{dt} = \sum_i (\boldsymbol{r}_i - \boldsymbol{R}_I) \times \boldsymbol{F}_i, \tag{5.15}
$$

where M_I is the mass of the body I, $\boldsymbol{V}_I$ its velocity, $\boldsymbol{I}_I$ its inertial tensor, $\boldsymbol{\Omega}_I$, its angular velocity, and $\boldsymbol{R}_I$ its center of mass, subjected to an arbitrary number of fluid particle forces $\boldsymbol{F}_i$ exerted at boundary particles referenced by $\boldsymbol{r}_i$. Both equations stand for the 6 degrees of freedom of the body that describe completely its dynamics.

Forces $\boldsymbol{F}_i$ that contribute to the motion of the rigid body are determined by the total summation of the fluid particle forces exerted on each body particle. The number of fluid particles that affects a particle on the body depends on

---

[1] In (Antuono et al., 2012) the analysis of the influence of this term is deeply discussed

the smoothing length of the kernel function. Thus, each boundary particle pertaining to the body experiences a force (Crespo et al., 2015) per unit mass expressed by,

$$F_i = \sum_w F_{iw}, \quad \text{with w} \in \{\text{Fluid-particles inside the kernel}\} \quad (5.16)$$

where F_{iw} represents the force per unit mass that a particle of fluid exerts on a body particle i. According to (Canelas, 2015), by using a particulate method it is easy to handle sub sets of particles (the body I), whose variables are integrated in time with a different set of equations. Therefore, using the resultant force from momentum equation of Navier Stokes and Newton's equations for rigid body dynamics, eq.(5.14) and (5.15) can be now expressed as,

$$M_I \frac{dV_I}{dt} = \sum_i m_i \frac{dv_{iw}}{dt}, \quad (5.17)$$

$$I \frac{d\Omega_I}{dt} = \sum_i m_i (r_i - R_I) \times \frac{dv_{iw}}{dt}, \quad (5.18)$$

in both equations $m_i \dfrac{dv_{iw}}{dt}$ involves the force exerted upon a particle that pertains to the set of particles of body I. This force incorporates body forces, and fluid particle resultant forces (from Navier Stokes momentum equation). Finally the resultant motion of the body I is driven by the sum of individual particle motions that follows,

$$v_i = V + \Omega \times (r_i - R_I). \quad (5.19)$$

The principal idea of the aforementioned is related to the previous work of (Koshizuka et al., 1998) and applied successfully by (Canelas, 2015).

5.4 Boundary treatment

Dynamic boundary conditions

In this kind of boundary treatment particles belonging to the boundary domain are considered to behave like fluid particles. Under this proposal particles representing any boundary shall satisfy both, continuity (5.3) and momentum (5.11) equations. Nevertheless the boundary domain may appear either fixed or experience an imposed law of motion. In the present study, boundary particles are fixed while representing a fluid reservoir in which the numerical campaign is carried out and just in one case there will appear an imposed motion law. In (Crespo et al., 2007b) the foundation and properties of this boundary treatment can be found, additionally a numerical and experimental comparison is

presented. The author also clarifies the simplicity and advantages of the dynamic boundary implementation in SPH-based numerical approaches.

When implementing Dynamic boundary treatment fluid particles near or approaching a boundary are subjected to a repulsive force. This force is the result of increasing the density value of particles that belong to the boundary when the distance of any fluid particle approaching it is below two times the smoothing length. The repulsion effect to the fluid particle is presented in the momentum equation due to the pressure term.

Periodic open boundaries

Periodic open boundaries algorithm let particles near an open lateral boundary consider information of particles inside a periodic (complementary) support domain. The complementary support domain on the opposite side of an open boundary mimics a domain with no lateral boundaries in the region where such implementation is applied. Figure 5.1 shows the idea of considering periodic open boundaries.
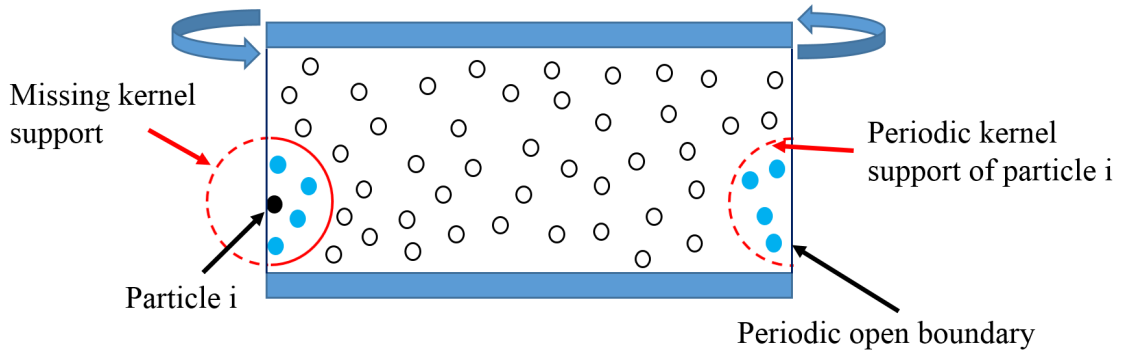
Figure 5.1: Periodic open boundaries.

5.5   Time integration

The integration in time in this study will adopt an explicit second order integration Symplectic scheme (Leimkuhler et al., 1996). Mainly the procedure involves two-half steps as it is explained below. Given the general term of material property S evaluated at particle i,

$$\frac{dS_i^{n+1}}{dt} = \frac{S_i^{n+1} - S_i^n}{\Delta t} \tag{5.20}$$

adding an adjustment to the anterior equation as follows,

$$\frac{dS_i^{n+1}}{dt} = \frac{S_i^{n+1} + S_i^{n+1/2} - S_i^{n+1/2} - S_i^n}{\Delta t} \tag{5.21}$$

then separating eq.(5.21),

$$\frac{1}{2}\frac{dS_i^n}{dt} = \frac{S_i^{n+1/2} - S_i^n}{\Delta t} \tag{5.22}$$

$$\frac{1}{2}\frac{dS_i^{n+1/2}}{dt} = \frac{S_i^{n+1} - S_i^{n+1/2}}{\Delta t} \tag{5.23}$$

rearranging terms in both equations,

$$S_i^{n+1/2} = S_i^n + \frac{1}{2}\Delta t\frac{dS_i^n}{dt} \tag{5.24}$$

$$S_i^{n+1} = S_i^{n+1/2} + \frac{1}{2}\Delta t\frac{dS_i^{n+1/2}}{dt} \tag{5.25}$$

commonly eq. (5.24), and (5.25) are referred as predictor and corrector steps.

Concerning the stability of the simulation the parameter that rules the region where the methodology does not present numerical disturbances while approaching an analytical solution is the Courant-Friedrichs-Lewy (CFL) condition. Furthermore this number allows the time length step appropriated for the information of a material function to travel through each discretizated spatial region. Therefore the information behaves in a more realistic manner. Based on the DualSPHysics software implementation the CFL number is calculated as follows.

$$\Delta t = CFL \cdot min\big(\Delta t_f, \Delta t_{CV}\big) \tag{5.26}$$

where,

$$\Delta t_f = min_a\left(\sqrt{\frac{h}{|\boldsymbol{f}_a|}}\right)$$

$$\Delta t_{CV} = min_a\left(\frac{h}{c_s + max_a\left|\dfrac{h\boldsymbol{v}_{ij}\cdot\boldsymbol{r}_{ij}}{\boldsymbol{r}_{ij}^2 + \eta^2}\right|}\right)$$

High Performance Computing implementation

Due to the necessity of extending numerical calculations to parallel architectures so as to reach admissible computational times, extraordinary efforts have been recently developed in the usage of Graphic Processing Units best known as GPU's. Linked to this a high demand on adapting serial codes to clusters arrays may appear to increase. As a consequence many of the actual softwares let the user perform simulations using more than just one core in a desktop machine. This is the case speaking particularly about the DualSPHysics software. The nature of the SPH methodology let the code be massively parallelized, since each material particle can be easily tracked and be treated as

an individual entity. DualSPHysics provides the option of carrying out numerical simulations in a GPU card implementing CUDA or in a cluster by means of the Message Passing Interface standard. In this study a comparison of two different parallel architectures will be exposed. A detailed explanation about the High Performance Computing implementation in DualSPHysics can be found in (Cercos-Pita, 2015; Crespo et al., 2015; Domínguez et al., 2013a,b; Maruzewski et al., 2010; Moulinec et al., 2008; Valdez-Balderas et al., 2013).

6

Results and validations

In this chapter the numerical results of implementing the Smoothed Particle Hydrodynamics methodology concerning the solution of the Navier-Stokes equations are presented. The numerical approaches were carried out upon the assumption of a quasi-incompressible viscous fluid. Initially the SPH method is validated in accordance with other authors results. First the results of the classical cases of immersed simple geometries in a viscous fluid are conducted. In one of the cases the results of a moving square in accordance with an imposed motion law through a fluid at rest are exhibited. Similarly the case of a fixed circular cylinder immersed in a fluid flow is exposed and discussed. Furthermore the ascending motion of a circular cylinder located at a certain depth from an undisturbed free surface is examined; the ascending motion is a consequence of the density differences of the cylinder and the fluid. Similarly the fluid flow through an open channel configuration, namely a fish-pass structure, is investigated. The aforementioned study cases assess the performance of the numerical methodology letting SPH be able to obtain results in close agreement with previous solutions either numerical or experimental from other authors work. Finally two interesting cases are discussed. First the a numerical simulation of the submarine ascending motion to an undisturbed free surface in an open channel is described. Following a similar procedure like that in the ascending motion of the cylinder, a difference of densities between the solid body and the media causes the buoyantly rising to the free surface. To conclude a numerical approach of a train when it passes trough a tunnel is studied.

Flow around a moving square cylinder

Continuing with the process of conducting a numerical simulation, after having described the physical phenomenon in chapter 2, a pre-processing stage is then performed, namely the particle representation of the continuous domain as shown below.
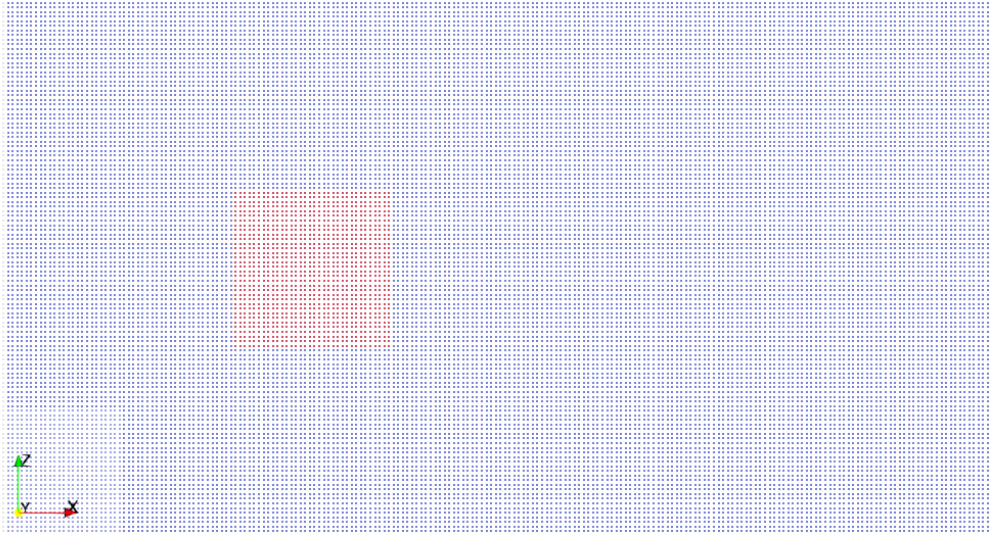
**Figure 6.1:** Initial particle representation.

Figure 6.1 shows the square (particles coloured by red) and fluid (particles coloured by blue) domains in their particle representation. The square cylinder has been discretised into boundary particles, such particles have the same properties of fluid particles but they remain linked during the travelling (see motion law in Figure 2.2) along the x axis through the fluid. The entire domain is not plotted in order to appreciate the subdivision in particles of the geometry of interest.

The drag coefficient C_d is calculated according to (Colagrossi, 2011),

$$C_D = \frac{|F_x|}{\frac{1}{2}\rho U^2 L} \tag{6.1}$$

where F_x stands for the total force vector x-component exerted by the fluid to the square. Important parameters like the diffusion coefficient δ_ϕ (see eq.(5.13)) are set as 0.1 as suggested in (Crespo et al., 2015), only extreme oscillations may demand an increase in the coefficient value. A distance between particles of $dp = 0.03$ m is adopted, the smoothing length is calculated resulting in $h = 0.044$ m, and the CFL number is designated as 0.2. The number of particles "np" for representing the computational domain was np=4M and the Reynolds number obtained using the current physical parameters is Re=150.

Results and comparison of the SPH numerical approaching with other authors contributions are highlighted. The total drag force is plotted in Figure 6.2 and compared in Table 6.1 with previous solutions from (Bouscasse et al., 2013) and (Franke et al., 1990).
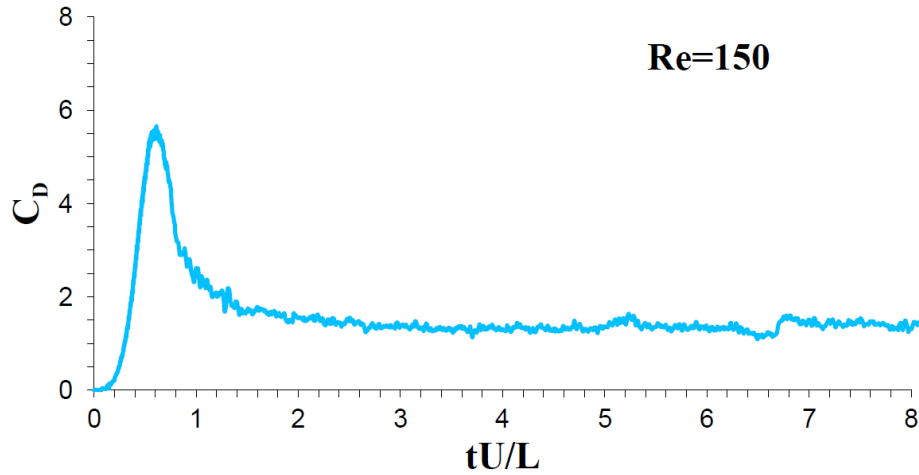
Figure 6.2: Total drag force coeficcient.

Author	C_D
(Franke et al., 1990)	1.5
(Bouscasse et al., 2013)	1.72
Present result using DualSPHysics	1.45

Table 6.1: Comparison of previous numerical solutions of a moving square cylinder at Re=150

Flow around a fixed circular cylinder

This section present the results of the second study case early described in chapter 2, for more details refer to Figure 2.3. Then conducting the particle representation like in the previous section, Figure 6.3 illustrates the final set of particles that represents the boundary (circular cylinder)and fluid domains. Again not the entire domain is presented in order to scheme the zones of interest, namely the circular cylinder. The Reynolds number calculated for this phenomenon is Re=100.
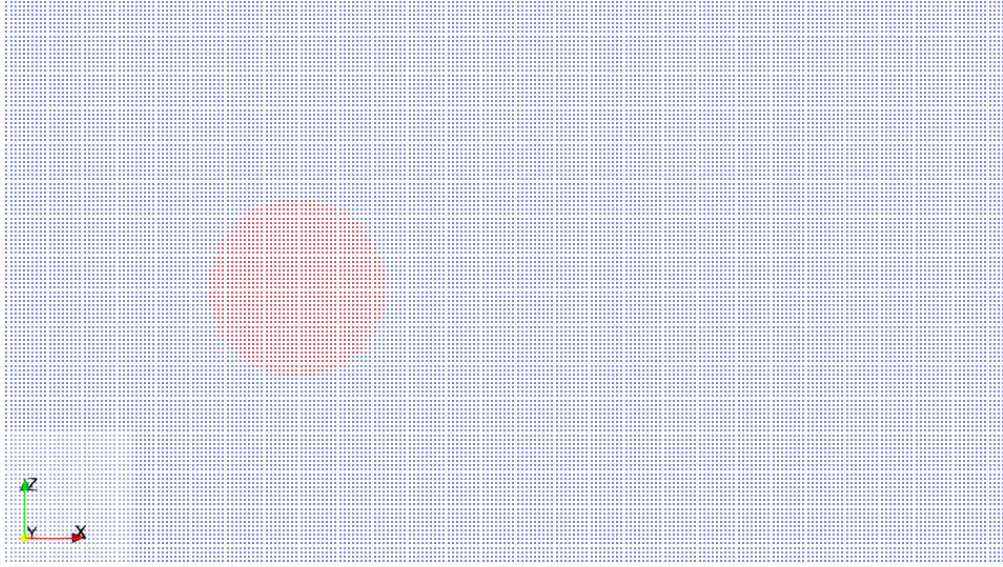
Figure 6.3: Initial particle representation.

Regarding the numerical approach it is considered $\delta_\phi = 0.1$, the distance between particles is dp= 0.03 m. Additionally the calculated smoothing length was $h = 0.025$ m, and the CFL number remains equal to 0.2. The total number of particles employed for the simulation was np=2M. In order to validate quantitatively the results obtained the lift and drag coefficients, and the Strouhal number are compared with other published contributions. The lift and drag coefficients are defined as follows,

$$C_L = \frac{|F_y|}{\dfrac{1}{2}\rho U^2 D} \tag{6.2}$$

In the case of the drag coefficient eq. (6.1) is adapted in the following manner,

$$C_D = \frac{|F_x|}{\dfrac{1}{2}\rho U^2 D} \tag{6.3}$$

where D is now the characteristic length. Both F_x and F_y represent the corresponding force components in x and y directions of the resultant force vector

applied to the cylinder by the fluid flow. The Strouhal number is defined as $St = D/TU$ being T the period of the regular vortex pattern generated "vortex shedding", U is the far-field velocity and D is the characteristic length. Table 6.2 outlines a comparison of previous works and the values measured in this study case.

Author	C_D	C_L	St
(Braza et al., 1986)	1.364	± 0.25	-
(Liu et al., 1998)	1.350	± 0.339	0.164
(Calhoun, 2002)	1.330	± 0.298	0.175
(Ng et al., 2009)	1.368	± 0.36	-
(Marrone et al., 2013)	1.36	± 0.24	0.168
(Vacondio et al., 2013)	1.33	± 0.33	0.16
Present results using DualSPHysics	1.32	± 0.25	0.18

Table 6.2: Comparison of previous solutions for C_D, C_L, and Strouhal number of fluid passing a circular cylinder.

Ascending motion of a cylinder in a viscous flow

This third study case previously detailed in chapter 2 (see Figure 2.4 for a brief description) is discretised into particles as shown in Figure 6.4. Due to the dimensions of the physical phenomenon a noteworthy difference is observed, namely the complete particle distribution of the entire numerical domain.
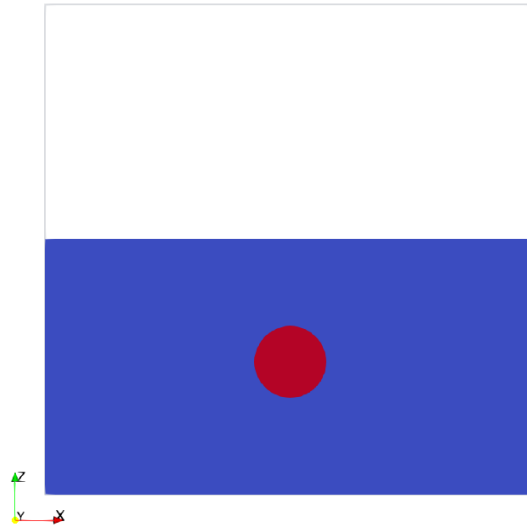
Figure 6.4: Initial particle layout.

Figure 6.5 illustrates a detailed view applied to the geometry particle distribution.
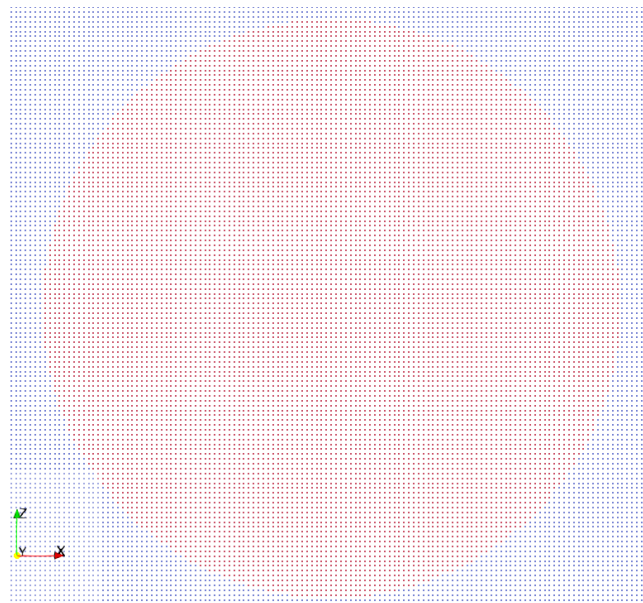
Figure 6.5: Detail of the circular cylinder.

The numerical parameters consist of $\delta_\phi = 0.1$, the distance between particles dp= 0.0025 m. Concerning the kernel attributes the smoothing length results $h = 0.0084$ m. Again CFL=0.2, and the number of particles np=335K.

Figure 6.6: Ascending motion of the cylinder exit from the free surface $\rho_c = 0.62\rho_w$ kg m^{-3}.

Figure 6.6 exhibits different positions during the vertical ascending motion of the cylinder until its exit from the fluid free surface.

(a) t=0.9s   (b) t=1.0s   (c) t=1.1s

(d) t=1.2s   (e) t=1.3s   (f) t=1.4s

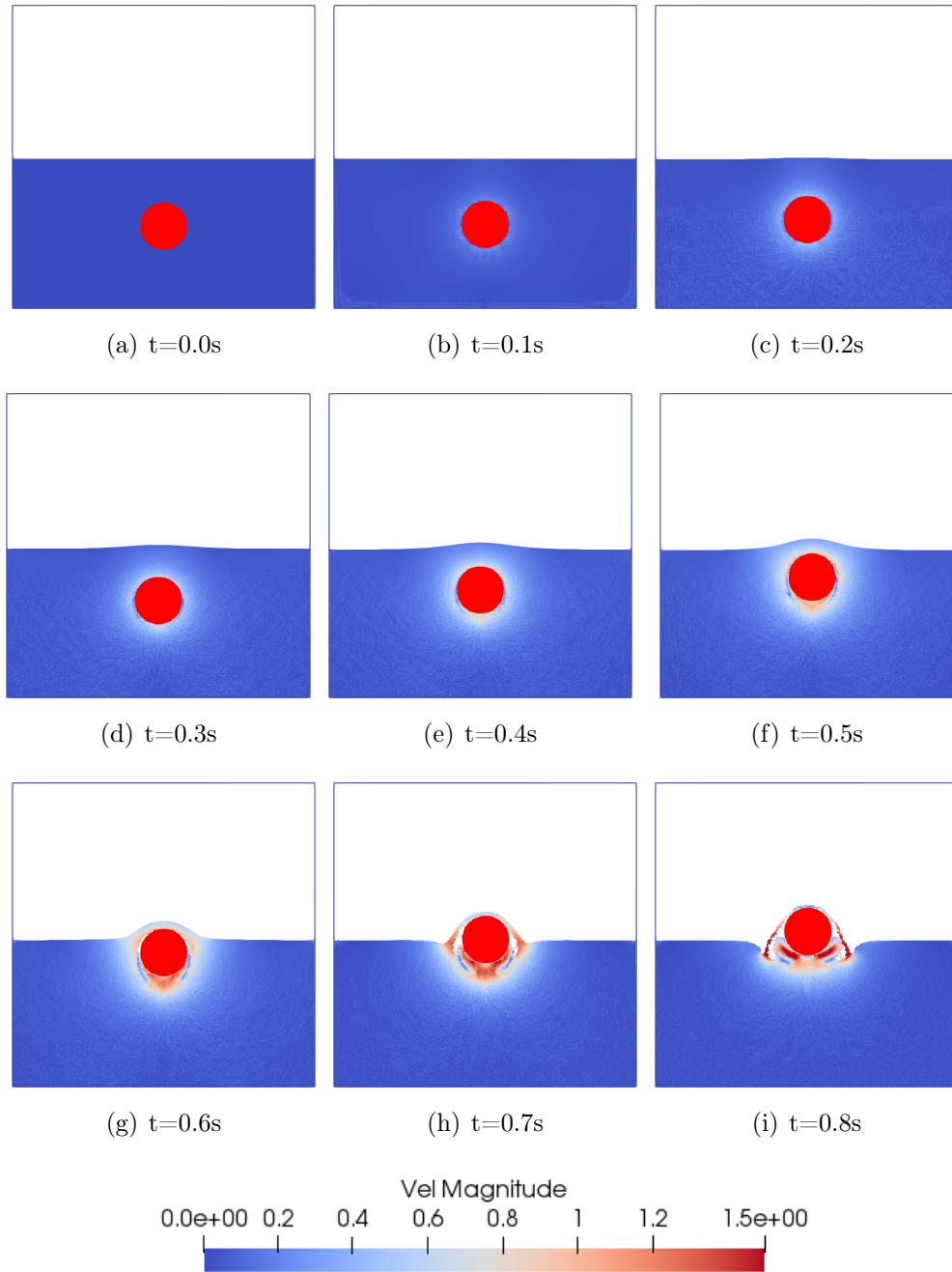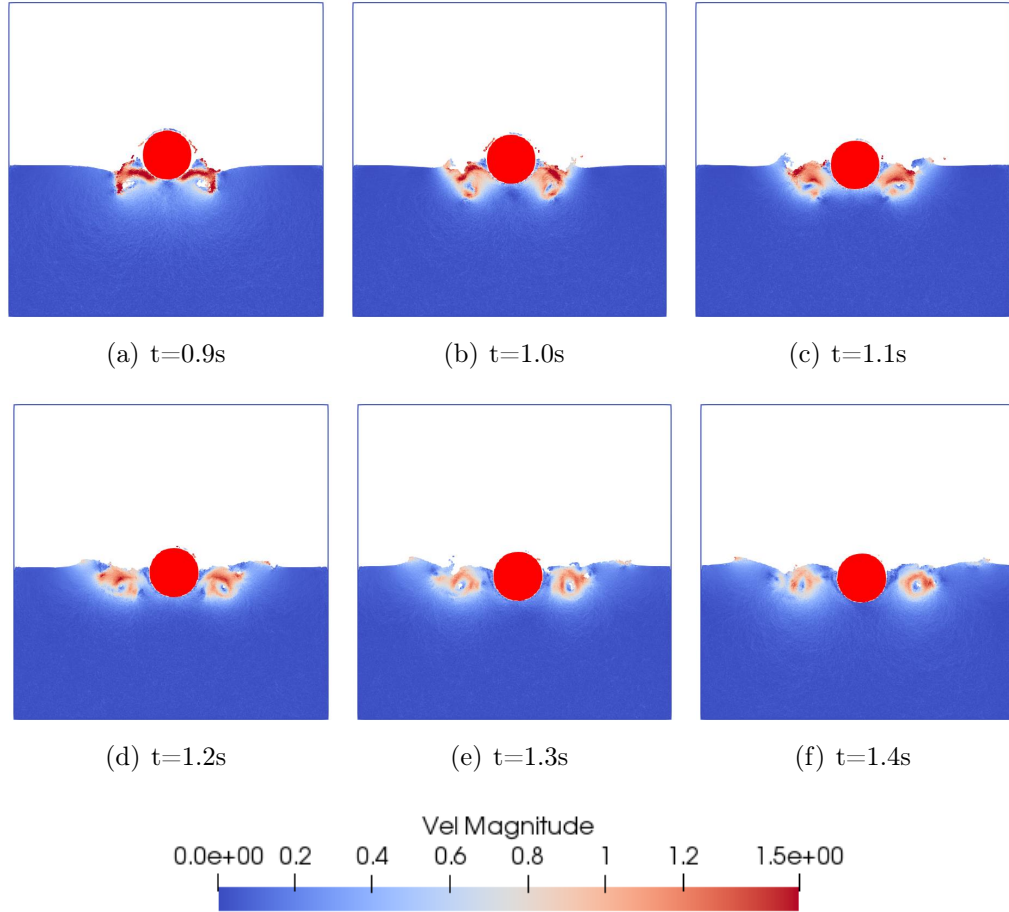**Figure 6.7:** Cylinder returning back motion.

Once the cylinder has reached its maximum position it presents a vertical descending motion and drops again into the fluid domain. Eventually the cylinder exhibits an oscillatory movement until the entire system reaches an equilibrium steady state, such phenomenon is not discussed in this study, since the main objective is the validation of the ascending motion. In Figure 6.7 locations at different time steps described by cylinder are depicted.

In order to assess quantitatively the numerical SPH capabilities, a comparison with previous results of (Moshari et al., 2014) is carried out. The values of maximum velocity and change in position along the vertical direction are then plotted. Figures 6.8 and 6.9 show the maximum values of the velocity achieved by the cylinder. Notwithstanding the slight discordance in the maximum velocity value, the numerical simulation using the SPH method compared well and exhibits a similar tendency like that in experimental results.

It is worth pointing that, in (Moshari et al., 2014) an air-liquid simulation was performed using VOF method with a special interface treatment. Therefore SPH seems to provide good results even when considering a single phase.
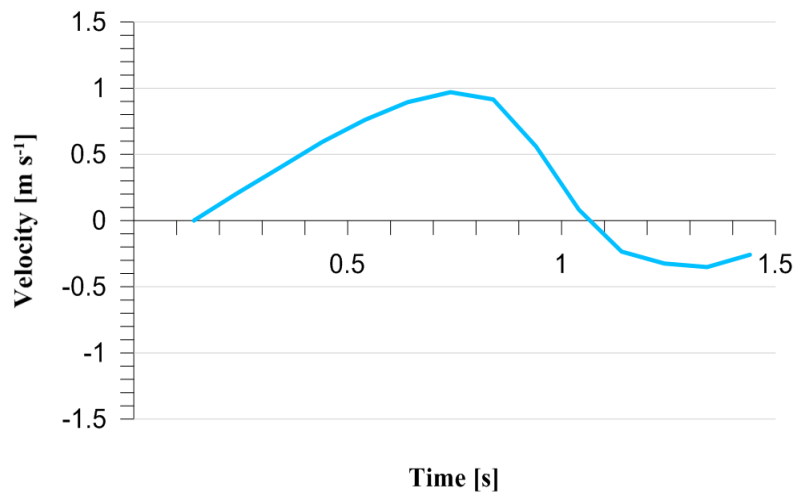
Figure 6.8: Present results using the SPH method.
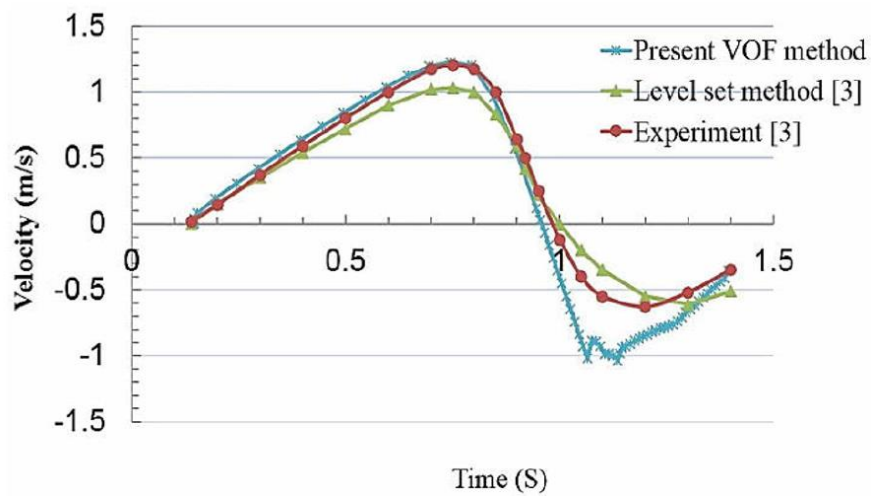
Figure 6.9: Velocity values from (Moshari et al., 2014).

65
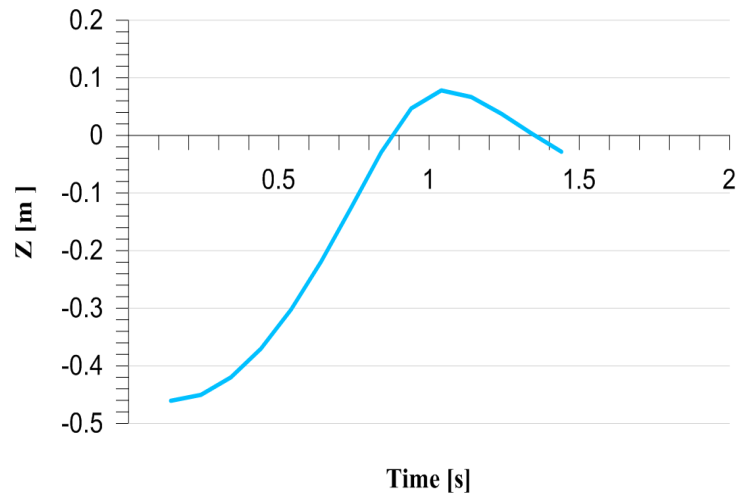
Figure 6.10: Present results using the SPH method.
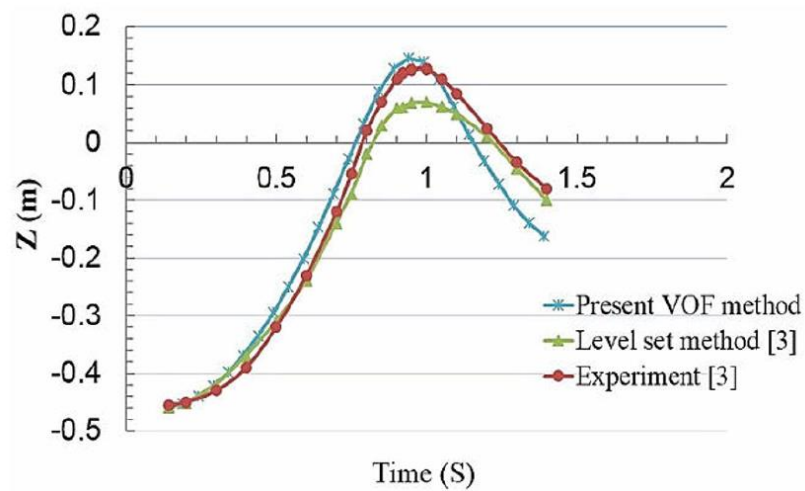
Figure 6.11: Distance of the center along the vertical axis till the free surface (Moshari et al., 2014).

Figures 6.10 and 6.11 plot the vertical ascending motion described by the cylinder. Finally Table 6.3 presents other authors solution and the final results acquired using SPH.

Author	Velocity $\mathrm{m\,s^{-1}}$	Height m
(Colicchio et al., 2009)	1.2	0.125
(Moshari et al., 2014)	1.22	0.14
Present results using DualSPHysics	0.97	0.08

Table 6.3: Comparison with previous solutions.

A single carriage train travelling through a tunnel
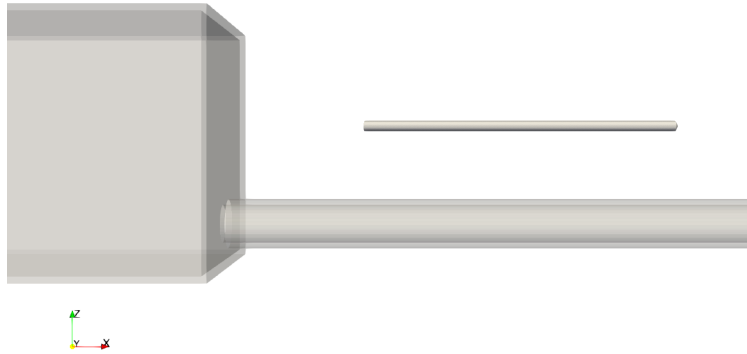
Figure 6.12: Original domain.
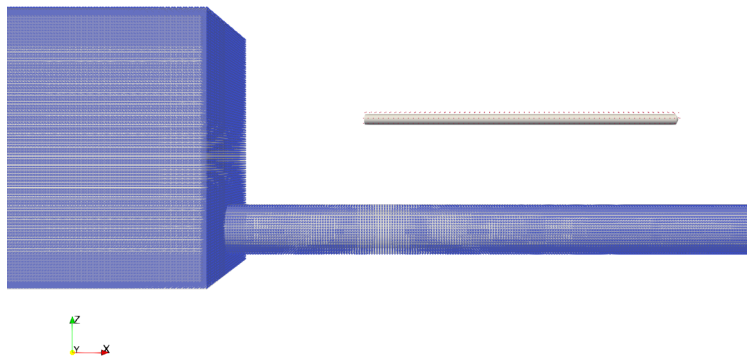
Figure 6.13: Particle distribution process.
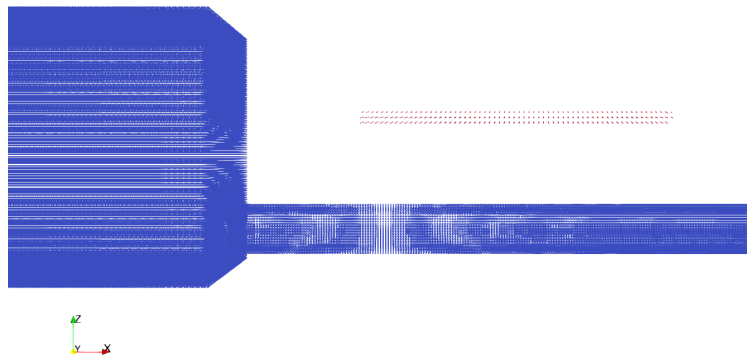
Figure 6.14: Final particle domain representation.

Figures 6.12, 6.13 and 6.14, describes the process of particle representation applied to the current numerical domain. This discretization process does not imply a complex topological relation between particles unlike mesh based methods. Only the process of particle representation is shown for solid boundaries in order to diminish confusion.

Results of the numerical simulation Figure 6.15 shows that compared to the solution obtained by (Ricco et al., 2007) shown in Figure 6.16 pressure values apparently exist in the same range.
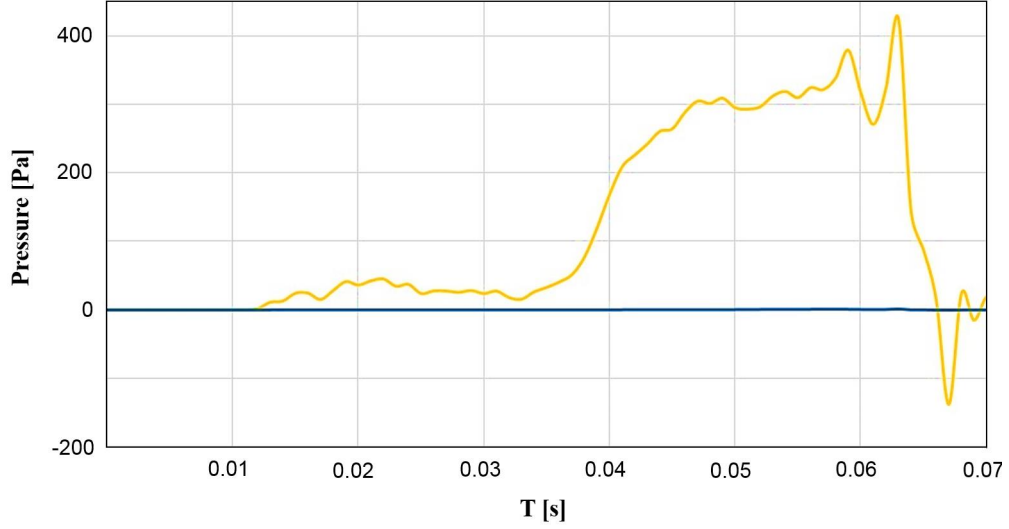
Figure 6.15: Pressure values during the train travelling along the tunnel. Solution using DualSPHysics.
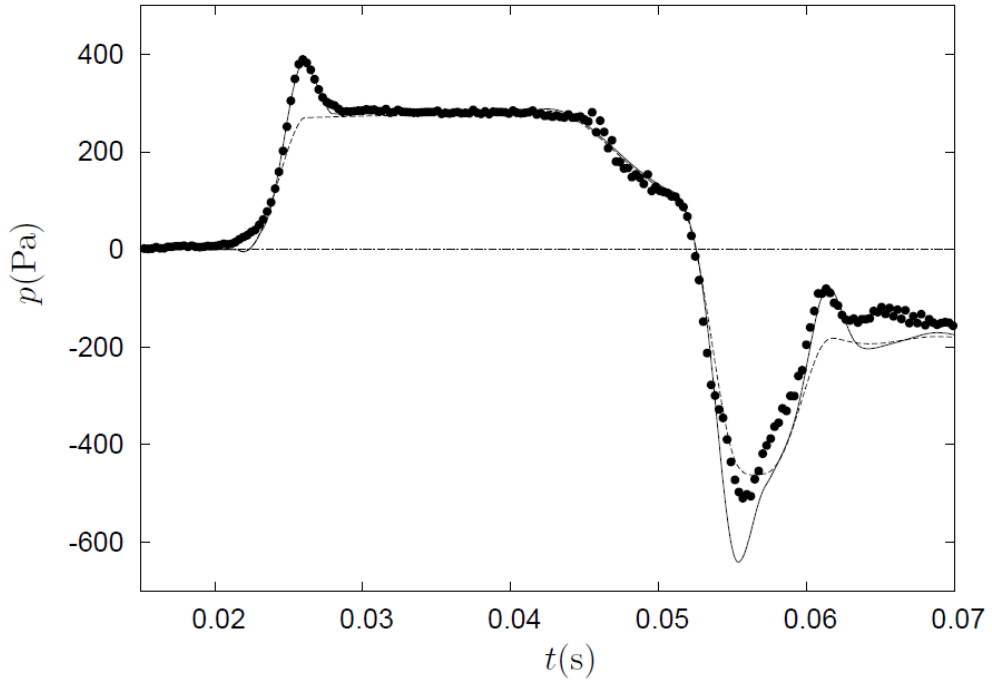
Figure 6.16: Pressure values during the train travelling along the tunnel, travelling at $v_x = 30.6$ m s^{-1}. Comparison between experimental ($\bullet$) and numerical data with (—) and without (– –) the separation bubble model. Results taken from (Ricco et al., 2007).

Such tendency shown in experimental results is found to be the typical pressure behaviour considering a single train travelling through a tunnel. In the present study a crucial difference starts at $t = 0.015$ s where the particle located to measure the pressure field (see Figure 2.8) begins to detect the presence of the train some seconds earlier than in the experimental facility. This earlier pressure detection confirms that special treatments should be employed, since the numerical domain is assumed to be confined. Additionally it seems that information of field variables do not travel through the media at the right velocity. This may suggest an increase in the sound velocity so as to achieve a correct pressure recording. Another interesting observable factor is that, DualSPHysics was unsuccessful to predict low pressure reported values. This is featured during the interval period of time $t = [0.06 - 0.07]$ s where the pressure values correspond to a minimum of P$= -145$ Pa which is higher compared with value achieved in the experiments P< -500 Pa.

Important factors considered during the pre-processing stage, are the extension added (see Figure 2.5) to the numerical domain. Differences in pressure measurements using different extensions in the numerical domain (not shown), do highlight the necessity of consider a bigger domain as previously mentioned so as to numerically approach more realistic solutions. Errors due to the reflected waves in the pressure field suggest that special boundary treatments are needed to be performed. DualSPHysics apparently reproduced the values obtained using the numerical code in (Ricco et al., 2007) when no separation bubble model is turned on. Nevertheless, quantitatively the results do not match with any of the models presented in previous works, where the behaviour seems be more like the solution published by (Ricco et al., 2007).

Finally the oscillatory behaviour of the pressure measurement reinforce the use of the $\delta\phi$ parameter. By increasing the value of such numerical aid, variations are expected to decrease. Unfortunately this study reveals the limitations of DualSPHysics at least for this sort of studies. The compressibility threshold required for matching experimental solutions when treating high speeds accurately, is beyond the capabilities of the code. An attempt to modify the code in order to add the equation of energy and modify the equation of state is pretended to be performed in the future to become success in challenging high speed problems.

Ascending motion of a submarine hull

This study case covers the submarine hull ascending motion. Figures 6.17 and 6.18 describe a similar process of converting any complex geometry into its particle distribution like that illustrated in the anterior section. For further details refer Figures 2.11 and 2.12 in chapter 2.

Figure 6.17: Original domain.
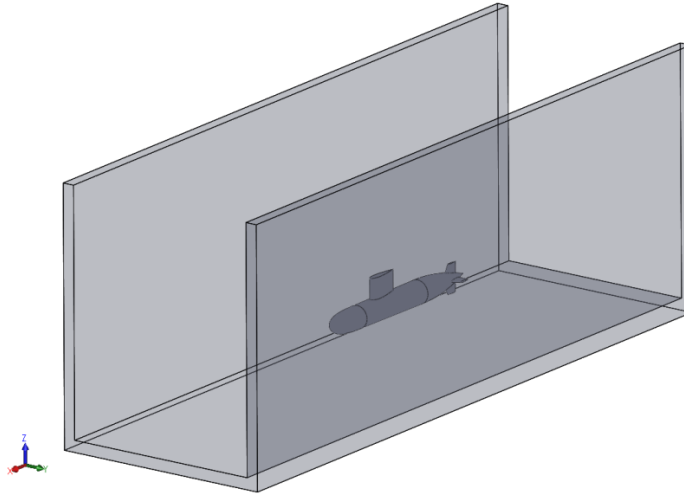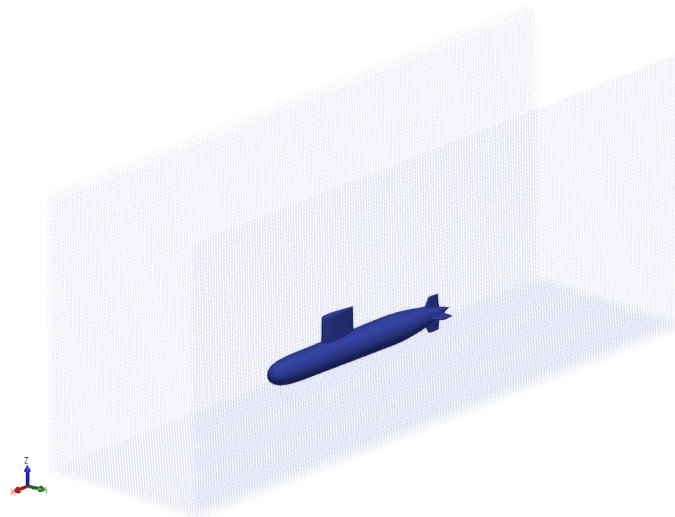

Figure 6.18: Particle distribution process.

Figure 6.19, illustrates a detailed view of the submarine hull. It can be appreciated the level of detail once the particle distribution has been performed. It is remarkable how the particles easily are able to reproduce the particle version of solid parts like the appendages, which are those structures at the rear (often called tail) part of the submarine. Also the sail (tower-like structure), at the top of the submarine has accurately been discretised into particles. Is important to note that, no pitfalls about the division into particles in any study case has been mentioned. This contributes to the ease of the SPH methodology and in particular DualSPHysics to manage geometries even simple or complex unlike traditional grid-based methods do.
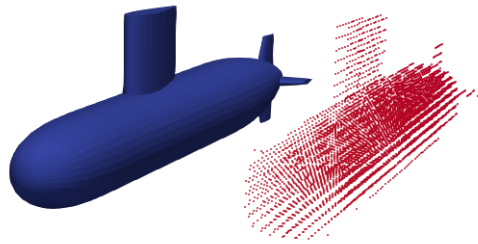
Figure 6.19: Final particle domain representation using Gencase.

Figure 6.20 exhibits the vertical position change described by the submarine hull during its ascending motion.
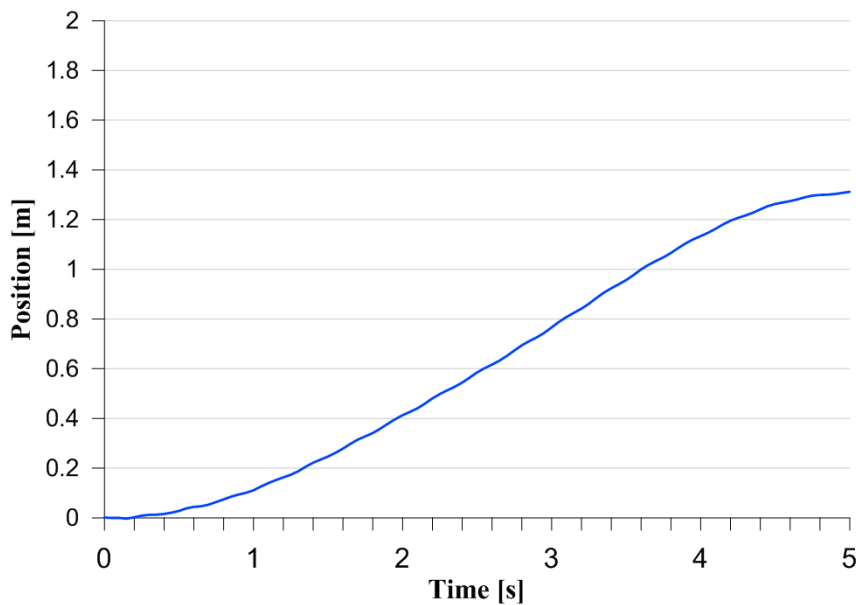
Figure 6.20: Position of the center of mass of the submarine during the surfacing.

Figure 6.21 illustrates the rotation in the x-component axis. This rotational motion reveals a instability in the axial axis of the submarine hull. This results confirm the previous findings (Bettle et al., 2009, 2014b) with the difference that, they implemented a mesh-grid based method.
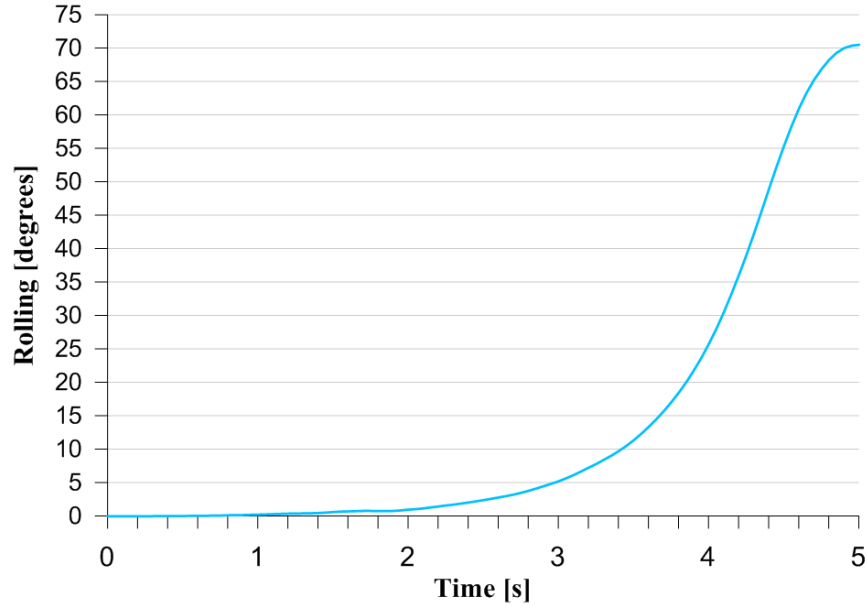
Figure 6.21: Final particle domain representation using Gencase.

As a consequence of the difference of densities between the body and the media, causes an increase in the velocity field, in particular in the z-component similarly to the case of the circular cylinder. However the contribution to the rotational motion is due to the asymmetric submarine shape. This geometrical issue let the vertical forces exerted in the body structure try to rotate the submarine. Additionally the area of the sail at the top of the body permits the forces to increase their effect by means of major area of application. Contributions of all forces even exerted by viscous or pressure terms cause a rotational motion of approximately 70 deg, in contrast to the pitching Figure 6.22 and yawing Figure 6.23 rotational motions. The resultant pitching developed with respect to the y-component shows a tendency which is attributed to the initial sudden acceleration. The sudden starting causes a difference in the current position of the mass center and consequently unstable forces, in particular the buoyant force will try to meet again an equilibrium. Until such equilibrium is recovered all non-equilibrated forces components cause a movement, being this movement higher where no equilibrium is encountered. Therefore it can be conclude that the higher non equilibrium state is that where no significant symmetry exist, in this case and viewing the submarine normal to the y axis, the former part (where the sail is) and the rear part (where an array of appendages appear).
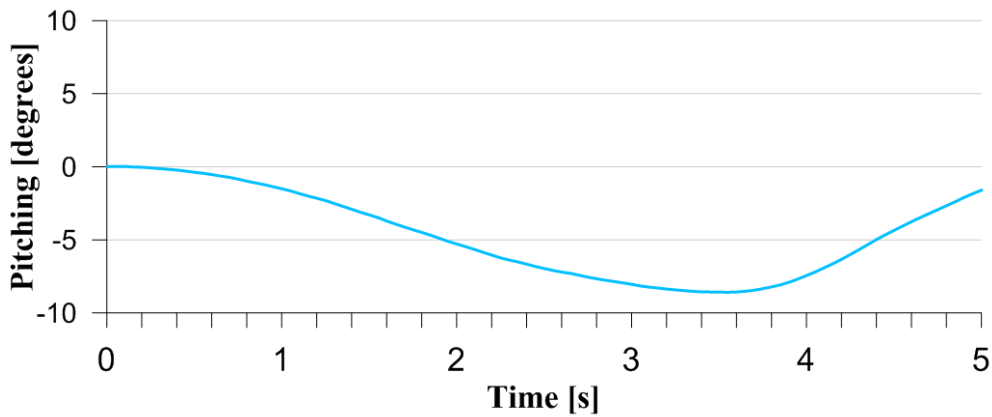
Figure 6.22: Final particle domain representation using Gencase.
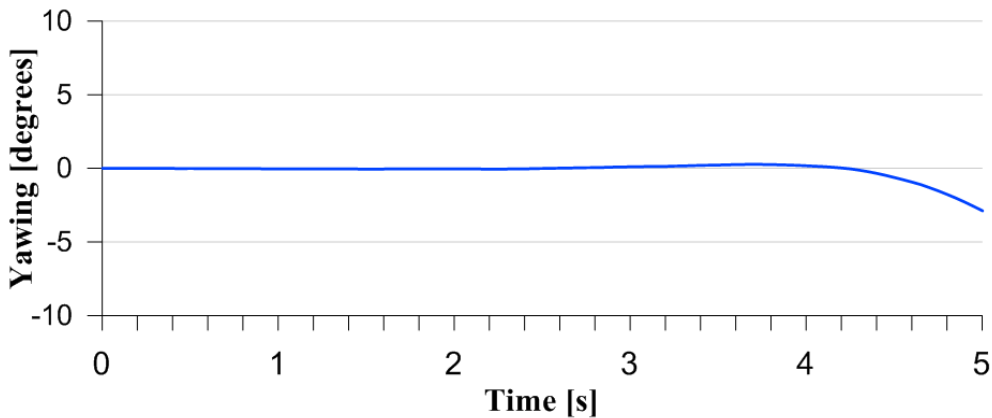
Figure 6.23: Final particle domain representation using Gencase.

Observing the yawing rotation it is quite obvious that, as the horizontal forces acting on the body are equal at equal levels of depth therefore no significant during the ascending motion as it is depicted in Figure 6.23. The following Figures illustrates each of the rotational motions in more detail during the ascending. Figure 6.24(c) shows that the pitching rotation explained in previous paragraphs starts being more evident at t=2.0s. The height of the water level does not provide sufficient time for the submarine to even achieve a terminal velocity, what causes en effect for a continuous non equilibrium state. This is maintained until the submarine exits from the free surface. An important point to mention is that, in all the next Figures just the particles in the free surface are depicted to not contribute to confusion.
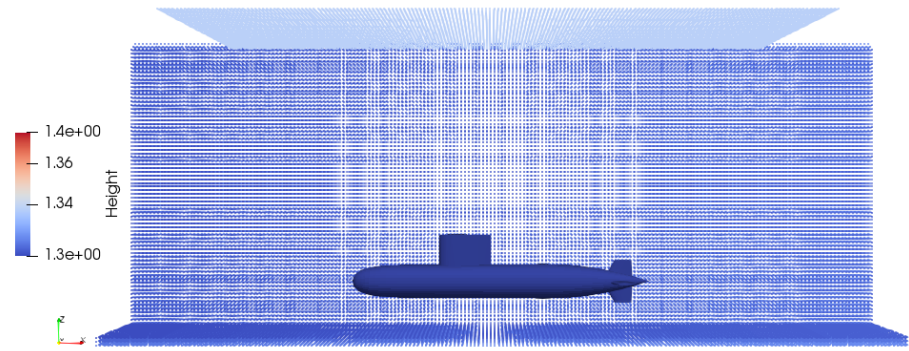
(a) t=0.0 s
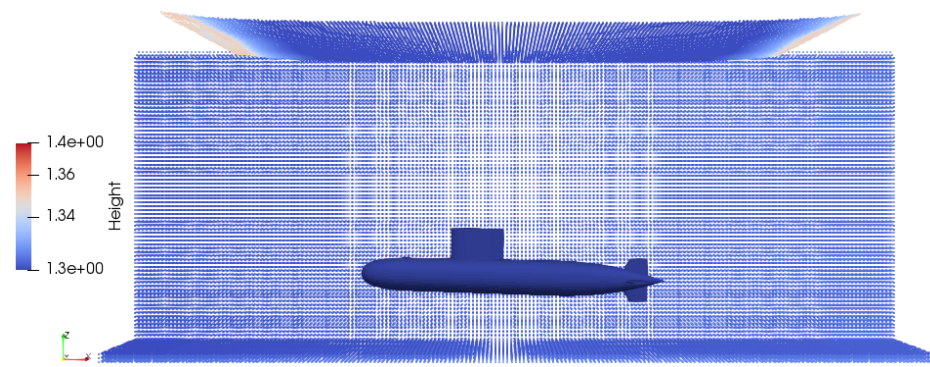
(b) t=1.0 s
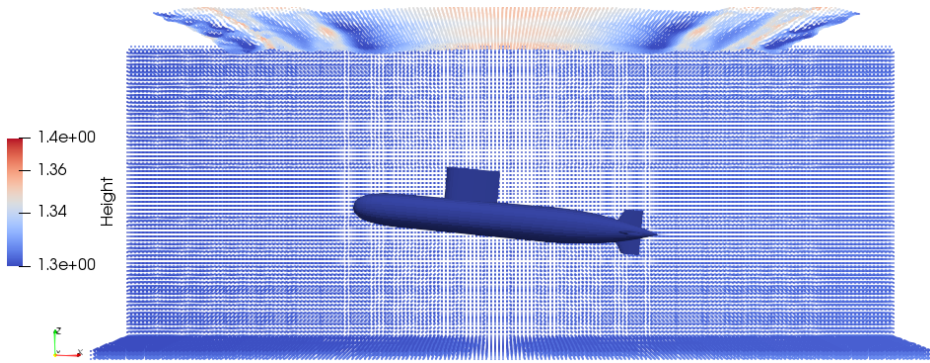
(c) t=2.0 s
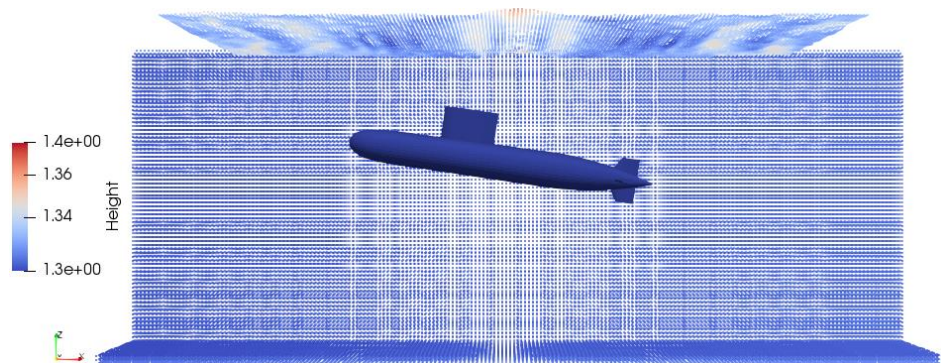
(d) t=3.0 s

Figure 6.24: Submarine pitching rotational motion.
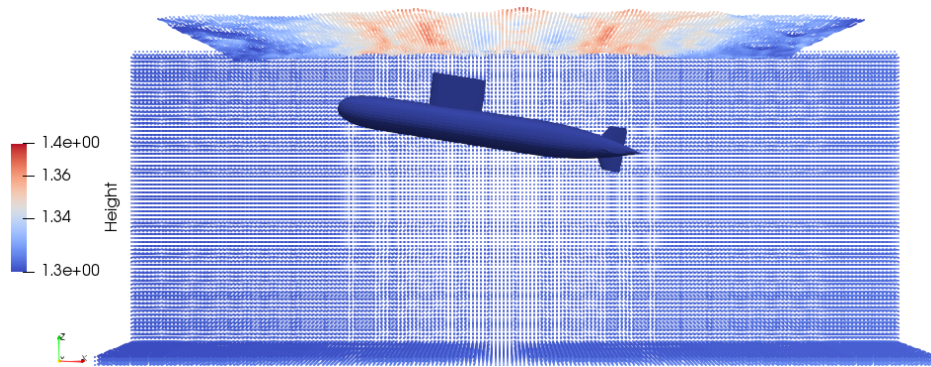
(a) t=3.5 s
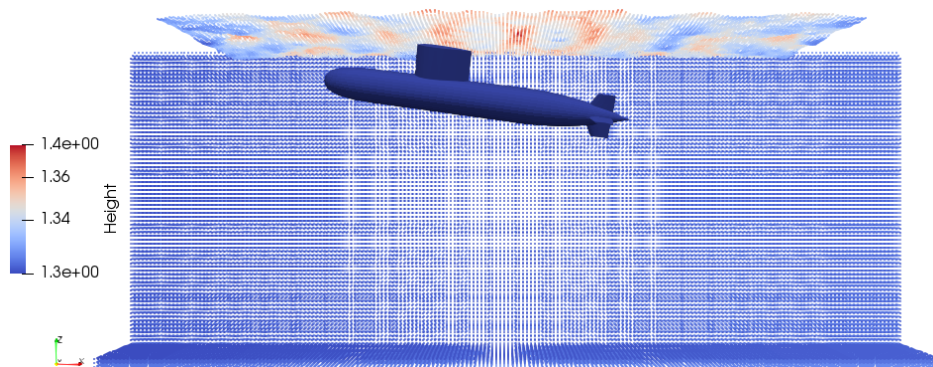
(b) t=4.0s
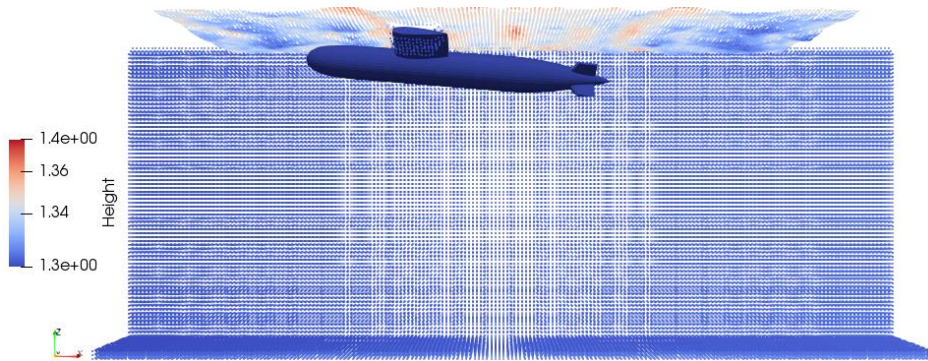
(c) t=4.5s
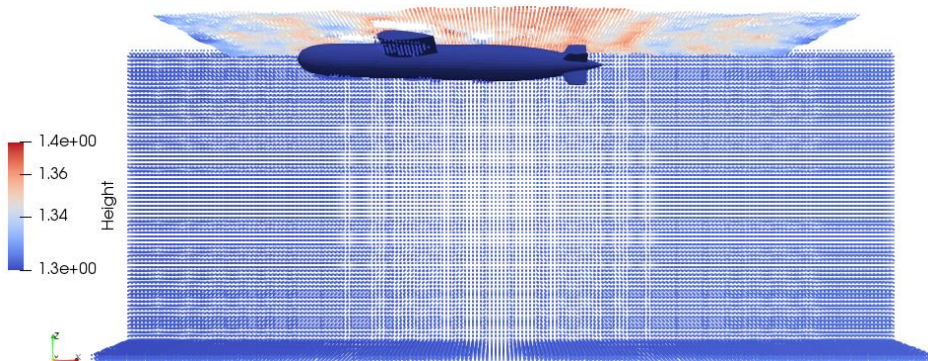
(d) t=5.0s

Figure 6.25: Submarine pitching rotational motion.

Figure 6.26 shows that the rolling rotational motion appears from t=3.0s Figure 6.26(b), confirming previous works where the more considerable effect of this motion appear to be stronger near the free surface. After t=3.5s Figure 6.26(c) the rotational motion causes a major instability producing a rotation of almost 75 degrees.

(a) t=2s

(b) t=3.0s

(c) t=3.5s

(d) t=4.0s

(e) t=4.5s

(f) t=5.0s
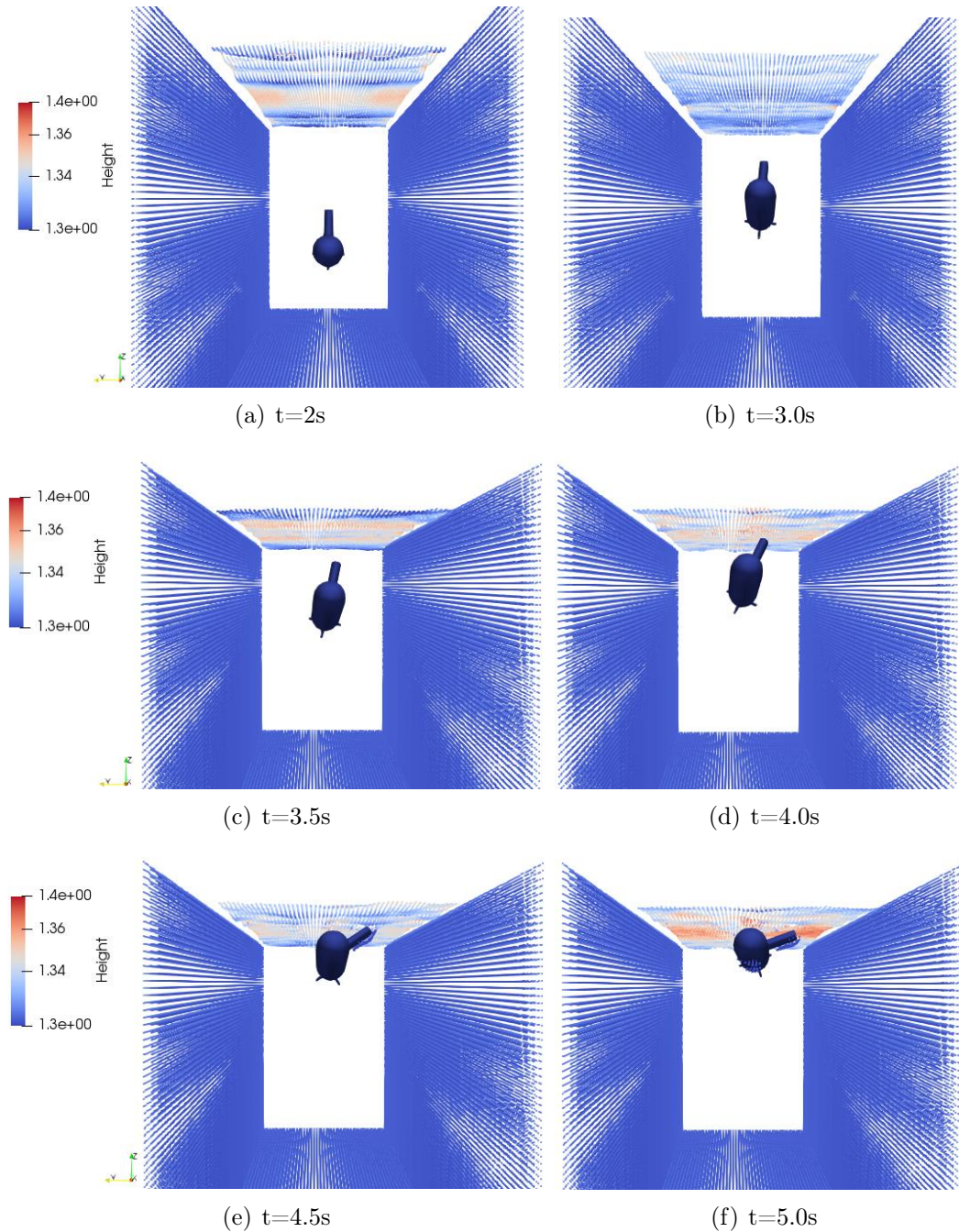
Figure 6.26: Submarine rolling rotational motion.

Finally as discussed previously, the yawing rotational motion does not contribute for the instability ascending surfacing problem. Figure 6.27 depicts briefly the linear evolution in time of the submarine ascending normal to the y-x plane. The behaviour is as expected since equilibrium forces on the horizontal y-direction do not exert any rotation in the z-axis.

(a) t=0.0s

(b) t=1.0s

(c) t=2.0s

(d) t=3.0s

(e) t=3.5s

(f) t=4.0s

(g) t=4.5s

(h) t=5.0s
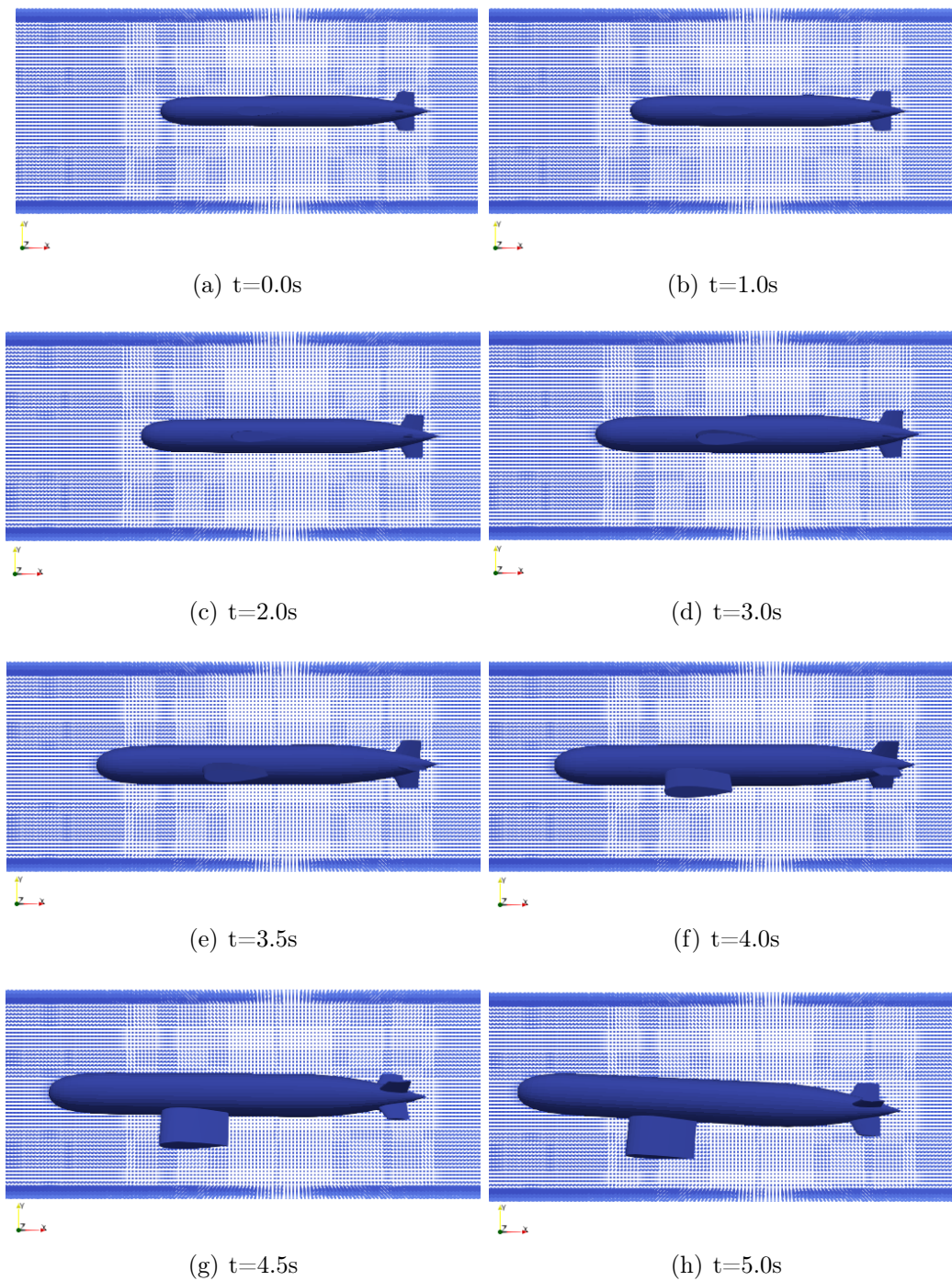
Figure 6.27: Submarine yawing rotational motion.

Figure 6.27(a) reveals that the effect of the rolling instability becomes evident from t=3.0s Figure 6.21. Finally Figure 6.27(g) depicts the almost 75 degree motion near the free surface.

7

Conclusions

This study has attended numerically the fluid solid interaction problem through five study cases. The processing stage has been performed by means of a meshless method, the Smoothing Particle Hydrodynamics using DualSPHysics. The results analysed in the moving square cylinder shows the capabilities of the software for reproducing published solution concerning the drag coefficient, however additional extensions to the numerical domain are consider necessary so as to not the results to be affected by waves reflected onto the boundaries. This may represent a problem due to the increase in computational effort while attending to 3-D problems. Therefore special attention should be given to the enhancement of boundaries. Regarding the second validation case, a good numerical agreement is highlighted regardless additional domain extensions are needed. Results confirm the credibility of DualSPHysics but enhancements to the boundaries may increase . This also turns into a motivation for the beginner user of DualSPHysics to propose and modify the code according to the phenomenon to be analysed. The third case confirms the accuracy of the software and the method, achieving reasonable results compared to those obtained in previous works studying fluid solid interactions. Although deviations may appear, acceptable results demonstrates the accuracy of SPH while challenging free surface physical phenomena. No extra effort has been introduced to deal with the fluid free surface like that carried out in cited references. Furthermore throughout all the numerical simulations no complex pre-processing stage has been prior required. Due to the Lagrangian scheme adopted by the methodology the free surface appears to deform naturally, this easily handled task accomplished by means of the SPH do present several difficulties in mesh-grid based methods, revealing then, a truthfully advantage in contrast to conventional mesh based methods.

It has been also simulated the physical phenomenon of a train when it travels at a high speed through a tunnel. This phenomenon has been accurately simulated, but the pressure values of interest do not contribute to the reliability of the SPH method for reproducing solutions obtained in previous papers. Despite the discordance in the measurements the SPH technique attempts quite effective to predict the tendency of experimental results. Finally high level oscillations apparently caused by the velocity of the train in the fluid domain do not contribute to consider DualSPHysics to be capable of predicting variable fields in quite compressible phenomena. A remarkable effort to the equation of state and the formulation concerning compressibility is demanded.

Finally a submarine hull ascending motion has been effectively reproduced confirming previous evidence with other numerical solutions. In contrast to the conventional mesh-grid based methods implemented in this kind of study cases, an efficient and innovative fluid solid interaction algorithm using the SPH technique has highlighted its advantage due to the no dependency of a previous meshing process. What is more, no additional softwares are required since the SPH is evidently is able o reproduce experimental phenomena while including both, rigid body equations of motion and the equations pertaining to the fluid dynamics.

In conclusion the Smoothed Particle Hydrodynamics numerical technique seems to be an excellent numerical tool to analysed and predict phenomena regarding fluid solid interactions. The SPH methodology in its weakly incompressible version has been presented from its fundamentals and implemented through the DualSPHysics software. The parallel scheme of DualSPHysics aided to massively extend calculations and reduce runtime. Five cases have been numerically reproduced finding good agreement with other authors solutions. Meaningful results have been obtained and notwithstanding in one case was no possible at all to achieve the expected measurements the novel SPH methodology is evident to show significant advantages while challenging problems where conventional mesh grid based methods find difficulties due to mesh dependency , the complexity of the geometries involved and the time consuming meshing process.

Current implementation and future of SPH

Most of the current noteworthy developments, challenges, and future issues concerned to SPH are deeply presented and discussed in (Violeau and Rogers, 2016), from which the most relevant subjects are briefed below:

▶ **Turbulence** (Dalrymple and Rogers, 2006; Ferrand et al., 2013; Mayrhofer et al., 2015; Shao, 2006; Violeau and Piccon, 2001).

▶ **Multi-fluid SPH** (Fourtakas et al., 2013; Grenier et al., 2009; Ulrich et al., 2013).

▶ **Numerical stability** (Violeau and Leroy, 2014, 2015)

▶ **Variable resolution** (Barcarolo et al., 2014; Vacondio et al., 2012, 2013)

▶ **Coupling** (Altomare et al., 2014; Li et al., 2014a,b, 2015)

In (Violeau and Rogers, 2016), a general panorama as a bellwether in moving SPH forward is exhibited by considering the main activities either in Industry or Research fields.

A

Alternative formulation of the gradient and divergence operators in SPH

What literature traditionally consider straightforward

The SPH formality

Beginning with equation (4.1)

$$\langle f(r_i)\rangle = \int_{\partial\Omega} f(r_j)W(r_i - r_j)dr_j, \tag{A.1}$$

now simplifying the notation as follows,

$$f(r_i) = f_i,$$
$$f(r_j) = f_j,$$
$$W(r_i - r_j) = W_{ij},$$

then equation (A.1) becomes

$$\langle f_i\rangle = \int_{\partial\Omega} f_j W_{ij} dr_j, \tag{A.2}$$

multiplying and dividing the right hand side of the anterior equation by $\dfrac{\rho_j}{\rho_j}$,

$$\langle f_i\rangle = \int_{\partial\Omega} \frac{\rho_j}{\rho_j} f_j W_{ij} dr_j,$$
$$= \int_{\partial\Omega} \frac{f_j}{\rho_j} W_{ij}\rho_j dr_j,$$

as the region of integration is assumed to be a volume integral the term $\rho_j dr_j$ may be change by m_j, then

$$\langle f_i \rangle = \int_{\partial\Omega} \frac{f_j}{\rho_j} W_{ij} m_j, \tag{A.3}$$

performing the same process(particle representation) of reversing the Riemman summation, the next discretized equality appears,

$$f_i = \sum \frac{m_j}{\rho_j} f_j W_{ij}, \tag{A.4}$$

it is worth mentioning once this point has been reached, that i and j denotes the function evaluated at particle i and particle j respectively. Equation (A.5) represents the most common SPH summation formula. Now if f_i is considered to be $f_i = \rho_i$, using (A.5),

$$
\begin{aligned}
\rho_i &= \sum \frac{m_j}{\rho_j} \rho_j W_{ij}, \\
&= \sum_j m_j \frac{\rho_j}{\rho_j} W_{ij}, \\
&= \sum_j m_j W_{ij},
\end{aligned}
$$

in this way,

$$\rho_i = \sum_j m_j W_{ij}, \tag{A.5}$$

Following this idea, mathematical operators are developed in next subsections.

Derivative operator

Besides continuous, basic mathematical operators can be turn into the SPH representation. In this case the derivative operator is obtained. Considering,

$$\frac{\partial f_i}{\partial r_i} = \frac{\partial}{\partial r_i} \int_{\partial\Omega} f_j W_{ij} dr_j, \tag{A.6}$$

where the right hand side denotes the derivative of f with respect to r evaluated in particle i. As f_j and W_{ij} are continuous and C^1, then

$$
\begin{aligned}
\frac{\partial}{\partial r_i} \int_{\partial\Omega} f_j W_{ij} dr_j &= \int_{\partial\Omega} \frac{\partial}{\partial r_i} f_j W_{ij} dr_j, \\
&= \int_{\partial\Omega} f_j \frac{\partial W_{ij}}{\partial r_i} dr_j, \\
&= \int_{\partial\Omega} \frac{\rho_j}{\rho_j} f_j \frac{\partial W_{ij}}{\partial r_i} dr_j, \\
&= \int_{\partial\Omega} \frac{f_j}{\rho_j} \frac{\partial W_{ij}}{\partial r_i} \rho_j dr_j, \\
&= \int_M \frac{f_j}{\rho_j} \frac{\partial W_{ij}}{\partial r_i} dm_j, \\
&= \sum_j \frac{f_j}{\rho_j} \frac{\partial W_{ij}}{\partial r_i} m_j,
\end{aligned}
$$

rearranging terms,

$$
\frac{\partial f_i}{\partial r_i} = \sum_j \frac{m_j}{\rho_j} f_j \frac{\partial W_{ij}}{\partial r_i}, \tag{A.7}
$$

However the last equation is not able to equal to zero when a constant function is operated under the derivative operator. This is explained due to the definition of the kernel. Following the idea of (Danis et al., 2013) the introduction of the next product derivative shown below, enhances the derivative SPH representation to better model an accurate constant derivative. Then considering,

$$
\frac{\partial (f_i \cdot 1)}{\partial r_i} = 1 \cdot \frac{\partial f_i}{\partial r_i} + f_i \cdot \frac{\partial 1}{\partial r_i}, \tag{A.8}
$$

isolating the first term on right hand side,

$$
1 \cdot \frac{\partial f_i}{\partial r_i} = \frac{\partial (f_i \cdot 1)}{\partial r_i} - f_i \cdot \frac{\partial 1}{\partial r_i},
$$

$$
\frac{\partial f_i}{\partial r_i} = \frac{\partial f_i}{\partial r_i} - f_i \cdot \frac{\partial 1}{\partial r_i}, \tag{A.9}
$$

now applying the derivative operator SPH definition eq. (A.7),

$$
\begin{aligned}
\frac{\partial f_i}{\partial r_i} &= \frac{\partial f_i}{\partial r_i} - f_i \cdot \frac{\partial 1}{\partial r_i}, \\
&= \sum_j \frac{m_j}{\rho_j} f_j \frac{\partial W_{ij}}{\partial r_i} - f_i \cdot \sum_j \frac{m_j}{\rho_j} \cdot 1 \cdot \frac{\partial W_{ij}}{\partial r_i}, \\
&= \sum_j \frac{m_j}{\rho_j} f_j \frac{\partial W_{ij}}{\partial r_i} - f_i \cdot \sum_j \frac{m_j}{\rho_j} \frac{\partial W_{ij}}{\partial r_i}, \\
&= \sum_j \frac{m_j}{\rho_j} f_j \frac{\partial W_{ij}}{\partial r_i} - \sum_j \frac{m_j}{\rho_j} f_i \frac{\partial W_{ij}}{\partial r_i}, \\
&= \sum_j \frac{m_j}{\rho_j} \left(f_j - f_i \right) \frac{\partial W_{ij}}{\partial r_i},
\end{aligned}
$$

therefore,

$$
\frac{\partial f_i}{\partial r_i} = \sum_j \frac{m_j}{\rho_j} \left(f_j - f_i \right) \frac{\partial W_{ij}}{\partial r_i}. \tag{A.10}
$$

generalizing this formula for any conserved property, $(f_i \rho_i^n)$, the derivative of such quantity applying (A.10) results,

$$
\frac{\partial \left(f_i \rho_i^n \right)}{\partial r_i} = \rho_i^n \cdot \frac{\partial f_i}{\partial r_i} + n f_i \rho_i^{n-1} \cdot \frac{\partial \rho_i}{\partial r_i}, \tag{A.11}
$$

isolating the first term on the right hand side,

$$
\rho_i^n \cdot \frac{\partial f_i}{\partial r_i} = \frac{\partial \left(f_i \rho_i^n \right)}{\partial r_i} - n f_i \rho_i^{n-1} \cdot \frac{\partial \rho_i}{\partial r_i}, \tag{A.12}
$$

and conducting the same process like that for obtaining (A.7),

$$\rho_i^n \cdot \frac{\partial f_i}{\partial r_i} = \frac{\partial}{\partial r_i} \int_{\partial \Omega} \left(f_j \rho_j^n \right) W_{ij} dr_j - n f_i \rho_i^{n-1} \frac{\partial}{\partial r_i} \int_{\partial \Omega} \left(\rho_j W_{ij} \right) dr_j,$$

$$= \int_{\partial \Omega} \frac{\partial \left(f_j \rho_j^n W_{ij} \right)}{\partial r_i} dr_j - n f_i \rho_i^{n-1} \int_{\partial \Omega} \frac{\partial \left(\rho_j W_{ij} \right)}{\partial r_i} dr_j,$$

$$= \int_{\partial \Omega} f_j \rho_j^n \frac{\partial W_{ij}}{\partial r_i} dr_j - n f_i \rho_i^{n-1} \int_{\partial \Omega} \rho_j \frac{\partial W_{ij}}{\partial r_i} dr_j,$$

$$= \int_{\partial \Omega} \left(\frac{\rho_j}{\rho_j} \right) f_j \rho_j^n \frac{\partial W_{ij}}{\partial r_i} dr_j - n f_i \rho_i^{n-1} \int_{\partial \Omega} \left(\frac{\rho_j}{\rho_j} \right) \rho_j \frac{\partial W_{ij}}{\partial r_i} dr_j,$$

$$= \int_{\partial \Omega} \frac{\rho_j^n}{\rho_j} f_j \frac{\partial W_{ij}}{\partial r_i} \rho_j dr_j - n f_i \rho_i^{n-1} \int_{\partial \Omega} \frac{\rho_j}{\rho_j} \frac{\partial W_{ij}}{\partial r_i} \rho_j dr_j,$$

$$= \int_{M} \rho_j^{n-1} f_j \frac{\partial W_{ij}}{\partial r_i} dm_j - n f_i \rho_i^{n-1} \int_{M} \frac{\partial W_{ij}}{\partial r_i} dm_j,$$

$$= \sum_j \rho_j^{n-1} f_j \frac{\partial W_{ij}}{\partial r_i} m_j - n f_i \rho_i^{n-1} \sum_j \frac{\partial W_{ij}}{\partial r_i} m_j,$$

$$= \sum_j m_j \left(\rho_j^{n-1} f_j - n f_i \rho_i^{n-1} \right) \frac{\partial W_{ij}}{\partial r_i},$$

then the next equality is obtained,

$$\rho_i^n \cdot \frac{\partial f_i}{\partial r_i} = \sum_j m_j \left(\rho_j^{n-1} f_j - n f_i \rho_i^{n-1} \right) \frac{\partial W_{ij}}{\partial r_i}, \tag{A.13}$$

finally, isolating the derivative operator,

$$\frac{\partial f_i}{\partial r_i} = \frac{1}{\rho_i^n} \sum_j m_j \left(\rho_j^{n-1} f_j - n f_i \rho_i^{n-1} \right) \frac{\partial W_{ij}}{\partial r_i}. \tag{A.14}$$

In SPH literature n can be set equal to 1 or -1. If $n = 1$ the derivative of a constant is identically equal to zero, in contrast with the value of $n = -1$. However a value of $n = -1$ provides an equation capable of manage the momentum conservation. Now each corresponding equality is deployed below.

for $n = 1$

$$\frac{\partial f_i}{\partial r_i} = \frac{1}{\rho_i} \sum_j m_j \left(f_j - f_i \right) \frac{\partial W_{ij}}{\partial r_i}, \tag{A.15}$$

for $n = -1$,

$$\frac{\partial f_i}{\partial r_i} = \rho_i \sum_j m_j \left(\frac{f_j}{\rho_j^2} + \frac{f_i}{\rho_i^2} \right) \frac{\partial W_{ij}}{\partial r_i}. \tag{A.16}$$

Continuing with the deduction of a mathematical SPH representation of the operators that appear naturally in the Navier Stokes equations, the gradient and divergence equivalence in SPH is now presented.

Gradient of a function

Remembering the definition of the gradient operator,

$$\nabla = \frac{\partial}{\partial r^1} \boldsymbol{i}_1 + \frac{\partial}{\partial r^2} \boldsymbol{i}_2 + \frac{\partial}{\partial r^3} \boldsymbol{i}_3 \tag{A.17}$$

now considering the next scalar function evaluated in particle i as f_i, and applying the gradient operator,

$$\nabla f_i = \frac{\partial f_i}{\partial r^1} \boldsymbol{i}_1 + \frac{\partial f_i}{\partial r^2} \boldsymbol{i}_2 + \frac{\partial f_i}{\partial r^3} \boldsymbol{i}_3 \tag{A.18}$$

then implementing equation (A.14) on each derivative term,

$$
\begin{aligned}
\nabla f_i =& \frac{\partial f_i}{\partial r_i^1} \boldsymbol{i}_1 + \frac{\partial f_i}{\partial r_i^2} \boldsymbol{i}_2 + \frac{\partial f_i}{\partial r_i^3} \boldsymbol{i}_3, \\
=& \frac{1}{\rho_i^n} \sum_j m_j \left(\rho_j^{n-1} f_j - n f_i \rho_i^{n-1} \right) \left(\frac{\partial W_{ij}}{\partial r_i^1} \boldsymbol{i}_1 + \frac{\partial W_{ij}}{\partial r_i^2} \boldsymbol{i}_2 + \frac{\partial W_{ij}}{\partial r_i^3} \boldsymbol{i}_3 \right), \\
=& \frac{1}{\rho_i^n} \sum_j m_j \left(\rho_j^{n-1} f_j - n f_i \rho_i^{n-1} \right) \left(\frac{\partial W_{ij}}{\partial r_i^k} \boldsymbol{i}_k \right), \\
=& \frac{1}{\rho_i^n} \sum_j m_j \left(\rho_j^{n-1} f_j - n f_i \rho_i^{n-1} \right) \left(\nabla_i W_{ij} \right),
\end{aligned}
$$

therefore,

$$\nabla f_i = \frac{1}{\rho_i^n} \sum_j m_j \left(\rho_j^{n-1} f_j - n f_i \rho_i^{n-1} \right) \left(\nabla_i W_{ij} \right), \tag{A.19}$$

once again, considering both values of n. The next equations are obtained for n=1 and n=-1 respectively,

$$\nabla f_i = \frac{1}{\rho_i} \sum_j m_j \left(f_j - f_i \right) \nabla_i W_{ij}, \tag{A.20}$$

$$\nabla f_i = \rho_i \sum_j m_j \left(\frac{f_j}{\rho_j^2} + \frac{f_i}{\rho_i^2} \right) \nabla_i W_{ij}. \tag{A.21}$$

Divergence of a function

Given the divergence definition applied to a vectorial function evaluated in particle i,

$$
\begin{aligned}
\nabla_i \cdot \boldsymbol{f}_i &= \frac{\partial}{\partial r_i^k} \boldsymbol{i}_k \cdot f_i^z \boldsymbol{i}_z, \\
&= \frac{\partial}{\partial r_i^k} f_i^z \left(\boldsymbol{i}_k \cdot \boldsymbol{i}_z \right), \\
&= \frac{\partial}{\partial r_i^k} f_i^z \delta_{kz}, \\
&= \frac{\partial f_i^k}{\partial r_i^k}.
\end{aligned}
$$

with $k \in \{1, 2, 3\}$. Applying again equation (A.14),

$$
\begin{aligned}
\nabla_i \cdot \boldsymbol{f}_i &= \frac{\partial f_i^k}{\partial r_i^k}, \\
&= \frac{1}{\rho_i^n} \sum_j m_j \left(\rho_j^{n-1} f_j^k - n f_i^k \rho_i^{n-1} \right) \left(\frac{\partial W_{ij}}{\partial r_i^k} \right),
\end{aligned}
\qquad \text{(A.22)}
$$

turning back to index notation,

$$
\begin{aligned}
\frac{1}{\rho_i^n} \sum_j m_j \left(\rho_j^{n-1} f_j^k - n f_i^k \rho_i^{n-1} \right) \frac{\partial W_{ij}}{\partial r_i^k} \delta_{kz} &= \frac{1}{\rho_i^n} \sum_j m_j \left(\rho_j^{n-1} f_j^z - n f_i^z \rho_i^{n-1} \right) \frac{\partial W_{ij}}{\partial r_i^k} \left(\boldsymbol{i}_k \cdot \boldsymbol{i}_z \right), \\
&= \frac{1}{\rho_i^n} \sum_j m_j \left(\rho_j^{n-1} f_j^z - n f_i^z \rho_i^{n-1} \right) \boldsymbol{i}_z \cdot \frac{\partial W_{ij}}{\partial r_i^k} \boldsymbol{i}_k,
\end{aligned}
$$

using the distribution axiom from vectorial spaces, $\boldsymbol{i}_z$ can be distributed as follows,

$$
\frac{1}{\rho_i^n} \sum_j m_j \left(\rho_j^{n-1} f_j^z \boldsymbol{i}_z - n f_i^z \boldsymbol{i}_z \rho_i^{n-1} \right) \cdot \frac{\partial W_{ij}}{\partial r_i^k} \boldsymbol{i}_k = \frac{1}{\rho_i^n} \sum_j m_j \left(\rho_j^{n-1} \boldsymbol{f}_j - n \boldsymbol{f}_i \rho_i^{n-1} \right) \cdot \frac{\partial W_{ij}}{\partial r_i^k} \boldsymbol{i}_k,
$$

finally,

$$
\nabla_i \cdot \boldsymbol{f} = \frac{1}{\rho_i^n} \sum_j m_j \left(\rho_j^{n-1} \boldsymbol{f}_j - n \boldsymbol{f}_i \rho_i^{n-1} \right) \cdot \nabla_i W_{ij}
\qquad \text{(A.23)}
$$

if n=1,

$$
\nabla_i \cdot \boldsymbol{f}_i = \frac{1}{\rho_i} \sum_j m_j \left(\boldsymbol{f}_j - \boldsymbol{f}_i \right) \cdot \nabla_i W_{ij},
\qquad \text{(A.24)}
$$

if n=-1,

$$
\nabla_i \cdot \boldsymbol{f}_i = \rho_i \sum_j m_j \left(\frac{\boldsymbol{f}_j}{\rho_j^2} + \frac{\boldsymbol{f}_i}{\rho_i^2} \right) \cdot \nabla_i W_{ij}.
\qquad \text{(A.25)}
$$

Bibliography

Altomare, C., Suzuki, T., Dominguez, J. M., Crespo, A. J., Gomez-Gesteira, M., and Caceres, I. (2014). A hybrid numerical model for coastal engineering problems. *Coastal Engineering Proceedings*, 1(34):60.

Anderson, J. (1995). *Computational Fluid Dynamics: The Basics with Applications*. McGraw-Hill international editions. McGraw-Hill.

Antuono, M., Colagrossi, A., and Marrone, S. (2012). Numerical diffusive terms in weakly-compressible sph schemes. *Computer Physics Communications*, 183(12):2570 – 2580.

B. Kajtar, J. and J. Monaghan, J. (2009). On the fish-like swimming of linked bodies with and without skin.

Barcarolo, D. A., Le Touzé, D., Oger, G., and De Vuyst, F. (2014). Adaptive particle refinement and derefinement applied to the smoothed particle hydrodynamics method. *Journal of Computational Physics*, 273:640–657.

Batchelor, G. K. (2000). *An Introduction to Fluid Dynamics*. Cambridge Mathematical Library. Cambridge University Press.

Belytschko, T., Krongauz, Y., Organ, D., Fleming, M., and Krysl, P. (1996). Meshless methods: an overview and recent developments. *Computer methods in applied mechanics and engineering*, 139(1-4):3–47.

Benz, W. (1988). Applications of smooth particle hydrodynamics (sph) to astrophysical problems. *Computer Physics Communications*, 48(1):97–105.

Benz, W. and Asphaug, E. (1994). Impact simulations with fracture. i. method and tests. *Icarus*, 107(1):98–116.

Benz, W. and Asphaug, E. (1995). Simulations of brittle solids using smooth particle hydrodynamics. *Computer physics communications*, 87(1-2):253–265.

Berczik, P. (2000). Modeling the star formation in galaxies using the chemodynamicalsph code. *Astrophysics and Space Science*, 271(2):103–126.

Bettle, M. C., Gerber, A. G., and Watt, G. D. (2009). Unsteady analysis of the six dof motion of a buoyantly rising submarine. *Computers & Fluids*, 38(9):1833–1849.

Bettle, M. C., Gerber, A. G., and Watt, G. D. (2014a). Using reduced hydrodynamic models to accelerate the predictor–corrector convergence of implicit 6-dof urans submarine manoeuvring simulations. *Computers & Fluids*, 102:215–236.

Bettle, M. C., Gerber, A. G., and Watt, G. D. (2014b). Using reduced hydrodynamic models to accelerate the predictor–corrector convergence of implicit 6-dof urans submarine manoeuvring simulations. *Computers & Fluids*, 102:215–236.

Bonet, J. and Kulasegaram, S. (2000). Correction and stabilization of smooth particle hydrodynamics methods with applications in metal forming simulations. *International journal for numerical methods in engineering*, 47(6):1189–1214.

Bouscasse, B., Colagrossi, A., Marrone, S., and Antuono, M. (2013). Nonlinear water wave interaction with floating bodies in sph. *Journal of Fluids and Structures*, 42:112–129.

Braza, M., Chassaing, P., and Minh, H. H. (1986). Numerical study and physical analysis of the pressure and velocity fields in the near wake of a circular cylinder. *Journal of fluid mechanics*, 165:79–130.

Bui, H., Fukagawa, R., and Sato, K. (2006). Smoothed particle hydrodynamics for soil mechanics. *proceedings of Numerical Methods in Geotechnical Engineering, Graz*, pages 275–281.

Bui, H. H., Fukagawa, R., Sako, K., and Ohno, S. (2008). Lagrangian meshfree particles method (sph) for large deformation and failure flows of geomaterial using elastic–plastic soil constitutive model. *International Journal for Numerical and Analytical Methods in Geomechanics*, 32(12):1537–1570.

Calhoun, D. (2002). A cartesian grid method for solving the two-dimensional streamfunction-vorticity equations in irregular regions. *Journal of computational physics*, 176(2):231–275.

Canelas, R. . (2015). *Numerical modeling of fully coupled solid-fluid flows*. Phd thesis, Universidade de Lisboa, Instituto Superior Técnico, Portugal.

Canelas, R. B., Domínguez, J. M., Crespo, A. J., Gómez-Gesteira, M., and Ferreira, R. M. (2015). A smooth particle hydrodynamics discretization for the modelling of free surface flows and rigid body dynamics. *International Journal for Numerical Methods in Fluids*, 78(9):581–593.

Cercos-Pita, J. L. (2015). Aquagpusph, a new free 3d sph solver accelerated with opencl. *Computer Physics Communications*, 192:295–312.

Chen, J., Beraun, J., and Carney, T. (1999). A corrective smoothed particle method for boundary value problems in heat conduction. *International Journal for Numerical Methods in Engineering*, 46(2):231–252.

Chu, C.-R., Chien, S.-Y., Wang, C.-Y., and Wu, T.-R. (2014). Numerical simulation of two trains intersecting in a tunnel. *Tunnelling and Underground Space Technology*, 42(Supplement C):161 – 174.

Cleary, P., Prakash, M., and Ha, J. (2006). Novel applications of smoothed particle hydrodynamics (sph) in metal forming. *Journal of materials processing technology*, 177(1):41–48.

Cleary, P. W. (1998). Modelling confined multi-material heat and mass flows using sph. *Applied Mathematical Modelling*, 22(12):981–993.

Cleary, P. W. and Ha, J. (2000). Three dimensional modelling of high pressure die casting. *International Journal of Cast Metals Research*, 12(6):357–365.

Colagrossi, A. (2005). A meshless lagrangian method for free-surface and interface flows with fragmentation. *These, Universita di Roma*.

Colagrossi, A. (2011). *2D Incompressible flow around a moving square inside a rectangular box. 2D SPH Validation*.

Colagrossi, A. and Landrini, M. (2003). Numerical simulation of interfacial flows by smoothed particle hydrodynamics. *Journal of computational physics*, 191(2):448–475.

Colicchio, G., Greco, M., Miozzi, M., and Lugni, C. (2009). Experimental and numerical investigation of the water-entry and water-exit of a circular cylinder. In *Proceedings of the 24th Int. Workshop on Water Waves and Floating Bodies, Zelenogorsk, Russia, Apr*, pages 19–22.

Crespo, A., Gómez-Gesteira, M., and Dalrymple, R. A. (2007a). 3d sph simulation of large waves mitigation with a dike. *Journal of Hydraulic Research*, 45(5):631–642.

Crespo, A., Gómez-Gesteira, M., and Dalrymple, R. A. (2007b). Boundary conditions generated by dynamic particles in sph methods. *CMC-TECH SCIENCE PRESS-*, 5(3):173.

Crespo, A., Gómez-Gesteira, M., and Dalrymple, R. A. (2008). Modeling dam break behavior over a wet bed by a sph technique. *Journal of waterway, port, coastal, and ocean engineering*, 134(6):313–320.

Crespo, A. J., Domínguez, J. M., Rogers, B. D., Gómez-Gesteira, M., Longshaw, S., Canelas, R., Vacondio, R., Barreiro, A., and García-Feal, O. (2015). Dualsphysics: Open-source parallel cfd solver based on smoothed particle hydrodynamics (sph). *Computer Physics Communications*, 187:204–216.

Dalrymple, R. and Rogers, B. (2006). Numerical modeling of water waves with the sph method. *Coastal engineering*, 53(2):141–147.

Danis, M., Orhan, M., and Ecder, A. (2013). Isph modelling of transient natural convection. *International Journal of Computational Fluid Dynamics*, 27(1):15–31.

Das, R. and Cleary, P. (2010). Effect of rock shapes on brittle fracture using smoothed particle hydrodynamics. *Theoretical and Applied Fracture Mechanics*, 53(1):47–60.

Domínguez, J. M., Crespo, A. J., and Gómez-Gesteira, M. (2013a). Optimization strategies for cpu and gpu implementations of a smoothed particle hydrodynamics method. *Computer Physics Communications*, 184(3):617–627.

Domínguez, J. M., Crespo, A. J., Valdez-Balderas, D., Rogers, B. D., and Gómez-Gesteira, M. (2013b). New multi-gpu implementation for smoothed particle hydrodynamics on heterogeneous clusters. *Computer Physics Communications*, 184(8):1848–1860.

E. Danis, M., Orhan, M., and Ecder, A. (2013). Isph modelling of transient natural convection. 27:15–31.

Fekken, G. (2004). Numerical simulation of free surface ow with moving rigid bodies. ph. d. thesis.

Ferrand, M., Laurence, D., Rogers, B. D., Violeau, D., and Kassiotis, C. (2013). Unified semi-analytical wall boundary conditions for inviscid, laminar or turbulent flows in the meshless sph method. *International Journal for Numerical Methods in Fluids*, 71(4):446–472.

Fourtakas, G., Rogers, B. D., and Laurence, D. R. (2013). Modelling sediment resuspension in industrial tanks using sph. *La Houille Blanche*, (2):39–45.

Franke, R., Rodi, W., and Schönung, B. (1990). Numerical calculation of laminar vortex-shedding flow past cylinders. *Journal of Wind Engineering and Industrial Aerodynamics*, 35:237–257.

Gallati, M., Braschi, G., and Falappi, S. (2005). Sph simulations of the waves produced by a falling mass into a reservoir. *Nuovo Cimento-C*, 28(2):129–140.

García-Senz, D., Bravo, E., and Woosley, S. (1999). Single and multiple detonations in white dwarfs. *Astronomy and astrophysics*, 349:177–188.

Ghazali, J. N. and Kamsin, A. (2008). A real time simulation and modeling of flood hazard. In *WSEAS International Conference. Proceedings. Mathematics and Computers in Science and Engineering*, number 12. WSEAS.

Gingold, R. A. and Monaghan, J. J. (1977). Smoothed particle hydrodynamics: theory and application to non-spherical stars. *Monthly notices of the royal astronomical society*, 181(3):375–389.

Gómez-Gesteira, M. and Dalrymple, R. A. (2004). Using a three-dimensional smoothed particle hydrodynamics method for wave impact on a tall structure. *Journal of waterway, port, coastal, and ocean engineering*, 130(2):63–69.

Gotoh, H., Shao, S., and Memita, T. (2004). Sph-les model for numerical investigation of wave interaction with partially immersed breakwater. *Coastal Engineering Journal*, 46(01):39–63.

Gray, J. and Monaghan, J. (2004). Numerical modelling of stress fields and fracture around magma chambers. *Journal of Volcanology and Geothermal Research*, 135(3):259–283.

Gray, J., Monaghan, J., and Swift, R. (2001). Sph elastic dynamics. *Computer methods in applied mechanics and engineering*, 190(49):6641–6662.

Greenhow, M., Vinje, T., Brevig, P., and Taylor, J. (1981). Nonlinear ship motions. *Proceedings of the 3rd. Int. Conf. on Num. Ship Hydro.*

Greenhow, M., Vinje, T., Brevig, P., and Taylor, J. (1982). A theoretical and experimental study of the capsize of salter's duck in extreme waves. *Journal of Fluid Mechanics*, 118:221–239.

Grenier, N., Antuono, M., Colagrossi, A., Le Touzé, D., and Alessandrini, B. (2009). An hamiltonian interface sph formulation for multi-fluid and free surface flows. *Journal of Computational Physics*, 228(22):8380–8393.

Ha, J. and Cleary, P. W. (2000). Comparison of sph simulations of high pressure die casting with the experiments and vof simulations of schmid and klein. *International Journal of Cast Metals Research*, 12(6):409–418.

Ha, J. and Cleary, P. W. (2005). Simulation of high pressure die filling of a moderately complex industrial object using smoothed particle hydrodynamics. *International Journal of Cast Metals Research*, 18(2):81–92.

Hadžić, I., Hennig, J., Perić, M., and Xing-Kaeding, Y. (2005). Computation of flow-induced motion of floating bodies. *Applied mathematical modelling*, 29(12):1196–1210.

Havelock, T. H. (1936). The forces on a circular cylinder submerged in a uniform stream. *Proceedings of the Royal Society of London A: Mathematical, Physical and Engineering Sciences*, 157(892):526–534.

Herrera, P. A., Massabó, M., and Beckie, R. D. (2009). A meshless method to simulate solute transport in heterogeneous porous media. *Advances in water resources*, 32(3):413–429.

Hieber, S. E. and Koumoutsakos, P. (2008). A lagrangian particle method for the simulation of linear and nonlinear elastic models of soft tissue. *Journal of Computational Physics*, 227(21):9195–9215.

Hieber, S. E., Walther, J. H., and Koumoutsakos, P. (2004). Remeshed smoothed particle hydrodynamics simulation of the mechanical behavior of human organs. *Technology and Health Care*, 12(4):305–314.

Hosseini, S., Manzari, M., and Hannani, S. (2007). A fully explicit three-step sph algorithm for simulation of non-newtonian fluid flow. *International Journal of Numerical Methods for Heat & Fluid Flow*, 17(7):715–735.

Hu, X. and Adams, N. A. (2007). An incompressible multi-phase sph method. *Journal of computational physics*, 227(1):264–278.

Hultman, J. and Pharasyn, A. (1999). Hierarchical, dissipative formation of elliptical galaxies: is thermal instability the key mechanism?. hydrodynamical simulations including supernova feedback, multi-phase gas and metal enrichment in cdm: structure and dynamics of elliptical galaxies. *Astronomy and Astrophysics*, 347:769–798.

Hunter, J. (1992). *Surface tension in smoothed particle hydrodynamics*. PhD thesis, Honours thesis, Mathematics Department, Monash University, Melbourne, Australia.

Iglesias, A. S., Rojas, L. P., and Rodríguez, R. Z. (2004). Simulation of anti-roll tanks and sloshing type problems with smoothed particle hydrodynamics. *Ocean Engineering*, 31(8):1169–1192.

Jeong, J., Jhon, M., Halow, J., and Van Osdol, J. (2003). Smoothed particle hydrodynamics: Applications to heat conduction. *Computer Physics Communications*, 153(1):71–84.

Jiang, F. and Sousa, A. C. (2006). Sph numerical modeling for ballistic-diffusive heat conduction. *Numerical Heat Transfer, Part B: Fundamentals*, 50(6):499–515.

Jutzi, M., Benz, W., and Michel, P. (2008). Numerical simulations of impacts involving porous bodies: I. implementing sub-resolution porosity in a 3d sph hydrocode. *Icarus*, 198(1):242–255.

Kajtar, J. and Monaghan, J. (2010). On the dynamics of swimming linked bodies. *European Journal of Mechanics-B/Fluids*, 29(5):377–386.

Kajtar, J. and Monaghan, J. J. (2008). Sph simulations of swimming linked bodies. *Journal of Computational Physics*, 227(19):8568–8587.

Kipfer, P. and Westermann, R. (2006). Realistic and interactive simulation of rivers. In *Proceedings of Graphics Interface 2006*, pages 41–48. Canadian Information Processing Society.

Kleiber, M. (1998). *Handbook of Computational Solid Mechanics: Survey and Comparison of Contemporary Methods*. Springer Berlin Heidelberg.

Koshizuka, S., Nobe, A., and Oka, Y. (1998). Numerical analysis of breaking waves using the moving particle semi-implicit method. *International Journal for Numerical Methods in Fluids*, 26(7):751–769.

Laigle, D., Lachamp, P., and Naaim, M. (2007). Sph-based numerical investigation of mudflow and other complex fluid flow interactions with structures. *Computational Geosciences*, 11(4):297–306.

Lee, W. H. (2000). Newtonian hydrodynamics of the coalescence of black holes with neutron stars—iii. irrotational binaries with a stiff equation of state. *Monthly Notices of the Royal Astronomical Society*, 318(2):606–624.

Lee, W. H. and Kluzniak, W. (1999). Newtonian hydrodynamics of the coalescence of black holes with neutron stars—ii. tidally locked binaries with a soft equation of state. *Monthly Notices of the Royal Astronomical Society*, 308(3):780–794.

Leimkuhler, B. J., Reich, S., and Skeel, R. D. (1996). Integration methods for molecular dynamics. *IMA Volumes in Mathematics and its Applications*, 82:161–186.

LeVeque, R. (2002). *Finite Volume Methods for Hyperbolic Problems*. Cambridge Texts in Applied Mathematics. Cambridge University Press.

Li, S. and Liu, W. (2007). *Meshfree Particle Methods*. Springer Berlin Heidelberg.

Li, S. and Liu, W. K. (2002). Meshfree and particle methods and their applications. *Applied Mechanics Reviews*, 55(1):1–34.

Li, Z., Leduc, J., Combescure, A., and Leboeuf, F. (2014a). Coupling of sph-ale method and finite element method for transient fluid–structure interaction. *Computers & Fluids*, 103:6–17.

Li, Z., Leduc, J., Combescure, A., and Leboeuf, F. (2014b). Coupling of sph-ale method and finite element method for transient fluid–structure interaction. 103:6–17.

Li, Z., Leduc, J., Nunez-Ramirez, J., Combescure, A., and Marongiu, J.-C. (2015). A non-intrusive partitioned approach to couple smoothed particle hydrodynamics and finite element methods for transient fluid-structure interaction problems with large interface motion. *Comput. Mech.*, 55(4):697–718.

Libersky, L. D. and Petschek, A. (1991). Smooth particle hydrodynamics with strength of materials. In *Advances in the free-Lagrange method including contributions on adaptive gridding and the smooth particle hydrodynamics method*, pages 248–257. Springer.

Libersky, L. D., Petschek, A. G., Carney, T. C., Hipp, J. R., and Allahdadi, F. A. (1993). High strain lagrangian hydrodynamics: a three-dimensional sph code for dynamic material response. *Journal of computational physics*, 109(1):67–75.

Liu, C., Zheng, X., and Sung, C. (1998). Preconditioned multigrid methods for unsteady incompressible flows. *Journal of Computational Physics*, 139(1):35–57.

Liu, G. (2009). *Meshfree Methods: Moving Beyond the Finite Element Method, Second Edition*. CRC Press.

Liu, G. and Han, X. (2003). *Computational Inverse Techniques in Nondestructive Evaluation*. CRC Press.

Liu, G. and Liu, M. (2003). *Smoothed Particle Hydrodynamics: A Meshfree Particle Method*. World Scientific.

Liu, G. and Quek, S. (2013). *The Finite Element Method: A Practical Course*. Elsevier Science.

Liu, G. and Zhang, G. (2013). *Smoothed Point Interpolation Methods: G Space Theory and Weakened Weak Forms*. World Scientific Publishing Company.

Liu, G.-R. (2002). *Mesh free methods: moving beyond the finite element method*. CRC press.

Liu, J.-L. (2004). Computations of two passing-by high-speed trains by a relaxation overset-grid algorithm. *International journal for numerical methods in fluids*, 44(12):1299–1315.

Liu, M. and Liu, G. (2005). Meshfree particle simulation of micro channel flows with surface tension. *Computational Mechanics*, 35(5):332–341.

Liu, M. and Liu, G. (2010a). Smoothed particle hydrodynamics (sph): an overview and recent developments. *Archives of computational methods in engineering*, 17(1):25–76.

Liu, M., Liu, G., and Lam, K. (2002). Investigations into water mitigation using a meshless particle method. *Shock waves*, 12(3):181–195.

Liu, M., Liu, G., and Lam, K. (2003a). Comparative study of the real and artificial detonation models in underwater explosions. *Electron Model*, 25(2):113–124.

Liu, M., Liu, G., and Lam, K. (2003b). Computer simulation of flip-chip underfill encapsulation process using meshfree particle method. *International Journal of Computational Engineering Science*, 4(02):405–408.

Liu, M., Liu, G., and Lam, K. (2003c). A one-dimensional meshfree particle formulation for simulating shock waves. *Shock Waves*, 13(3):201–211.

Liu, M., Shao, J., and Li, H. (2014). An sph model for free surface flows with moving rigid objects. *International Journal for Numerical Methods in Fluids*, 74(9):684–697.

Liu, M. B. and Liu, G. R. (2010b). Smoothed particle hydrodynamics (sph): an overview and recent developments. *Archives of Computational Methods in Engineering*, 17(1):25–76.

Lo, E. Y. and Shao, S. (2002). Simulation of near-shore solitary wave mechanics by an incompressible sph method. *Applied Ocean Research*, 24(5):275 – 286.

Lucy, L. B. (1977). A numerical approach to the testing of the fission hypothesis. *The astronomical journal*, 82:1013–1024.

Mackay, M. (2003). *The standard submarine model: a survey of static hydrodynamic experiments and semiempirical predictions*.

Marrone, S., Colagrossi, A., Antuono, M., Colicchio, G., and Graziani, G. (2013). An accurate sph modeling of viscous flows around bodies at low and moderate reynolds numbers. *Journal of Computational Physics*, 245:456–475.

Maruzewski, P., Touzé, D. L., Oger, G., and Avellan, F. (2010). Sph high-performance computing simulations of rigid solids impacting the free-surface of water. *Journal of Hydraulic Research*, 48(S1):126–134.

Mayrhofer, A., Laurence, D., Rogers, B., and Violeau, D. (2015). Dns and les of 3-d wall-bounded turbulence using smoothed particle hydrodynamics. *Computers & Fluids*, 115:86 – 97.

Mokos, A., Rogers, B., Stansby, P., and Domínguez, J. (2014). A multi-phase particle shifting algorithm for sph simulations for violent hydrodynamics on a gpu. *Proceedings of the 9th SPHERIC*, pages 1–8.

Molteni, D. and Colagrossi, A. (2009). A simple procedure to improve the pressure evaluation in hydrodynamic context using the sph. *Computer Physics Communications*, 180(6):861 – 872.

Monaghan, J. (1985). Particle methods for hydrodynamics. *Computer Physics Reports*, 3(2):71–124.

Monaghan, J. (1990). Modelling the universe. In *Astronomical Society of Australia, Proceedings*, volume 8, pages 233–237.

Monaghan, J. (2012). Smoothed particle hydrodynamics and its diverse applications. *Annual Review of Fluid Mechanics*, 44:323–346.

Monaghan, J. and Gingold, R. (1983). Shock simulation by the particle method sph. *Journal of computational physics*, 52(2):374–389.

Monaghan, J., Kos, A., and Issa, N. (2003). Fluid motion generated by impact. *Journal of waterway, port, coastal, and ocean engineering*, 129(6):250–259.

Monaghan, J. J. (1992). Smoothed particle hydrodynamics. *Annual review of astronomy and astrophysics*, 30(1):543–574.

Monaghan, J. J. (1994). Simulating free surface flows with sph. *Journal of computational physics*, 110(2):399–406.

Monaghan, J. J. and Kajtar, J. B. (2009). Sph particle boundary forces for arbitrary boundaries. *Computer Physics Communications*, 180(10):1811–1820.

Monaghan, J. J. and Lattanzio, J. C. (1985). A refined particle method for astrophysical problems. *Astronomy and astrophysics*, 149:135–143.

Monaghan, J. J. and Lattanzio, J. C. (1991). A simulation of the collapse and fragmentation of cooling molecular clouds. *The Astrophysical Journal*, 375:177–189.

Morris, J. P., Fox, P. J., and Zhu, Y. (1997). Modeling low reynolds number incompressible flows using sph. *Journal of computational physics*, 136(1):214–226.

Moshari, S., Nikseresht, A. H., and Mehryar, R. (2014). Numerical analysis of two and three dimensional buoyancy driven water-exit of a circular cylinder. *International Journal of Naval Architecture and Ocean Engineering*, 6(2):219–235.

BIBLIOGRAPHY

Moulinec, C., Issa, R., Marongiu, J., and Violeau, D. (2008). Parallel 3-d sph simulations. *Computer Modeling in Engineering and Sciences*, 25(3):133.

Moyo, S. and Greenhow, M. (2000). Free motion of a cylinder moving below and through a free surface. 22:31–44.

Müller, M., Schirm, S., and Teschner, M. (2004). Interactive blood simulation for virtual surgery based on smoothed particle hydrodynamics. *Technology and Health Care*, 12(1):25–31.

Ng, Y. T., Min, C., and Gibou, F. (2009). An efficient fluid–solid coupling algorithm for single-phase flows. *Journal of Computational Physics*, 228(23):8807–8829.

Nugent, S. and Posch, H. (2000). Liquid drops and surface tension with smoothed particle applied mechanics. *Physical Review E*, 62(4):4968.

Omidvar, P., Stansby, P. K., and Rogers, B. D. (2013). Sph for 3d floating bodies using variable mass particle distribution. *International Journal for Numerical Methods in Fluids*, 72(4):427–452.

Pastor, M., Haddad, B., Sorbino, G., Cuomo, S., and Drempetic, V. (2009). A depth-integrated, coupled sph model for flow-like landslides and related phenomena. *International Journal for numerical and analytical methods in geomechanics*, 33(2):143–172.

Rasio, F. A. and Lombardi, J. C. (1999). Smoothed particle hydrodynamics calculations of stellar interactions. *Journal of Computational and Applied Mathematics*, 109(1):213–230.

Ricco, P., Baron, A., and Molteni, P. (2007). Nature of pressure waves induced by a high-speed train travelling through a tunnel. *Journal of Wind Engineering and Industrial Aerodynamics*, 95(8):781–808.

Rogers, B. D., Dalrymple, R. A., and Stansby, P. K. (2010). Simulation of caisson breakwater movement using 2-d sph. *Journal of Hydraulic Research*, 48(sup1):135–141.

Rook, R., Yildiz, M., and Dost, S. (2007). Modeling transient heat transfer using sph and implicit time integration. *Numerical Heat Transfer, Part B: Fundamentals*, 51(1):1–23.

S Peskin, C. (1977). Peskin, c.s.: Numerical analysis of blood flow in the heart. j. comput. phys. 25, 220-252. 25:220–252.

Shao, S. (2006). Incompressible sph simulation of wave breaking and overtopping with turbulence modelling. *International Journal for Numerical Methods in Fluids*, 50(5):597–621.

Shao, S., Ji, C., Graham, D. I., Reeve, D. E., James, P. W., and Chadwick, A. J. (2006). Simulation of wave overtopping by an incompressible sph model. *Coastal Engineering*, 53(9):723–735.

Shao, S. and Lo, E. Y. (2003). Incompressible sph method for simulating newtonian and non-newtonian flows with a free surface. *Advances in water resources*, 26(7):787–800.

Souto-Iglesias, A., Delorme, L., Pérez-Rojas, L., and Abril-Pérez, S. (2006). Liquid moment amplitude assessment in sloshing type problems with smooth particle hydrodynamics. *Ocean Engineering*, 33(11):1462–1484.

Swegle, J. and Attaway, S. (1995). On the feasibility of using smoothed particle hydrodynamics for underwater explosion calculations. *Computational Mechanics*, 17(3):151–168.

Tanaka, N. and Takano, T. (2005). Microscopic-scale simulation of blood flow using sph method. *International Journal of Computational Methods*, 2(04):555–568.

Tartakovsky, A. M. and Meakin, P. (2006). Pore scale modeling of immiscible and miscible fluid flows using smoothed particle hydrodynamics. *Advances in Water Resources*, 29(10):1464–1478.

Thacker, R. and Couchman, H. (2001). Star formation, supernova feedback, and the angular momentum problem in numerical cold dark matter cosmogony: halfway there? *The Astrophysical Journal Letters*, 555(1):L17.

TSUBOTA, K.-i., WADA, S., and YAMAGUCHI, T. (2006). Simulation study on effects of hematocrit on blood flow properties using particle method. *Journal of Biomechanical Science and Engineering*, 1(1):159–170.

Tu, C., Yin, Z., Lin, J., and Bao, F. (2017). A review of experimental techniques for measuring micro-to nano-particle-laden gas flows. *Applied Sciences*, 7(2):120.

Ulrich, C., Leonardi, M., and Rung, T. (2013). Multi-physics sph simulation of complex marine-engineering hydrodynamic problems. *Ocean Engineering*, 64:109–121.

Ulrich, C. and Rung, T. (2012). Multi-physics sph simulations of launching problems and floating body interactions. In *Proceeding of the 31st International Conference on Ocean, Offshore and Arctic Engineering (OMAE), June*, pages 10–15.

Vacondio, R., Rogers, B., and Stansby, P. (2012). Accurate particle splitting for smoothed particle hydrodynamics in shallow water with shock capturing. *International Journal for Numerical Methods in Fluids*, 69(8):1377–1410.

Vacondio, R., Rogers, B., Stansby, P., Mignosa, P., and Feldman, J. (2013). Variable resolution for sph: a dynamic particle coalescing and splitting scheme. *Computer Methods in Applied Mechanics and Engineering*, 256:132–148.

Valdez-Balderas, D., Domínguez, J. M., Rogers, B. D., and Crespo, A. J. (2013). Towards accelerating smoothed particle hydrodynamics simulations for free-surface flows on multi-gpu clusters. *Journal of Parallel and Distributed Computing*, 73(11):1483–1493.

Violeau, D. and Leroy, A. (2014). On the maximum time step in weakly compressible sph. *Journal of Computational Physics*, 256:388–415.

Violeau, D. and Leroy, A. (2015). Optimal time step for incompressible sph. *Journal of Computational Physics*, 288:119–130.

Violeau, D. and Piccon, S. (2001). Jp: Two attempts of turbulence modelling in smoothed particle hydrodynamics. In *In: Proceedings of the 8th International Symposium on Flow Modeling and Turbulence Measurements*. Citeseer.

Violeau, D. and Rogers, B. D. (2016). Smoothed particle hydrodynamics (sph) for free-surface flows: past, present and future. *Journal of Hydraulic Research*, 54(1):1–26.

Wells, M. and Wettlaufer, J. (2005). Two-dimensional density currents in a confined basin. *Geophysical & Astrophysical Fluid Dynamics*, 99(3):199–218.

Wendland, H. (1995). Piecewise polynomial, positive definite and compactly supported radial functions of minimal degree. *Advances in computational Mathematics*, 4(1):389–396.

Zhang, J., A. Maxwell, J., G. Gerber, A., Gordon L. Holloway, A., and D. Watt, G. (2013). Simulation of the flow over axisymmetric submarine hulls in steady turning. 57:180–196.

Zhou, C., Liu, G., and Lou, K. (2007). Three-dimensional penetration simulation using smoothed particle hydrodynamics. *International Journal of Computational Methods*, 4(04):671–691.

Zienkiewicz, O. and Taylor, R. (2000). *The Finite Element Method: Solid mechanics*. Referex collection.Mecánica y materiales. Butterworth-Heinemann.